SYNCHROTRON-BASED *IN-SITU* AND *EX-SITU* INVESTIGATION OF PEROVSKITE FOR PHOTOVOLTAIC APPLICATIONS

Elly Miller Shatsala

A thesis submitted in partial fulfillment of the requirements for the award of Doctor of Philosophy in Physics of Masinde Muliro Unversity of Science and Technology

June, 2025

PLAGIARISM STATEMENT

STUDENT DECLARATION:

1. I acknowledge that using content from other sources without proper citation, whether directly or through paraphrasing, constitute plagiarism. I understand that this violates the academic policies of Masinde Muliro University of Science and Technology.
2. I affirm that this thesis is entirely my own work.
3. I recognize that plagiarism is a serious academic offense. If any form of plagiarism is detected in my thesis, I accept that it may receive a failure grade "F".
4. I also understand that engaging in academic dishonesty, includes plagiarism, could result in suspension or expulsion from the university.

Sign: Shatsala ………………………… Date: 30/06/2025 …………………………

Shatsala Elly Miller
SPH/H/07/15

SUPERVISORS DECLARATION:

We hereby approve the examination of this thesis. The thesis has been subjected to plagiarism test and its similarity index is not above 20%.

Sign__________________________ Date……31/06/2025………
Dr. Celline Awino Omondi
Department of Physics
Masinde Muliro University of Science and Technology, Kakamega, Kenya

Sign………………………………. Date………………………....
Dr. Maxwell Mageto
Department of Physics
Masinde Muliro University of Science and Technology, Kakamega, Kenya

Sign………………………………. Date………………………....
Prof. Hussein Golicha
Department of Physics
Masinde Muliro University of Science and Technology, Kakamega, Kenya

DECLARATION

This PhD thesis is my original work prepared with no other than indicated sources and has not been presented elsewhere for a degree or any other award.

Sign: Shatsala Date: 30/06/2025

Shatsala Elly Miller

SPH/H/07/15

CERTIFICATION:

The undersigned certify that they have read and hereby recommend for acceptance of Masinde Muliro University of Science and Technology a Doctor of philosophy in physics thesis entitled **"SYNCHROTRON-BASED *IN-SITU* AND *EX-SITU* INVESTIGATION OF PEROVSKITE FOR PHOTOVOLTAIC APPLICATIONS"**

Supervisors:

Sign-------------------------- Date 26/06/2025…
Dr. Celline Awino Omondi
Department of Physics
Masinde Muliro University of Science and Technology, Kakamega, Kenya

Sign………………………………. Date………………………....
Dr. Maxwell Mageto
Department of Physics
Masinde Muliro University of Science and Technology, Kakamega, Kenya

Sign………………………………. Date………………………....
Prof. Hussein Golicha
Department of Physics
Masinde Muliro University of Science and Technology, Kakamega, Kenya

COPYRIGHT

DEDICATION

I dedicate this work to my beloved son and wife for the support they have offered me.

ACKNOWLEDGMENTS

I extend my sincere gratitude to Almighty God for granting us the strength and insight that guided this work. I am deeply thankful to LAAAMP for their generous grant, which played a vital role in supporting this research. Their belief in the significance of our study and their commitment to advancing knowledge in this field have been instrumental to its success. I also wish to express my heartfelt appreciation to Beamline 7.3.3 and Beamline 12.3.2 at the Advanced Light Source, which graciously hosted us through support from the Director of the Office of Science, Office of Basic Energy Sciences, U.S. Department of Energy, under Contract No. DE-AC02-05CH11231. My sincere thanks go as well to the Molecular Foundry division, which supported our work under the same contract.

In particular, I am profoundly grateful for the invaluable assistance provided by Dr. Chenhui Zhu, beamline scientist at 7.3.3; Dr. Nobumichi Tamura, senior scientist at 12.3.2; and Dr. Caroline Sutter-Fella, staff scientist in the Inorganic Nanostructures Facility at the Molecular Foundry. Their expertise and support were critical to the success of this project.

ABSTRACT

The advancement of perovskite-based optoelectronic devices hinges on overcoming their intrinsic instability challenges. Synchrotron-based techniques have been widely employed to characterize various materials, including the structural and interactive properties of perovskite crystals and their complexes, using *ex situ*, *in situ*, and *operando* approaches. Grazing Incidence Wide-Angle X-ray Scattering (GIWAXS) and Small-Angle X-ray Scattering (GISAXS) studies have revealed inherent crystal peaks in perovskite films through both *in situ* and *ex situ* methods. This thesis investigates the crystallization dynamics, humidity resilience, and defect passivation strategies of triple-cation ($Cs_{0.05}(FA_{0.83}MA_{0.17})_{0.95}Pb(I_{0.83}Br_{0.17})_3$) perovskite thin films, along with co-passivation strategies applied to $Cs_{0.1}FA_{0.9}PbI_3$ using phenylethylammonium chloride (PEACl) and 2,8-Bis(diphenylphosphoryl)dibenzo[b,d]furan (PPF), aiming to enhance structural, optical, and electronic properties for efficient photovoltaic applications. A comprehensive experimental approach was adopted, combining solvent engineering, anti-solvent optimization, and co-passivation strategies. Film fabrication and degradation behaviors were characterized using synchrotron-based *in situ* and *ex situ* GIWAXS techniques, micro-X-ray diffraction (μ-XRD), photoluminescence (PL) spectroscopy, UV-Vis absorption spectroscopy, Atomic Force Microscopy (AFM), Scanning Electron Microscopy (SEM), and Energy Dispersive X-ray Spectroscopy (EDS) for detailed analysis. Results reveal that 5% cesium incorporation into triple-cation perovskites yields superior crystal structures, minimizing δ-perovskite phase and PbI_2 formation while enhancing humidity resistance. Solvent treatments, particularly with ethyl acetate (EA) and chlorobenzene (CB), influenced grain size, surface morphology, and film smoothness. Co-passivation of $Cs_{0.1}FA_{0.9}PbI_3$ with PEACl and PPF slowed crystallization kinetics, regulated grain orientation, suppressed non-radiative recombination centers, and stabilized the thermodynamically favorable α-perovskite phase. GIWAXS data confirmed the evolution of highly oriented 2D/3D mixed-phase architectures with enhanced c-axis unit cell alignment. Surface and elemental analysis demonstrated uniform passivant distribution, stronger Pb–O bonding, and reduced ion migration pathways. Photo-physical studies showed narrowed PL peaks, bandgap tuning, and reduced trap densities. This work establishes a strategic framework for achieving high-quality, stable perovskite films, laying the foundation for fabricating full solar modules at MMUST Materials Research Laboratory. The outcomes also pave the way for future collaborations, contributing toward the commercialization of perovskite photovoltaics with power conversion efficiencies exceeding 40%. Additionally, ongoing work involving robot automation and Machine Learning for high-throughput experiments at the Advanced Light Source, along with the development of a new multimodal spin-coater design to eliminate overheating and mechanical wobbles, is expected to further enhance beamline studies for perovskite, polymer, and battery research.

TABLE OF CONTENTS

LIST OF TABLES

LIST OF FIGURES

LIST OF ABBREVIATIONS AND ACRONYMS

0D	Zero Dimension
1D	One Dimension
1T	Thiophene
2D	Two Dimension
2*H*	2-Hexagonal
2T	Bi-Thiophene
3-CAT	Triple cation
3D	Three Dimension
3T	Terthiophene
4*H*	4-Hexagonal
6*H*	6-Hexagonal
8*H*	8-Hexagonal
a	lattice constant/parameter
$\vec{\boldsymbol{a}}$	Scattering vector
A	Absorption factor of x-ray
AFM	Atomic Force Microscopy
AgB	Silver Behenate

Al_2O_3	Aluminium oxide
ALS	Advanced Light Source
APS	Advanced Photon Source
APXPS	Angle-Resolved X-ray Photo-electron Spectroscopy
ARPES	Angle-Resolved Photo-emission Spectroscopy
$\vec{B}$	Magnetic field
$\overrightarrow{B_y}$	Unidirectional Magnetic field
BA	Butylammonium
BAI	Butylamminium Iodide
BDA	1,4-butanediamonium
BF_4	Tetrafluoroborate
BP	Black Phosphorene
Br	Bromine
CA	California
$CaTiO_3$	Calcium titanate
CB	Chlorobenzene
CCD	Charge-Couple Device
CdTe	Cadmium Telluride

$CH_3NH_3PbI_3$	Methylammonium Lead Iodide
$CH_3NH_3PbBr_3$	Methylammonium Lead Bromide
$CH_3NH_3PbI_{3-x}Br_x$	Methylammonium Lead Iodide/Bromide
$CH_3NH_3PbI_{3-x}Cl_x$	Methylammonium Lead Iodide/Chloride
CIGS	Copper Indium Gallium Selenide
Cl	Chlorine
CO_2	Carbon Dioxide
Cs	Cesium
c-Si	Crystalline Silicon
$CsMAFAPbI_3$ (Cs-MAFA)	Cesium Methyl Ammonium Bromide Formammidium Lead Iodide
CSV	Comma-Separated Values
d	lattice spacing
d	material thickness
D	Divalent (organic spacer cation)
DAN	dianthradipyridine
DC	Direct Current
DFT	Density functional theory
DI	De-Ionized water

DJ	Dion-Jacobson
DMF	Dimethylformamide
DMSO	Di-Methyl Sulfoxide ,
DSSCs	Dye Sensitized Solar Cells
EA	Ethyl-Acetate
EDS	Energy-Dispersive x-ray Spectrometer
ESRF	European Synchrotron Radiation Facility
E_x	*E*xciton binding energies
f_a	atomic scattering factor
FA (CH $(NH_2)_2^+$)	Formadinium
FAI	Formammidium Iodiode
FAPI	Formmmidium Lead Iodiode.
FELs	free-electron lasers
FETs	Field Effect Transistors
FTIR	Fourier transform infrared spectroscopy
GaAs	Gallium Asernide
Ge	Germanium
GISAXS	Grazing Incident Small Angle X-ray Scattering

GIWAXS	Grazing Incident Wide Angle X-ray Scattering
GIXD	Grazing Incident X-ray Diffraction
HAQ	hot air quenching process
hkl	Miller indices
H_2O	Water
I	Iodine
ICDD	International Centre for Diffraction Data
$I_{(q)}$	Intensity of scattered radiation
IR	Infra-Red
ITO	Indium Tin Oxide
K	Kelvin
KB	Kirkpatrick–Baez
k_i and k_f	Initial and final wave-vectors
L	Ligand (organic spacer cation)
LAAAMP	Lightsources for Africa, the America, Asia, Middle east and the Pacific
LBNL	Lawrence Berkeley National Laboratory
LINAC	Linear Accelerator
M	Molar

MA ($CH_3NH_3^+$)	Methylammonium
MABr	Methylammonium Bromide
$MAFAPbI_3$ (MAFA)	Methylammonium Bromide Formammidium Lead Iodide
MAI	Methyl-Ammonium Iodide
MAPI	Methylammonium Lead Iodide
MJ	Multi-Junctions
MMSC	Multi-Modal Spin Coater System
MMUST	Masinde Muliro University of Science and Technology
N	Number of elements in a unit cell
O_2	Oxygen
P	structure/form factor
P	phosphorus
Pb	Lead
$PbCl_2$	Lead Chloride
PCE	Performance Cell Efficiency
PDA	propane-1,3-diammonium
PEA	Phenyethylammonium
PEACl	phenylethylammonium chloride

PF_6	Hexafluorophosphate
PL	Photoluminescence
PNMR	phosphorus nuclear magnetic resonance
PPF	2,8-Bis(diphenyl-phosphoryl)-dibenzo[b,d]furan
PSO	Photon Science Group
PV	Photovoltaic
q	Inverse space vector
r	distance from the center of mass
r_A, r_B, and r_X	ionic radii of A, B, and X ions in ABX_3 perovskite
RAT	Reflection, Absorption and Transmittance
RF	Radio Frequency
RH	Relative Humidity
RIXS	Resonant Inelastic X-ray Scattering
R_j	position elements in a unit cell at j
RMS	root-mean-square
RP	Ruddlesden–Popper
rpm	revolutions per minute
SAXS	Small Angle X-ray Scattering

SCN	Supra-Chiasmatic Nucleus
SCs	Solar Cells
SEM	Scanning Electron Microscopy
SLS	Synchrotron Light Source
Sn	Tin
SRS	Synchrotron Radiation Source
t	tolerance factor
TFT	trifluoro toluene
TiO_2	Titanium Oxide
TMDS	Transition Metal Dichalcogenides
PEDOT	poly(3,4-ethylenedioxythiophene
PSS	polystyrene sulfonate
TCI	Tokyo Chemical Industry
t_y	Geometric and polarization factors parameter
UK	United Kingdom
USA	United States of America
V_{oc}	Open-Circuit Voltage
VRS	Video-Rate Scanning

UV – light	Ultra-Voltage Light
UV-Vis	Utra-Violet Visual
v/v	Volume-Volume ratio
WAXS	Wide Angle X-ray Scattering
wt%	percentage with respect to
XAS	X-Ray absorption spectroscopy
XRD	X-Ray Diffraction
XRF	X-ray fluorescence
Z	Atomic Number

Units

%	percentage
^{0}	degree
Å	Armstrong
^{0}C	degree celcius
cm^2	square centimeter
μl	microlitre
μm	micrometre
g	grams

eV	electron volts
GeV	Giga Electron Volts
keV	kiloelectronVolts
g/mol	gram per mol
mg/ml	milligram per millilitre
m/s^2 or ms^{-2}	metre per second squared
nm	nanometre
mm	millimetre
MeV	Mega electro Volt
mg	milli-gram
s	Second
Ω /sq	Ohm per square

Greek Alphabet

α	Alpha
δ	Delta
θ	scattering angle
μ	linear absorption coefficient
ρ	material density

$\rho_{(r)}$	electronic density
λ	X-ray wavelength
Ω	ohm

CHAPTER ONE
INTRODUCTION

1.1 The synchrotron background

1.1.1 Origin of synchrotrons

A synchrotron is a circular particle accelerator that accelerates charged particles, typically electrons, using sequences of magnets until they approach the speed of light (Willmott, P., 2019). As these electrons move at high speeds, they emit extremely bright light known as synchrotron radiation, which is millions of times brighter than conventional light sources and billions of times brighter than the sun. This intense light, primarily in the X-ray region, enables scientists to study matter at the atomic and molecular scale (Godwin, R. P., 1969).

Synchrotrons share many similarities with storage rings, as both feature a circular arrangement of magnets, a vacuum chamber, and other common components. In fact, a single ring can often be designed to function as both a synchrotron and a storage ring. By producing synchrotron radiation across a wide spectrum, from infrared to hard X-rays, synchrotrons are valuable tools for exploring various fields. They are used to study material structures, chemical bonding, and defect distributions in crystals, among other applications (Dudley M., 2023).

The remarkable legacy of modern physics as discussed in section 2.1, is deeply rooted in a series of transformative discoveries that began with Maxwell’s seminal work on electromagnetism in 1873 (Maxwell, J. C., 1873) and extended through the discovery and practical application of X-rays. Wilhelm Röntgen’s accidental discovery of X-rays in 1895, followed by Charles Barkla’s demonstration of elemental X-ray signatures in

1906, and Max von Laue's innovative X-ray diffraction experiments in 1912, collectively laid the groundwork for modern crystallography and atomic-scale investigations (Tubiana, M., 1996; Dibner, B., 1968).

The pioneering contributions of William Henry Bragg and Lawrence Bragg in 1913 cemented the methodology for determining crystal structures via the diffraction of X-rays (Bragg, W. H., & Bragg, W. L., 1913), fundamentally transforming our ability to probe the atomic organization of matter. Later, the construction of the first synchrotron in 1946 validated the concept of using high-energy particle accelerators and revealed the immense potential of the synchrotron light emitted as a by-product. The subsequent establishment of a dedicated synchrotron light source at Daresbury in 1980 marked a paradigm shift that enabled high-precision research across a host of disciplines (Wikipedia contributors, 24th March, 2025).

Today, synchrotron radiation is at the heart of experimental research across multiple fields, driving innovations that impact material science, healthcare, environmental studies, and beyond. Each stage of this historical progression not only exhibits the cumulative nature of scientific discovery but also demonstrates how theoretical insights and experimental ingenuity work together to push the boundaries of what is possible in modern science (Fan, C., & Zhao, Z. (Eds.), 2018).

1.1.2 Synchrotron facilities around the world

According to available information, there are approximately 70 synchrotron facilities and storage rings around the world, with various stages of development, including operational and under construction facilities (Lightsources.org. (May 18, 2025). Some prominent synchrotron sources around the world today include: the Advanced Light

Source (ALS) in Berkeley, California, USA; the Advanced Photon Source (APS) in Argonne, Illinois, USA; the European Synchrotron Radiation Facility (ESRF) in Grenoble, France; the Diamond Light Source in Didcot, UK; the Swiss Synchrotron Light Source (SLS) in Villigen, Switzerland; the MAX-lab in Lund, Sweden; and the Pohang Accelerator Laboratory in Pohang, South Korea.

It is important to highlight the growing initiative to establish an African synchrotron facility, an idea that began gaining traction about a decade ago. Significant progress has been made, including the development of a clear roadmap, training of users and personnel, and efforts to secure funding.

1.1.3 Synchrotron applications to our work

This discussion primarily focused on the Advanced Light Source, at which research was conducted, whereby, synchrotron-based protocol was developed to study perovskite crystallization, stability, and phase transitions, focusing on improving photovoltaic performance. *Ex situ* GIWAXS and micro-diffraction analysis of triple-cation perovskite films confirmed their transformation to a stable cubic phase, though slight reversion to the hexagonal phase was observed.

A 5% cesium composition maintained stability even under non-equilibrium humidity conditions. Co-passivation of $Cs_{0.1}FA_{0.9}PbI_3$ with PEACl and PPF slowed film growth, bypassing the unstable delta phase and enhancing stability. PL and UV-Vis spectroscopy showed emission at 780 nm with a 1.6 eV bandgap, while EDS mapping indicated oxygen coordination with lead.

1.2 Problem Statement

The growing concerns over climate change and energy shortages highlight the need for alternative renewable energy sources. Fossil fuels, the dominant energy source, contribute to environmental pollution through carbon dioxide emissions, and also leads to global temperature rise. Solar energy presents a promising alternative, but photovoltaic devices must be cost-effective, scalable, and stable to compete in the market.

Perovskite solar cells offer advantages such as high absorption coefficients, ease of fabrication, and efficient charge transport. However, their instability when exposed to oxygen, heat, moisture, and interface dynamics remains a major challenge. Understanding perovskite crystallization under environmental conditions like humidity is crucial for improving their stability and performance. While several studies have explored perovskite crystal growth using laboratory and synchrotron based *ex situ* and *in situ* techniques, gaps remain in analyzing its formation from the precursor solution to the final film.

Recent researches have utilized *in situ* Grazing Incidence X-ray Diffraction (GIXD) and Fourier Transform Infrared Spectroscopy (FTIR) to investigate perovskite crystallization (Burwig T., 2023 ; Szostak, R., *et al*., 2023 ; and Urwick, A. 2023). However, studies have not extensively examined triple and double cation perovskite compositions under GIWAXS techniques in humidity and inert environments. To address this, the Advanced Light Source (ALS) developed an *in situ* Multi-Modal Spin Coater (MMSC) system, integrating synchrotron-based GIWAXS/GISAXS techniques. This system enables real-time, high-resolution monitoring of perovskite crystallization. While humidity studies have been explored on 2D perovskites, it remains largely unexplained for high performing 3D formulation based on triple and double cations including those employing PEACl/PPF co-passivating strategies.

1.3 Objectives of the study

This study aims to develop a unified synchrotron protocol for investigating perovskite crystallization dynamics, stability, and morphological evolution, with a focus on phase transitions, degradation resistance, and co-passivation effects to improve photovoltaic performance.

1.3.1 Specific objectives

I. To determine film stability under non-equilibrium humidity conditions on ($Cs_{0.05}(FA_{0.83}MA_{0.17})_{0.95}Pb(I_{0.83}Br_{0.17})_3$) films through *ex situ* GIWAXS and micro-diffraction analysis.

II. To analyse the crystallization dynamics of perovskite film by tracking phase transitions and structural evolution in real-time using *in situ* GIWAXS.

III. To study the effects of co-passivation with PEACl and PPF of $Cs_{0.1}FA_{0.9}PbI_3$ films on the structure, defects, and phase orientation using *ex situ* GIWAXS and photoluminescence.

IV. To characterize the morphological, electronic, and optical properties using AFM, SEM, PL, and UV-Vis spectroscopy, respectively; along with elemental mapping via EDS, in order to understand crystallinity, molecular interactions, and defect mitigation for enhanced stability and performance.

1.4 Justification of the study

Over the past decade, research on perovskite solar cells (PSCs) has yielded impressive power conversion efficiencies (PCEs), with single-junction devices approaching nearly 27% in performance (National Renewable Energy Laboratory, 2020), making them promising for solar cells, LEDs, and photodetectors. However, their stability, scalability, and performance remain significant challenges for commercialization. To address these issues, optimizing crystallization kinetics under controlled humidity while employing strategic passivation is essential for enhancing structural integrity and mitigating degradation. The transition from liquid precursors to bulk polycrystals is highly sensitive to environmental factors, impacting key optoelectronic properties. *In situ* synchrotron techniques, such as GIWAXS and GISAXS, provide high temporal resolution to track crystallization kinetics, phase transitions, and grain growth in real time. Micro-diffraction further reveals localized structural details like strain distributions and defect propagation.

Phase transitions, such as those between tetragonal and cubic phases, play a crucial role in defining perovskite optoelectronic behavior. Synchrotron-based X-ray diffraction enables precise monitoring of these transitions under varying conditions, allowing direct correlation between structural changes and device efficiency. Additionally, the performance of perovskite materials is highly dependent on the effectiveness of passivation layers. *In situ* studies provide crucial insights into their long-term stability, defect mitigation, and the impact on grain boundary which is beneficial for charge carrier separation and transport.

Complementary characterization techniques such as photoluminescence (PL) and UV-Vis spectroscopy are crucial for analyzing the electronic and optical properties of perovskite films. PL mapping identifies defects, non-radiative recombination centers, and charge carrier dynamics, providing critical insights into film uniformity and potential efficiency losses. UV-Vis spectroscopy evaluates optical absorption, ensuring optimal bandgap energies for high-efficiency solar cells. Collectively, these techniques form a multi-modal framework that links structural properties to performance metrics.

This study focuses on monitoring perovskite film morphology under *in situ* humidity conditions to understand crystal growth and material depletion. By analyzing nucleation patterns and kinetically trapped morphologies, the research aims to refine fabrication protocols and reduce defects formation that hinders large scale scalability. A combination of *in situ/ex situ* GIWAXS, *ex situ* micro-diffraction, PL, UV-Vis, SEM, and EDS mapping provides a comprehensive understanding of crystallization dynamics and degradation mechanisms. These insights will contribute to the development of stable, high-performance, and commercially viable perovskite-based devices.

CHAPTER TWO
LITERATURE REVIEW

2.1 Synchrotrons Radiations

2.1.1 An introduction to synchrotrons radiations

The evolution of modern physics has been marked by a succession of seminal breakthroughs stretching from theoretical innovations to state-of-the-art experimental techniques (Maxwell, J. C., 1873; Simonyi, K., 2012; Miller, A. I., 2014; and O'Neill, W., 2024). Every transformative discovery, beginning with James Clerk Maxwell's revolutionary theory of electromagnetism in the 19th century and culminating with the creation and dedicated use of synchrotron light sources in the late 20th century, has redefined our understanding of the nature of light and matter (Romano, R., 1869). This thesis provides an extensive account of pioneering contributions—from Maxwell's formulation of electromagnetic theory to the construction of the first synchrotron in 1946 and onward to today's advanced research facilities—thereby establishing a continuous lineage of scientific progress that underpins modern research in physics, materials science, and beyond (Wikipedia contributors, 24th March, 2025).

The narrative traces how early theoretical work laid the groundwork for experimental techniques that now allow investigators to probe atomic structures and explore complex materials (Stanik, E., Döhring, T., Schreiber, K., Kätker, A., & Busch, U., 2023). Through rigorous experimentation and innovation, each breakthrough has demonstrated the profound impact of these discoveries on a wide range of applications including medical imaging, structural biology, and environmental science (Fenter, P. A., Rivers, M. L., Sturchio, N., & Sutton, S. R., 2018).

2.1.2 Foundations of Electromagnetism and the Birth of X-Ray Science

In 1873, James Clerk Maxwell published his transformative treatise in which he formulated a set of equations that fundamentally reconciled electricity, magnetism, and light into one unified electromagnetic framework (Maxwell, J. C., 1873). Maxwell's work, initially presented in a two-volume treatise, laid the mathematical groundwork for understanding the propagation of electromagnetic waves, an insight that eventually led to the discovery of electromagnetic radiation across a diverse range of frequencies (Maxwell, J. C., 1873).

His pioneering equations not only characterized the dynamics of the electromagnetic field but also challenged the prevailing mechanistic view of the physical universe by proposing that fields, rather than discrete particles, governed the interaction between matter and energy (Maxwell, J. C., 1873). This theoretical revolution set the stage for subsequent experimental discoveries by providing a clear, mathematical prediction of how electromagnetic disturbances move through space (Romano, R., 1869; Macfarlane, A., 2021). Maxwell's synthesis of theory and mathematical abstraction not only altered the landscape of physics during his time but also laid a crucial foundation for later developments in the field of X-ray science and particle acceleration (Maxwell, J. C., 1873).

2.1.3 The Discovery of X-rays and Their Pervasive Impact

In 1895, while experimenting with evacuated Crookes tubes, Wilhelm Conrad Röntgen observed a mysterious form of radiation that was capable of penetrating opaque materials and casting detailed shadows on a fluorescent screen (Tubiana, M., 1996;

Dibner, B., 1968). This unexpected phenomenon, later named X-rays due to their unknown nature, fundamentally altered both physics and medicine by providing a non-invasive method to view the interior of objects (History.com Editors., 23rd March, 2025).

Röntgen's discovery, made while investigating the behavior of cathode rays, revealed that these new rays could produce images of bones and metal objects buried within various substances, thus opening the door to diagnostic radiography (Busch, U., 2023). His seminal experiments, including the famous radiograph of his wife's hand, demonstrated that X-rays could reveal hidden structures by interacting differently with matter depending on its density and composition (History.com Editors., 23rd March 2025). The rapid acceptance and integration of X-ray technology into the medical field underscored the importance of these non-visible rays, which gradually became indispensable for both experimental research and clinical diagnosis (History.com Editors., 23rd March 2025).

2.1.4 Charles Barkla's Contributions to Elemental Identification with X-Rays

Building on the groundwork laid by Röntgen, Charles Barkla made significant strides in 1906 by demonstrating that the secondary X-ray spectra emitted from elements were unique to each substance (NobelPrize.org., 23rd March 2025). By carefully analyzing the scattering of X-rays in gases, Barkla was able to identify distinct spectral fingerprints that provided critical insights into the electronic structure of atoms (Barkla, C. G.; 1905; Skulls in the Stars, 2009). His experiments further showed that X-rays were inherently transverse electromagnetic waves, as he successfully demonstrated their polarization properties through innovative experimental setups (Barkla, C. G.; 1905; Skulls in the Stars, 2009).

Barkla’s findings on the characteristic spectra not only validated theoretical expectations based on Maxwell’s predictions but also introduced a robust method for elemental identification that would pave the way for future advances in atomic spectroscopy (Barkla, C. G.; 1905). These pioneering experiments underscored the importance of X-ray scattering as a tool for understanding atomic structure and provided a methodological backbone for later developments in X-ray crystallography and material analysis (NobelPrize.org., 23rd March 2025).

2.1.5 Max von Laue and the Advent of X-Ray Crystallography

In 1912, Max von Laue proposed that crystals, with their regular and repeating atomic arrangements, could diffract X-rays to form distinct interference patterns that carried detailed information about their internal structure (Stanik, E., Döhring, T., Schreiber, K., Kätker, A., & Busch, U., 2023). His hypothesis that X-rays, fundamentally electromagnetic waves, might interact with the periodic lattice of a crystal set the stage for the groundbreaking field of X-ray crystallography (Barkla, C. G., 1905; Skulls in the Stars, 2009).

Von Laue’s experiments involved directing a beam of X-rays through a crystal such as copper sulfate, where the resulting diffraction pattern, recorded on photographic plates, provided compelling evidence for the wave nature of X-rays (Barkla, C. G., 1905; Skulls in the Stars, 2009). The observed patterns, characterized by a series of distinct spots, were directly linked to the spatial arrangement of atoms within the crystal (Barkla, C. G., 1905). This revolutionary method not only confirmed that X-rays could be used to discern atomic spacing but also established a direct connection between electromagnetic theory and the structural analysis of matter (Barkla, C. G., 1905). Consequently, von Laue’s work expanded the horizons of both physics and chemistry by offering a novel experimental technique to probe the crystalline structure of a wide range of materials (Barkla, C. G., 1905).

2.1.6 The Braggs and the Foundation of Modern Crystallography

Following von Laue’s pioneering work, the subsequent contributions of William Henry Bragg and his son, Lawrence Bragg, during 1913–1914 further advanced the application of X-ray diffraction for structural analysis (Alford, T. L., Feldman, L. C., & Mayer, J. W., 2007; Aguilar-Marín, P., Angelats-Silva, L., Noriega-Diaz, E., Chavez-Bacilio, M., & Verde-Vera, R., 2020). The formulation of Bragg’s Law, expressed as ($n\lambda = 2d\sin\theta$ given as $q = \frac{2\pi}{d}$ in q-space and as $\vec{\boldsymbol{q}} = \vec{\boldsymbol{k}}_{\mathrm{f}} - \vec{\boldsymbol{k}}_{\mathrm{i}} = \vec{\boldsymbol{G}}$ in reciprocal lattice as explained in details in section 2.5), provided a precise mathematical relationship connecting the wavelength of X-rays, the inter-planar spacing of crystals, and the angles at which diffraction occurs (Jenkin, J., 2008).

This elegant law used a model where the crystal was envisaged as a series of parallel planes, and the constructive interference of X-rays reflected off these planes produced detectable diffraction peaks (Jenkin, J., 2008). William Henry Bragg constructed the first X-ray spectrometer in 1913, an innovation that allowed for the accurate measurement of X-ray spectra and ultimately enabled the determination of atomic arrangements in crystals (Ameh, E. S.; 2019). Lawrence Bragg’s subsequent work with common salt crystals using this new spectrometer and Laue’s method further substantiated the predictive power of Bragg’s Law, thereby laying the groundwork for modern crystallography (Jenkin, J., 2008).

Their collaborative efforts not only earned them the Nobel Prize in 1915, making them the only father-and-son team to share this honor in physics, but also cemented the methodological foundations that now drive research in material science, solid state physics, and chemistry (Aguilar-Marín, P., Angelats-Silva, L., Noriega-Diaz, E., Chavez-Bacilio, M., & Verde-Vera, R., 2020; Alford, T. L., Feldman, L. C., & Mayer, J. W.; 2007). Their work revolutionized how scientists could probe the atomic-scale structure of matter, a capability that remains essential in diverse scientific fields (Ameh, E. S.; 2019).

2.1.7 The Birth of Electron Synchrotrons and the Emergence of Synchrotron Light

The construction of the first synchrotron in 1946 marked a pivotal moment in accelerator physics as scientists sought to study high-energy particle collisions using advanced electromagnetic acceleration techniques (Lawson, J. D., 1997). Initially derived from the adaptation of existing betatrons, this early synchrotron verified the practicality of accelerating charged particles around a circular path using magnetic fields (Symmetry Magazine, 2005; Fenner, E., 2014). Although its primary purpose was to facilitate high-energy collision experiments, researchers soon discovered that the synchrotron emitted brilliant forms of radiation as a secondary phenomenon (Lawson, J. D., 1997).

This synchrotron radiation, which was initially considered an unwanted by-product, exhibited extraordinary brightness and a broad spectral range, prompting scientists to consider its potential for applications beyond particle physics (Sharp-Paul, N., 2017).

Early experiments at Cornell University in 1956 demonstrated that synchrotron light could be harnessed and used for precision X-ray spectroscopy (possessed X-ray properties), thus opening a host of new applications in both fundamental and applied sciences (Sharp-Paul, N., 2017). The unexpected discovery that accelerators could serve as intense light sources represented a transformative shift in experimental research techniques, integrating accelerator-based facilities with precision light-matter interaction studies (Sharp-Paul, N., 2017).

2.1.8 The Development of the World's First Dedicated Synchrotron Light Source

The realization that synchrotron light offered unique research capabilities ultimately led to the construction of the world's first dedicated synchrotron light source in the United Kingdom in 1980, located at Daresbury in Cheshire (Wille, K., 1991). This dedicated facility, known as the Synchrotron Radiation Source (SRS), was specifically designed to produce high-brilliance light beams for a wide range of scientific investigations (Winick, H., 1994).

Unlike earlier light sources that had been primarily developed for high-energy particle collision research, the SRS focused exclusively on exploiting the extraordinary properties of synchrotron light (Wille, K., 1991). Its design featured a 2-GeV electron storage ring that enabled the continuous production of synchrotron radiation across a broad electromagnetic spectrum, from infrared to hard X-rays (Winick, H., 1994). The SRS quickly became renowned for its versatility, hosting numerous beamlines that allowed researchers to perform a variety of experiments in structural chemistry, material science, and even biological studies (Wille, K., 1991).

Over the course of its operational lifespan from 1981 to 2008, the SRS provided over two million hours of beam time, catalyzing thousands of publications, numerous patents, and several prize-winning scientific achievements (Winick, H., 1994). This pioneering facility not only demonstrated the feasibility and utility of dedicated synchrotron light sources but also inspired the development of more advanced third-generation synchrotrons around the world (Wille, K., 1991).

2.1.9 Comparative Insights into Early and Modern Synchrotron Facilities

When comparing the initial synchrotron light produced as a by-product in high-energy particle accelerators with dedicated sources, significant advancements in brightness, stability, and versatility become evident (Mino, L., Borfecchia, E., Segura-Ruiz, J., Giannini, C., Martinez-Criado, G., & Lamberti, C., 2018). Early synchrotron experiments, such as those conducted at Cornell University in 1956, relied on incidental radiation from colliders that were not optimized for light production, leading to limitations in beam quality and control (Mino, L., Borfecchia, E., Segura-Ruiz, J., Giannini, C., Martinez-Criado, G., & Lamberti, C., 2018).

In contrast, purpose-built facilities like the SRS were engineered to maximize the brilliance and tunability of the emitted light by incorporating optimized magnetic lattice designs and specialized insertion devices (Wille, K., 1991). Modern synchrotron sources now feature advanced storage rings with sophisticated beamline instrumentation that allow researchers to achieve highly focused and stable beams across diverse wavelength ranges (Winick, H.,1994).

As a result, modern synchrotron light sources support precision experiments in fields ranging from nanoscience to biological imaging, a technological leap that underscores the transformative impact of dedicated synchrotron facilities (Clegg, W., 2019). These technological advancements not only enhance scientific discovery but also provide an invaluable bridge between theoretical predictions and experimental validation in numerous areas of physical and life sciences (Clegg, W., 2019).

2.1.10 Comparative Perspectives and Global Developments

Over the decades, synchrotron light sources have not only proliferated around the world but have also diversified in terms of their design and application (Mobilio, S., Boscherini, F., & Meneghini, C., 2016). Today-as mentioned earlier, more than 40 major facilities operate worldwide, each tailored to the unique demands of various scientific disciplines, while continuous upgrades ensure that they remain at the forefront of technological innovation (Mobilio, S., Boscherini, F., & Meneghini, C., 2016).

These facilities are distributed across multiple continents, thereby promoting international collaboration and facilitating access to cutting-edge research infrastructure for scientists from diverse backgrounds (Winick, H., 1994). For instance, while the Daresbury SRS in the United Kingdom pioneered the concept of a dedicated synchrotron light source, subsequent facilities such as the Advanced Light Source (ALS) in the USA and Diamond Light Source in the United Kingdom were built on its legacy by incorporating more advanced technologies and expanding experimental capabilities (Clegg, W., 2019).

A comparative analysis reveals that each generation of synchrotrons has seen improvements in both beam brightness and stability, key factors that have enabled new experimental techniques and broadened the range of research problems that can be tackled (Winick, H., 1994). This global proliferation has spurred a dynamic ecosystem in which technological advancements at one facility quickly disseminate through collaborative networks, thereby accelerating the pace of scientific discovery worldwide (Clegg, W., 2019).

2.1.11 Synchrotron radiation as an Electro-magnetic Emission with inherent characteristics

Synchrotron radiation describes the electromagnetic emission produced when charged particles—typically electrons—are accelerated to velocities approaching that of light and compelled to travel along curved trajectories by the influence of magnetic fields (NIST., 24th March, 2025). This remarkable phenomenon results from the fundamental principles of electrodynamics, which dictate that any accelerating charge will emit electromagnetic radiation (Wikipedia contributors, 24th March, 2025.). The radiation spans a broad range of wavelengths and exhibits extraordinary brightness, making it an indispensable asset for modern scientific research across numerous disciplines (Wikipedia contributors., 24th March, 2025).

Moreover, the controlled manipulation of the electron energy and magnetic environment in synchrotron facilities amplifies the inherent characteristics of the radiation, transforming it into a versatile probe for studying matter at atomic and molecular scales (Deutsches Elektronen-Synchrotron (DESY)., 24th March, 2025). Researchers worldwide routinely harness these features to investigate the structural, electronic, and dynamic properties of materials, biological specimens, and chemical systems through various experimental modalities (Hiden Analytical., 24th March, 2025).

2.1.12 Radiation Generation in Synchrotrons

The generation of synchrotron radiation occurs when electrons, traveling in a storage ring discussed in section 2.3, are forced to follow a curved path due to magnetic fields as stated before, predominantly provided by bending magnets, undulators, or wigglers (NIST., 24th March, 2025). In these accelerators, the rapid change in the direction of the fast-moving electrons produces a pulsed emission of radiation that is both highly collimated and intense (Deutsches Elektronen-Synchrotron (DESY)., 24th March, 2025). The radiation emerges as a consequence of the relativistic Doppler effect, whereby the radiation is compressed in the forward direction to form a narrow beam with a divergence typically on the order of one milli-radian or less.

This directional confinement, known as natural collimation, ensures that a large number of photons is delivered onto a very small area, significantly enhancing the signal available for experimental studies (Wikipedia contributors, 24th March, 2025). Furthermore, modern synchrotron facilities incorporate advanced insertion devices- discussed in section 2.3.2 that allow improved control over the electron trajectories and, in turn, finer tuning (European Organization for Nuclear Research (CERN)., 24th March, 2025) of the emitted radiation properties described as in section 2.2 below.

2.2 Fundamental Properties of Synchrotron Beams

2.2.1 High Intensity

Synchrotron radiation is notably characterized by its exceptionally high intensity, with brightness levels that far exceed those obtained from conventional laboratory sources (Wikipedia contributors, 23rd March, 2025). This high intensity stems from both the concentration of the radiation into a narrow beam and the enormous number of photons generated by the rapid acceleration of charged particles (Hiden Analytical., 24th March, 2025). The concentrated photon flux enables experiments to be performed on extremely small or weak samples, which would be challenging or even impossible to study using less intense sources (Hiden Analytical., 24th March, 2025).

In practice, high-intensity beams are crucial for probing the structural details of nanostructured materials, biological macromolecules, and other advanced materials (Grabowski, M., Cooper, D. R., Brzezinski, D., Macnar, J. M., Shabalin, I. G., Cymborowski, M., ... & Minor, W., 2021). The brightness, defined as the number of photons per unit area, per unit solid angle, and per unit time, is a key performance metric that distinguishes synchrotron radiation from other artificial light sources (Deutsches Elektronen-Synchrotron (DESY)., 24th March, 2025). This property has enabled breakthroughs in fields ranging from condensed matter physics to molecular biology by facilitating experiments that require both high resolution and minimal sample volumes (Wikipedia contributors, 23rd March, 2025).

2.2.2 Wide Spectrum

One of the most striking features of synchrotron radiation is its ability to span a very wide spectrum of frequencies, covering everything from the infrared region through the visible and ultraviolet up to hard X-rays (Wikipedia contributors, 23rd March, 2025). The vast spectral range arises because the emitted photons can have energies that vary over several orders of magnitude, which is a direct result of the relativistic motion of the electrons in the magnetic field (NIST., 24th March, 2025).

This broad wavelength range makes synchrotron radiation extremely versatile, as experiments can be tuned to specific regions of the spectrum to optimize the study of different physical phenomena (Hiden Analytical., 24th March, 2025). For example, infrared synchrotron radiation is commonly used for vibrational spectroscopy of organic and biological materials, whereas X-ray wavelengths are indispensable for crystallography and high-resolution imaging (Wikipedia contributors, 23rd March, 2025). Because a single synchrotron source can provide radiation across such a valuable continuum, researchers can perform complementary experiments without the need for multiple dedicated facilities (Deutsches Elektronen-Synchrotron, 24th March, 2025).

2.2.3 Tunable Wavelengths

A key advantage of synchrotron radiation sources is the ability to precisely tune the wavelength of the emitted light, enabling scientific experiments to be highly specific in terms of energy selection (Canon., 24th March, 2025). By adjusting the energy of the electrons in the storage ring and utilizing specialized magnetic devices, such as undulators and wigglers (discussed in details in section 2.3.2), the output wavelength can be shifted over a broad range (Elleaume, P., 1990).

In undulators, for instance, the periodic arrangement of dipole magnets forces the electrons into a sinusoidal path, leading to constructive interference effects that yield sharp spectral peaks at well-defined wavelengths (Deutsches Elektronen-Synchrotron (DESY)., 24th March, 2025). This tunability is especially crucial for anomalous dispersion experiments in crystallography, where precise wavelength settings allow researchers to exploit absorption edges of specific elements within a sample for phase determination (Canon., 24th March, 2025). Moreover, the ability to alter the magnetic field strength through which the electrons travel provides another level of control, ensuring that the radiation can be tailored to meet the exact requirements of various experimental protocols (SEES., 24th March, 2025).

2.2.4 Coherence

The coherent nature of synchrotron radiation is one of its most beneficial properties, as it indicates that the light waves are in phase over extensive distances (Wikipedia contributors, 23rd March, 2025). Coherence is critical for techniques that rely on interference and diffraction, as these processes require a stable phase relationship between different portions of the beam (SEES., 24th March, 2025). High spatial and temporal coherence contributes significantly to the resolution and sensitivity of imaging and spectroscopic experiments, making it possible to resolve features on the nanoscale range (Grabowski, M., *et al.*, 2021).

This coherence is a direct consequence of the well-controlled electron beam dynamics in a synchrotron, where the phase stability of emitted light is maintained across the entire beam (Deutsches Elektronen-Synchrotron (DESY)., 24th March, 2025). As a result, coherent synchrotron radiation is extensively used in techniques such as X-ray microscopy, interferometry, and holography, where the phase information is vital for reconstructing high-resolution images (Fonseca, M. D. C. *et al.*, 2018). Consequently, the coherence property not only enhances the imaging quality but also facilitates advanced data analysis methods that can yield more detailed insights into the underlying sample structure (Wikipedia contributors, 23rd March, 2025).

2.2.5 Polarization

Another distinctive attribute of synchrotron radiation is its polarization, which can be engineered to be either linear or elliptical depending on the configuration of the insertion devices (Deutsches Elektronen-Synchrotron (DESY)., 24th March, 2025). Polarization describes the orientation of the oscillating electric field vector in the electromagnetic wave and plays a crucial role in various spectroscopic methods (Deutsches Elektronen-Synchrotron (DESY)., 24th March, 2025). When the electrons in a synchrotron are accelerated in a plane, the emitted radiation is predominantly linearly polarized in that plane, which is fundamental for performing polarization-dependent X-ray absorption spectroscopy and scattering experiments (Wikipedia contributors, 23rd March, 2025).

Additionally, the precise control over polarization is often used to study magnetic properties, chemical bonding, and structural anisotropies in materials (Deutsches Elektronen-Synchrotron (DESY)., 24th March, 2025). By choosing the appropriate setup, researchers can investigate how different polarizations interact with samples, thereby unveiling information about electronic transitions and magnetic ordering at the atomic level (Grabowski, M., *et al*, 2021). The ability to produce highly polarized beams thus enhances the scientific utility of synchrotron sources by offering an additional experimental parameter for probing materials (Canon., 24th March, 2025).

2.2.6 Natural Collimation

Natural collimation refers to the inherent characteristic of synchrotron radiation to be highly directional and confined within a narrow angular spread (Deutsches Elektronen-Synchrotron (DESY)., 24th March, 2025). This is primarily due to relativistic effects, as the radiation emitted by electrons moving near the speed of light is concentrated into a sharp forward cone with an opening angle inversely proportional to the Lorentz factor (Deutsches Elektronen-Synchrotron (DESY)., 24th March, 2025). The superior collimation dramatically increases the photon flux density on the sample, thereby allowing sensitive experiments to be conducted on extremely small volumes (Mobilio, S., Boscherini, F., & Meneghini, C., 2016).

The precision afforded by this narrow beam is critical for applications in high-resolution X-ray imaging and micro-diffraction, where the ability to accurately target a minute region of a sample can be the difference between a successful experiment and one compromised by background noise (Hiden Analytical., 24th March, 2025). This natural collimation, combined with the high brightness, makes synchrotron radiation an ideal tool for investigations that require both spatial precision and significant photon flux.

2.2.7 Time-Resolved Capabilities

Synchrotron radiation is highly valued for its time-resolved capabilities, which enable the investigation of dynamic processes that occur on incredibly short timescales (Mills, D. M., 1991). The pulsed nature of the emitted light, a consequence of the discrete bunch structure of the circulating electron beam, allows researchers to capture transient phenomena during various physical, chemical, and biological processes (Deutsches Elektronen-Synchrotron (DESY)., 24th March, 2025). For instance, time-resolved X-ray diffraction experiments can monitor changes in the atomic or molecular structure during phase transitions, chemical reactions, or even muscle contractions (Huxley, H. E., Faruqi, A. R., Bordas, J., Koch, M. H. J., & Milch, J. R., 1980).

The ability to perform experiments in a time-resolved manner provides a window into the ultrafast dynamics of systems, revealing reaction intermediates and transient states that are often inaccessible with continuous wave sources (Mills, D. M., 1991). This temporal resolution is critical for understanding complex processes and can lead to breakthroughs in fields ranging from materials science to biochemistry (Nambu, A., Yoneyama, A., Takamatsu, D., Konishi, K., & Fujita, R., 2019). As a result, synchrotron facilities are at the forefront of research that demands the capture of rapid changes in experimental systems (Mills, D. M., 1991).

2.2.8 High Spatial Resolution

The exceptional brightness and coherence of synchrotron radiation contribute directly to its high spatial resolution capabilities (Grabowski, M., Cooper, D. R., Brzezinski, D., Macnar, J. M., Shabalin, I. G., Cymborowski, M., ... & Minor, W., 2021). High spatial resolution techniques, such as X-ray tomography and scanning X-ray microscopy, benefit from the small beam size and excellent collimation of synchrotron sources, allowing researchers to resolve structural details at the nanometer scale (Fonseca, M. D. C., Araujo, B. H. S., Dias, C. S. B., Archilha, N. L., Neto, D. P. A., Cavalheiro, E., ... & Franchini, K. G., 2018).

These capabilities have been instrumental in the study of intricate biological structures, advanced materials, and complex nanostructures in semiconductor devices (Mobilio, S., Boscherini, F., & Meneghini, C., 2016). For example, high-resolution X-ray microtomography has been used to image whole neurons in the brain, providing three-dimensional reconstructions that reveal previously unseen structural intricacies (Fonseca, M. D. C., Araujo, B. H. S., Dias, C. S. B., Archilha, N. L., Neto, D. P. A., Cavalheiro, E., ... & Franchini, K. G., 2018). This ability to obtain high spatial detail is also critical for determining the atomic arrangements in crystal structures, thereby facilitating a deeper understanding of material properties and biological functions (Grabowski, M., Cooper, D. R., Brzezinski, D., Macnar, J. M., Shabalin, I. G., Cymborowski, M., ... & Minor, W., 2021).

2.2.9 Non-Destructive Analysis

A significant advantage of many synchrotron-based techniques is their inherently non-destructive nature, which allows samples to be examined without incurring any damage or alteration (Wikipedia contributors, 23rd March, 2025). Techniques such as X-ray diffraction (XRD) and X-ray absorption spectroscopy (XAS) are designed to probe the structural and electronic properties of materials without compromising their integrity (Wikipedia contributors, 23rd March, 2025). This is particularly important when dealing with rare, valuable, or delicate samples such as archaeological artifacts and biological tissues, where preserving the sample is of paramount importance (Grabowski, M., *et al*, 2021).

The non-destructive character of these methods not only ensures that the specimen remains intact for further analysis but also allows for repeated measurements over time to monitor dynamic changes (Nambu, A., Yoneyama, A., Takamatsu, D., Konishi, K., & Fujita, R., 2019). Moreover, minimal exposure to high-intensity radiation is meticulously managed in synchrotron facilities to further protect sensitive materials from radiation-induced damage (Wikipedia contributors, 23rd March, 2025). Such non-invasiveness broadens the range of applications for synchrotron radiation, extending its use into fields where sample quantity is extremely limited (Deutsches Elektronen-Synchrotron (DESY)., 24th March, 2025).

2.3 Physics Principles of the Synchrotron

2.3.1 The synchrotron ring

Most synchrotron radiation research programs operated primarily as parasitic or secondary efforts, using the radiation produced during high-energy physics operation of storage rings and radiations (Willmott, P., 2019). With increasing interest in synchrotron radiation research, the former largely parasitic roles has changed. New storage rings dedicated only to synchrotron radiation research operation are now available.

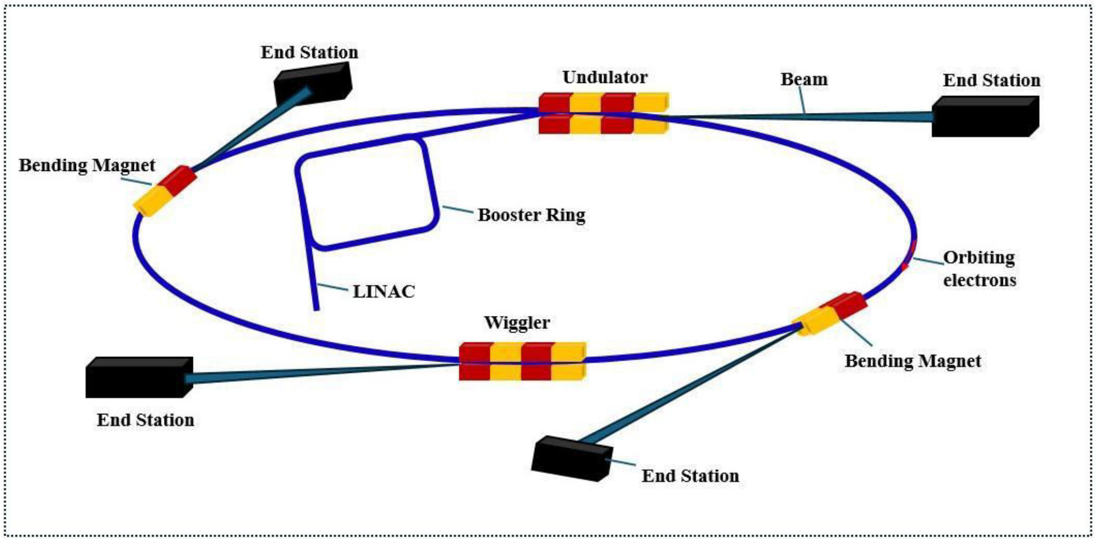

Figure 2.1: The basic elements of a storage ring designed as a dedicated synchrotron radiation source.

The most capable source of synchrotron radiation is the storage ring. The basic elements of a storage ring designed as a dedicated synchrotron radiation source (Wiedemann, H., 2003) are shown in Figure 2.1.

The deflection of a relativistic particle beam results in the emission of electromagnetic radiation, observed in the laboratory frame as broadband and highly collimated in the forward direction (Sanchez, E. R., *et al*, 2019). During this deflection, the emission direction sweeps across the observer's detection apparatus, similar to a searchlight. The brief duration of the detectable radiation pulse leads to the observation of a broad spectrum consisting of multiple harmonics of the beam's revolution frequency (Alonzo, C. A., Gather, M. C., Kang, J. W., Scarcelli, G., & Yun, S. H., 2016).

The spectrum's width is defined by the critical photon energy, which is determined solely by the particle's energy and the bending radius of the magnet. In practical scenarios, such radiation is generated using bending magnets in a storage ring, where the electron beam circulates for extended periods (Bosch, R. A., May, T. E., Reininger, R., & Green, M. A.,1996).

The electrons are produced in the injection system which comprises of a thermionic gun, RF buncher and a Linear accelerator (LINAC) system (Kutsaev, S. V., 2021). The electrons travel in a single bunch (High energy) or train of bunches (high energy) of approximately 100 MeV. The electrons are then directed to the booster ring in which the energy of the electrons is ramped to GeV scales by magnets and RFs. The emmittance of the electrons to the storage ring control the injection efficiency. Finally, the relativistic electrons are injected to the storage ring using direct current (DC) and pulsed electro-magnets considering the optics matching, collimation and other diagnostics (Aiba, M., 2018; Mulhaupt, G., 1995).

2.3.2 Production of radiations in the storage ring

To produce x-ray radiations from the storage rings, magnets called insertion devices are incorporated at given points on the storage ring. They are used to provide synchrotron radiation with the flexibility to adjust source parameters. (Hwang, C. S., Jan, J. C., Chang, C. S., Chen, S. D., Chang, C. H., & Uen, T. M., 2011; Willmott, P., 2019). The insertion devices include the wavelength shifters bending magnets, undulators and wiggler magnets described.

a. Wavelength Shifter

Wavelength Shifters are magnets that periodically deflect the beam in such a way that the total deflection angle cancels out (shown in Figure 2.2), as expressed by the equation 2.1.

$$\int_{-\infty}^{\infty} \vec{B}_y(y = 0, z)\, dz = 0 \qquad 2.1$$

where $\overrightarrow{B_y}$ is the unidirectional magnetic field, *y, z* represent the degrees of freedom and and *dz* in the differential element in the *z* space.

In low-energy storage rings, a wavelength shifter - typically implemented as an insertion device - is used to generate higher-energy (harder) X-ray radiation (Weihreter, E., & Wuestefeld, G., 1999). This device often consists of three or more dipole magnets with alternating magnetic field directions. Due to this configuration, a wavelength shifter is considered a true insertion device (Hwang, C. S., Jan, J. C., Chang, C. S., Chen, S. D., Chang, C. H., & Uen, T. M., 2011 ; Willmott, P., 2019). Figure 2.2 provides a schematic representation of a three-pole wavelength shifter (Hwang, C. S., Wang, B., Wahrer, B., Taylor, C., Chen, C., Juang, T., ... & Hsiung, G. Y., 2007). However, this was an ancient technology used in the first-generation synchrotrons and in modern light sources they are not widely used (Bilderback, D. H., Elleaume, P., & Weckert, E., 2005; Willmott, P., 2019).

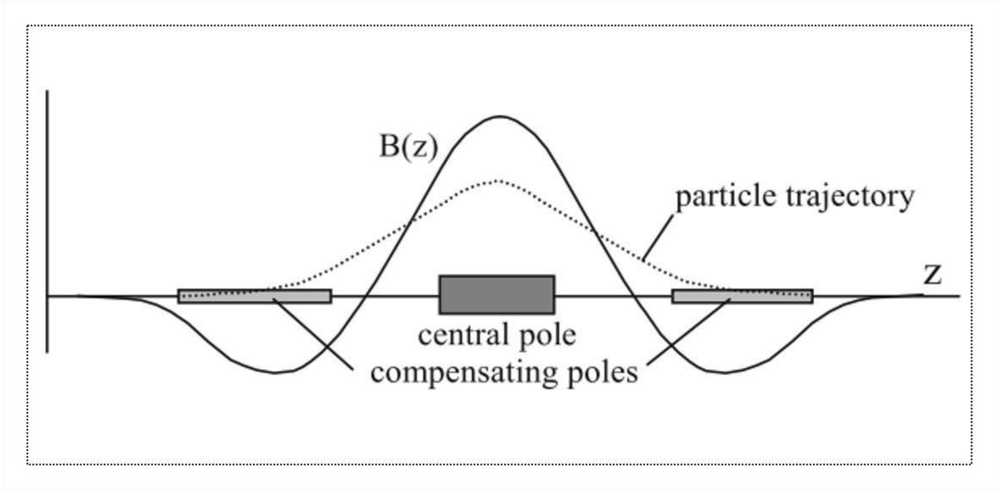

Figure 2.2: Magnetic field variation along the beam path in a wavelength shifter (Winick, H., & Doniach, S., 2012).

b. Bending Magnet

Radiations from bending magnets are the simplest type of radiation source (Kim, K. J., 1989). This appears when strong magnet are inserted along the storage ring, making their dipoles to force the electrons to circulate in the ring (Danby, G. T., Addessi, L., Armoza, Z., Benante, J., Brown, H. N., Bunce, G., ... & Redin, S. I., 2001). Whenever this happens, radiations are emitted tangentially to the orbit, much like a searchlight, while remaining highly collimated in the non-deflecting or vertical plane (Wiedemann, H., 2003). The radiation from bending magnets is emitted tangentially from points along the curved path, creating a swath of radiation around the storage ring, as illustrated in Figure 2.3 and in the schematic diagram in Figure 2.1.

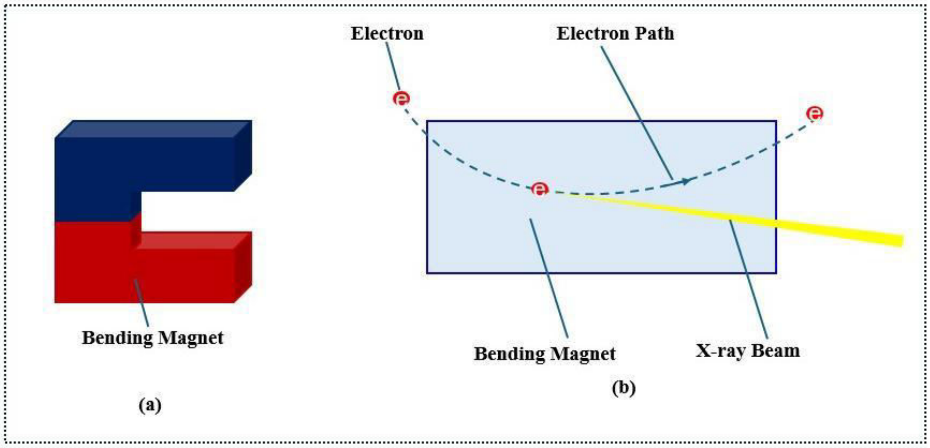

Figure 2.3: Radiation emitted from bending magnets in an electron storage ring; a) shows the bending magnet inserted in the ring b) the electron path and the tangentially emitted radiation.

c. Undulator

An undulator is another type of insertion device in which the electron beam is periodically deflected from its path by weak, sinusoidally varying magnetic fields (see Figure 2.4) (Schlueter, R. D., 1994; Levichev, E., & Vinokurov, N., 2010). These deflections create periodic disturbances in the electric field lines. A detector that measures the electric field identifies the periodic variation in the transverse electromagnetic field components, interpreting this as quasi-monochromatic radiation (Li, Y., Yang, Q., & Tian, Y., 2024).

The relativistic electrons in an undulator behave as well collimated flashlights, causing their emitted wavelength a spectrum. The stronger magnetic field, $\vec{B}$, increases the transverse electron oscillations and their transverse speed, proportional to, $\vec{B}$. The undulators enable different wavelengths emission, have very small angular spread, and with very high brightness (Farge, Y. (1980).

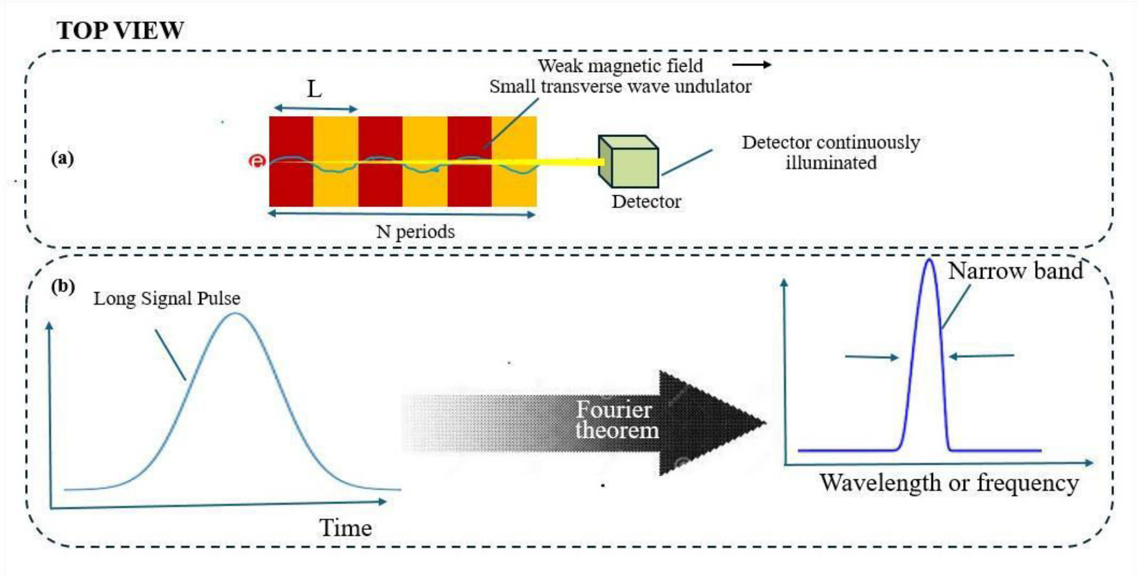

Figure 2.4: An undulator with the electron beam periodically deflected from its path by weak, sinusoidally varying magnetic fields with transformation by Fourier theorem.

d. Wiggler Magnet

Increasing the magnetic field strength in an undulator causes the electron's pure sinusoidal transverse motion to be altered by relativistic effects, such as transverse Lorentz contraction, which distorts the motion (Schlueter, R. D., 1994; Levichev, E., & Vinokurov, N., 2010). These distortions generate higher harmonics in the radiation spectrum. As the magnetic field strength increases, many harmonics are produced, eventually merging into a continuous spectrum that ranges from infrared to hard X-rays.

At this stage, the source magnet is referred to as a wiggler magnet. A wiggler, as an undulator, is a periodic magnet array, but its magnetic field is stronger and causes larger transverse oscillations of the electrons, generating multiple pulses hence stronger emission (Winick, H., Brown, G., Halbach, K., & Harris, J., 1981) as seen in Figure 2.5.

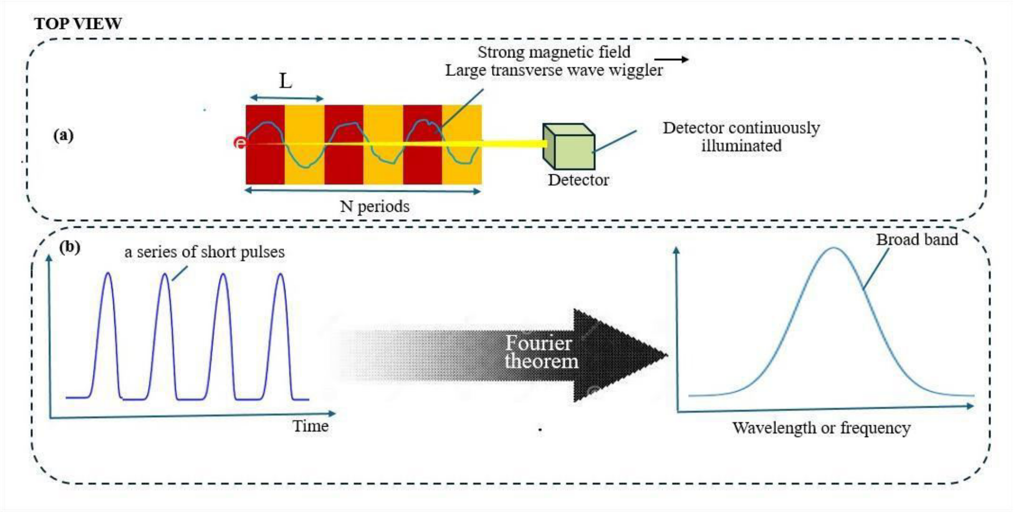

Figure 2.5: Wiggler causing larger transverse oscillations of the electrons, generating multiple pulses; hence, stronger emission.

2.4 The Synchrotron at the Advanced Light Source.

The Advanced Light Source (ALS) is a specialized particle accelerator that generates bright beams of x-ray light for scientific research (Schneider, J. R., 2010;Tamura, L., Hussain, Z., Padmore, H. A., Robin, D. S., Bailey, S., Feinberg, B., & Falcone, R. W., 2012). Electron bunches travel at nearly the speed of light in a circular path, emitting ultraviolet and x-ray light in the process. The light is directed through about 40 beamlines (Robin, D. *et al*., 2005), as shown in Figure 2.6, to the numerous experimental end-stations. Research including materials science, biology, chemistry, physics, and the environmental sciences is conducted here.

The wavelengths of the synchrotron light span the electromagnetic spectrum from infrared to x-rays and have the right size and energy range for examining the atomic and electronic structure of matter (Cramer, S. P., 2020).

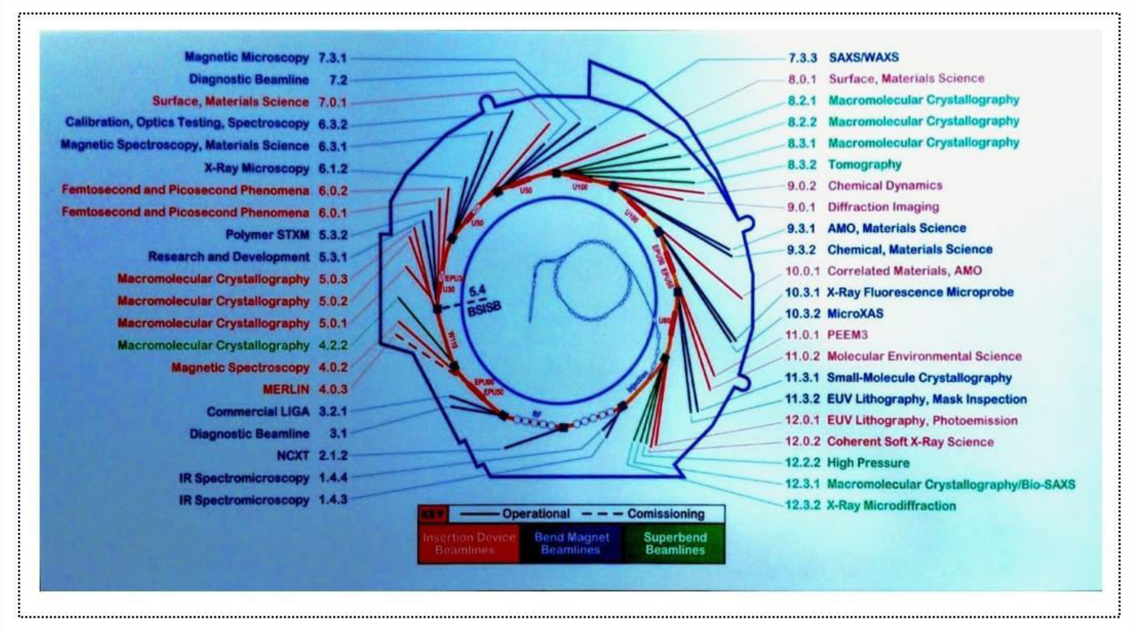

Figure 2.6: ALS beamlines ranging from scattering to diffraction and imaging.

The Advanced Light Source (ALS) is divided into two primary research groups: Photon Science and Accelerator Physics. The Photon Science Group (PSO) includes various programs, such as Angle-Resolved X-ray Photo-electron Spectroscopy (APXPS) & Chemical Sciences, Angle-Resolved Photo-emission Spectroscopy (ARPES), Dichroism, Diffraction & Imaging, Infrared, Microscopy, Resonant Inelastic X-ray Scattering (RIXS), and Scattering. For this thesis, we will focus on Diffraction & Imaging, specifically the Grazing Incidence Wide/Small Angle X-ray Scattering (GIWAXS/GISAXS) and Micro-diffraction techniques.

2.4.1 GIWAXS/GISAXS Scattering

X-Ray Scattering is an essential area of investigation in several scientific domains, from materials science to biological research. This technique has provided valuable insights into the structure and properties of various materials at a molecular level. What makes it an exciting area of research is the plethora of complex phenomena it illustrates at an atomic and subatomic level (Advanced Light Source (ALS), 24th March, 2025).

X-ray scattering is a physical phenomenon where an incoming X-ray beam deviates from its original path due to non-uniformities in the medium it passes through (Greaves, A. W. (2011). When a synchrotron X-ray beam strikes a sample, the atoms within the material cause the electrons to "ripple," emitting secondary radiations similar to how ripples spread outward when a pebble is thrown into water (Hobson, A., 2016).

X-ray scattering is broadly categorized into Coherent (Rayleigh) Scattering, and Compton Scattering (Mishra, R. K., Cherusseri, J., Allahyari, E., Thomas, S., & Kalarikkal, N., 2017; Narayanan, T., 2014). Coherent Scattering occurs when the scattered X-rays retain the same energy as the incoming beam. It is more prevalent at lower X-ray energies and with lighter elements. In contrast, Compton Scattering involves a change in the energy of the X-ray due to interaction with electrons (Cooper, M., Mijnarends, P., Shiotani, N., Sakai, N., & Bansil, A., 2004). Both scatterings could either be Small Angle X-ray Scattering (SAXS), or Wide-Angle X-ray Scattering (WAXS).

Wide Angle X-ray Scattering (WAXS) probes atomic-scale structures, providing crystallographic information about the sample (Schlipf & Müller-Buschbaum, 2017). Small Angle X-ray Scattering (SAXS) is surface-sensitive, owing to its grazing incidence, and explores mesoscale structures (1–1000 nm), making it ideal for studying crystallization and sample morphology (Erdemir *et al*., 2009; Rodríguez-Hornedo & Murphy, 1999). SAXS combined with fast two-dimensional detectors and synchrotron radiation enables *in situ* studies, providing dynamic insights into materials' growth processes. From GISAXS scattering curves, parameters such as particle sizes, shapes, distances, and correlations can be derived (Li, Senesi, & Lee, 2016), offering crucial information on nucleation and growth during temperature-controlled annealing (Renaud, Lazzari, & Leroy, 2009).

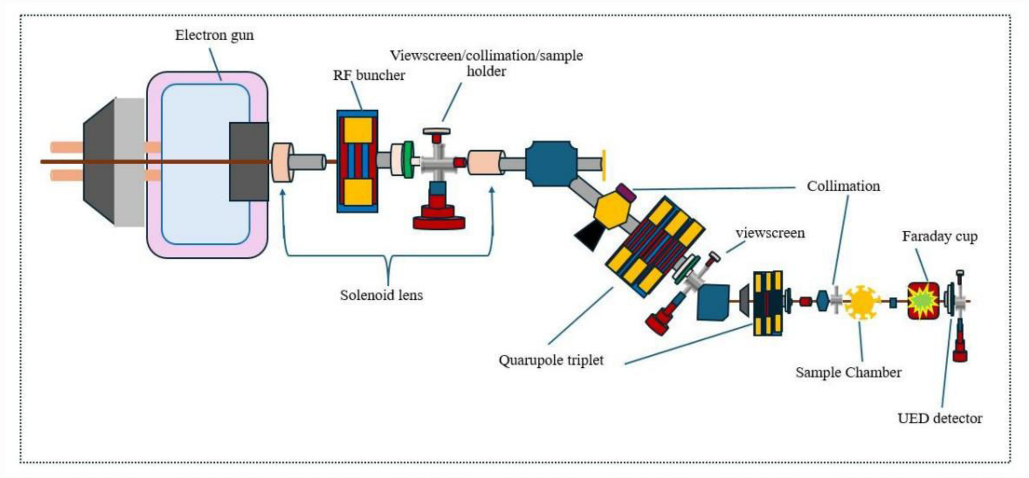

Figure 2.7: A schematic SAXS/WAXS diagram used to characterize the structure and interactions of nanomaterials and their complexes.

WAXS, as shown in Figure 2.7, is increasingly employed for characterizing the structure and interactions of nano-materials and their complexes. The phase and magnitude of the resulting diffraction pattern depend on the size, shape, and electron density of the atoms and the scattering angle (θ). Like SAXS, WAXS leverages differences in electron density for contrast and is less dependent on imaging conditions compared to other microscopy techniques. This method is grounded in Bragg's law (equation 2.2), which governs the relationship between X-ray scattering and crystal structure (Bragg, W. H., & Bragg, W. L., 1915).

$$q = \frac{2\pi}{d} \tag{2.2}$$

Where $d = \frac{n\lambda}{2\sin\theta}$; n represents the order of reflection, λ is the X-ray wavelength, d is the inter-planar spacing, and θ is the scattering angle. By varying θ, the conditions for constructive interference change, allowing us to probe different lattice planes within a crystal. This enables the extraction of detailed information about the crystal structure and orientations in the sample. In this study, WAXS is employed to identify the inherent phases present at each stage of perovskite crystallization, including the smallest structural features of the material.

2.4.2 Micro-diffraction and Imaging

Techniques like micro-diffraction and imaging-based diffraction methods allow detailed analysis of crystallographic properties, strain distributions, grain orientations, and phase transitions. These methods are ideal for studying thin films, nanostructures, and other complex materials, providing critical insights into their structural and functional properties (Thomas, O., Labat, S., Cornelius, T., & Richard, M. I., 2022).

Micro-diffraction is a powerful technique that focuses an X-ray beam to a very small spot size, typically a few microns (1 μm) or smaller, enabling high-resolution mapping of structural information across a sample. This capability makes it particularly useful for studying complex materials with heterogeneous properties. One of its key advantage is its high spatial resolution, which allows precise examination of localized regions within a sample (Aspinall, R. J., Marcus, W. A., & Boardman, J. W., 2002). This feature is ideal for analyzing grain structures, interfaces, and defects in various materials (van Benthem, K., Krämer, S., Sigle, W., & Rühle, M., 2002).

Another strength of micro-diffraction is its ability to provide crystallographic analysis, offering detailed information on lattice parameters, orientation, strain, and phase distributions (Korsunsky, A. M., Hofmann, F., Abbey, B., Song, X., Belnoue, J. P., Mocuta, C., & Dolbnya, I., 2012). Additionally, the technique is non-destructive, requiring minimal sample preparation, thereby preserving the integrity of the material under investigation. Furthermore, it supports dynamic studies, making it possible to observe structural changes in real-time during processes like heating, cooling, or applying mechanical stress in *in situ* or *operando* setups (Jungjohann, K., & Carter, C. B., 2016)

At the Advanced Light Source (ALS), beamline 12.3 .2 is specifically optimized for micro-diffraction applications. It provides high-resolution capabilities and allows coupling of measurements with controlled environmental conditions such as temperature, pressure, and chemical reactions, making it a versatile tool for advanced material research. It employs Laue and powder diffraction patterns in the material analysis.

Laue Diffraction is a non-destructive technique for determining the crystallographic orientation of single crystals and analyzing structural properties such as strain, symmetry, and defects. It uses a stationary single crystal and a polychromatic X-ray beam, producing a diffraction pattern that reveals the crystal's orientation and lattice structure (Ice, G. E., & Pang, J. W., 2009). This method is efficient, requires minimal sample preparation, and is particularly valuable for studying complex structures, mapping orientation relationships in polycrystalline materials, and assessing strain and defects (Zhang, F., 2015).

Powder Diffraction is a key crystallographic technique for analyzing crystalline materials. It examines finely ground samples with randomly oriented crystallites, ensuring comprehensive sampling of all crystallographic planes (Ali, A., Chiang, Y. W., & Santos, R. M., 2022). A monochromatic beam produces concentric diffraction rings, analyzed to determine lattice parameters, crystal structure, phase composition, and microstructural details like crystallite size and strain. Widely used for phase identification, it compares patterns to databases like ICDD and provides insights into unit cell dimensions and phase composition. Figure 2.8 shows the micro-diffraction beamline at ALS (Tamura N. *et al*., 2009). Applications span material science, pharmaceuticals, geology, and nanotechnology, making it invaluable for studying diverse materials and their structural properties.

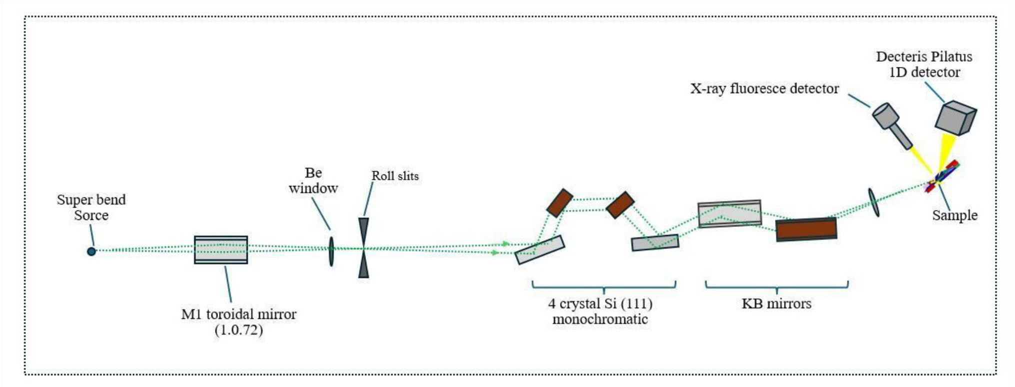

Figure 2.8: The micro-diffraction beamline at ALS: (a) the elevation view and (b) the plan view of the Beamline.

2.5 Physics of radiations and matter

2.5.1 Interaction of radiations with matter

X-ray diffraction experiments rely on elastic scattering events, although some electromagnetic radiation can also undergo inelastic scattering, as well as absorption and emission (Als-Nielsen, J., & McMorrow, D., 2011; Willmott, P., 2019). For instance, although metal halide perovskites typically contain relatively heavy Lead atoms, metallic lead is well known as an effective X-ray shielding material and exhibits strong X-ray luminescence, which can be detected as background noise.

When combined with a high-brilliance light source, the dose of ionizing radiation can become significant and must be controlled to minimize beam damage (Habs, D., & Köster, U., 2011). As the compositional range of metal halide perovskites expands and the exploration of doping elements and hybrid organic-inorganic structures becomes more complex, these interactions are increasingly important to consider. (Steele, J. A. *et al.*, 2023)

2.5.2 Physics of Scattering

In contrast to scattering from a free electron, the amplitude of X-rays scattered by the electrons in a given atomic shell is represented by the atomic scattering factor, f_a. As a result, f_a not only scales with the number of electrons in an atom but also with their density, meaning that charged ions with the same atomic number (Z) will have different form factors. During scattering, electrons oscillate to form a dipole, emitting a spherical wave. The difference between the incoming and outgoing ($\overrightarrow{k_i}$ and $\overrightarrow{k_f}$) wave-vectors defines the resulting scattering vector given in equation 2.4 (Steele, J. A. *et al.*, 2023).

$$\vec{q} = \vec{k}_f - \vec{k}_i \qquad 2.4$$

The value of f_a reaches a maximum when the scattering is in the same direction as the incident X-rays. Atomic scattering factors are calculated via a Fourier transform of the atomic electron density (equation 2.5) , with their values found in the International Tables for Crystallography, Volume C (Prince, E., 2006).

$$f_a(q) = \int \rho(r) e^{-eiqr}\, dr \qquad 2.5$$

Here, $\rho_{(r)}$ represents the electronic density around the atom, and r is the distance from the center of mass. As $q \rightarrow 0, f_a \rightarrow Z$, and as $q \rightarrow \infty, f_a \rightarrow 0$. Thus, the scattering amplitude at a given q is directly related to both the X-ray wavelength/energy and increases with Z. For a diffracting crystal, the structure factor P sums the atomic scattering factors for the various, N, elements in a unit cell at position R_j illustrated in equation 2.6 (Steele, J. A. *et al.*, 2023).

$$P = \sum \mathrm{j} = 1\mathrm{e}^{-\mathrm{iqR_j}} \qquad 2.6$$

The intensity of scattered radiation, $I(q)$, for crystals is proportional to the square of the form factor P and is given by equation 2.7.

$$I(q) = |P|^2 \times \mathrm{t_y} \times A \qquad 2.7$$

where A accounts for X-ray absorption, and t_y includes geometric and polarization factors at the beamline. The reflection multiplicity, which is the number of symmetry-equivalent reflections contributing to a single observed peak, also affects the observed intensity (Steele, J. A. *et al.*, 2023).

2.5.3 Physics of Absorption

X-ray absorption refers to the attenuation of the beam within the material, typically described by equation 2.8.

$$I_t = I_0 e^{-\mu d} \qquad 2.8$$

where I_t and I_0 are the transmitted and incident intensities, respectively, and d is the material thickness. The linear absorption coefficient, μ, depends on material density and can be converted to the mass attenuation coefficient by dividing by the material density, ρ (Steele, J. A. *et al*., 2023).

The parameter, μ encompasses all X-ray attenuation effects, including elastic and inelastic scattering, as well as photoelectric absorption and, μ scales significantly with Z. For lower X-ray energies (like, below 50 keV, depending on the material), the total mass absorption is dominated by the photoelectric effect (Fultz, B., & Howe, J. M., 2012).

2.5.4 Physics of Emission

Following X-ray photoelectric absorption, a secondary result is X-ray emission. After being energized into an excited state, characteristic X-rays are emitted as outer shell electrons in excited atoms lose energy and transition to lower energy states. This process is known as X-ray fluorescence (XRF). XRF emits radiation in all directions from the excited sample volume, effectively acting as a local *X*-ray photon source.

The ability of XRF to penetrate through the material and reach the detector depends on the energy of the emitted *X*-rays. Heavier elements like Pb (Z = 82) and Sn (Z = 50) produce X-rays with higher energies, allowing them to pass through large distances within the sample. In contrast, lighter elements like carbon produce X-rays with lower energies (Steele, J. A. *et al*., 2023).

While X-ray emission lines can serve as atomic fingerprints for chemical identification (Zschornack, G. H., 2007), they can also raise the background intensity in the detector. Therefore, selecting an X-ray energy above the absorption edge of a high-Z element can be problematic, as detectable XRF signals can introduce excess noise and reduce the quality of the data. Thus, XRF-related signals should be minimized to ensure high-quality measurements (Steele, J. A. *et al*., 2023).

2.5.5 Peak interpretation from GIWAXS diffraction data

To accurately identify the peaks observed in the diffraction patterns, it is first necessary to determine the tolerance factor (*t*) (Bakar, A. *et al*., 2022), as outlined in Equation 2.3, to establish whether the material adopts a cubic or hexagonal structure. Once the *t* factor is determined, we proceed with the peak assignment process. Assuming a cubic perovskite structure, such as $CsFAPbI_3$, the lattice constant is first determined, for example, $a = 6.3$ Å.

Using the standard cubic formula for d-spacing in equation 2.9;

$$d_{hkl} = \frac{a}{\sqrt{h^2+k^2+l^2}} \qquad 2.9$$

where a is the lattice constant and (*hkl*) are the Miller indices, then theoretical d-spacing values are calculated for values of h,k,l (Afzal, U., 2024; Hasan, S. G. A. *et al.*, 2021) These values are compared with calculated d-values derived from the measured q-values calculated from the relationship in equation 2.10.

$$\mathrm{d} = \frac{2\pi}{q} \qquad 2.10$$

By fitting appropriate (*hkl*) indices to the measured d-values, we identify the corresponding crystal planes. For instance, using the (100) plane as an example, a diffraction peak at $q = 1.0$ Å^{-1} closely matches the expected (100) reflection for a cubic perovskite with a lattice constant of 6.3 Å (Contreras-Torres, F. F., 2019). In comparison, a peak at $q = 0.9$ Å^{-1} corresponds to a larger calculated d-spacing (6.98 Å), which suggests possible lattice expansion, strain-induced shifts, slight distortions from the ideal cubic symmetry, or contributions from superstructure reflections typical in layered 2D perovskites or possible presence of PbI_2 (Liu, J., (2019).

PEACl on the other hand is a tetragonal shaped molecule with lattice parameters a = b = 8.95 Å, and c = 16.78 Å. The d-spacing formula for the tetragonal crystal system is as given in equation 2.11.

$$d_{hkl} = \frac{1}{\sqrt{\left(\frac{h^2+k^2}{a^2}\right)+\left(\frac{l^2}{c^2}\right)}} \qquad 2.11$$

For miller index (200), d_{002} is approximately 8.39Å, which matches the type low-angle XRD peaks seen in 2D layered hybrid perovskites.

2.6 Applications of Synchrotron Radiations Across Disciplines

In the following sections, we describe the specific disciplines in which the synchrotron radiations are applied.

2.6.1 Contemporary Research

Today, synchrotron radiation is applied to a myriad of disciplines that span engineering, healthcare, cultural heritage, and environmental science (Fenter, P. A., Rivers, M. L., Sturchio, N., & Sutton, S. R., 2018). In the field of engineering, synchrotron light is used for high-resolution imaging and spectroscopy, enabling a detailed analysis of material properties and stress distributions in critical components (Fenter, P. A., Rivers, M. L., Sturchio, N., & Sutton, S. R., 2018). In health care, synchrotron-based techniques have paved the way for advanced imaging modalities that provide higher spatial resolution and contrast than conventional imaging, significantly improving diagnostic accuracy in medical applications such as mammography, computed tomography, and X-ray microscopy (Tamal, M., Althobaiti, M., Alomari, A. H., Dipty, S. T., Suha, K. T., & Al-Hashim, M., 2022).

Additionally, synchrotron X-ray radiation has proven instrumental in bone research, helping scientists to investigate the aging process, detect early stages of osteoporosis, and evaluate treatments designed to enhance bone strength and resilience (Takeda, T., Itai, Y., Hyodo, K., Ando, M., Akatsuka, T., & Uyama, C. (1998;Xiao, C., Zhang, J., Li, Y., Xie, M., & Sun, D.,2025). Environmental scientists benefit from these facilities by using synchrotron techniques to analyze trace elements and chemical states in complex matrices, which is essential for monitoring pollutants and understanding nutrient dynamics in ecosystems (Fenter, P. A., Rivers, M. L., Sturchio, N., & Sutton, S. R., 2018).

Moreover, synchrotron radiation has found applications in the conservation and analysis of cultural heritage artifacts, where non-destructive imaging techniques are used to uncover hidden structures and compositions of historical objects. The unparalleled brightness and broad spectral range of synchrotron light make it an indispensable tool for cutting-edge research that addresses some of the most challenging problems across science and technology (Takeda, T., Itai, Y., Hyodo, K., Ando, M., Akatsuka, T., & Uyama, C., 1998).

2.6.2 Pure and basic science

The unique combination of properties exhibited by synchrotron radiation has propelled it to the forefront of scientific discovery across multiple fields. In physics and materials science, for example, the high-intensity, tunable, and well-collimated beams are used to examine crystalline structures, detect phase transitions, and assess mechanical properties at a micro-to nanoscale resolution (Hiden Analytical., 24th March, 2025). These beams enable detailed studies using techniques such as X-ray diffraction, small-angle scattering, and X-ray fluorescence, which are essential for the development of new materials as well as optimization of existing ones (Deutsches Elektronen-Synchrotron (DESY)., 24th March, 2025).

In the realm of biology, synchrotron radiation has revolutionized macromolecular crystallography by providing the high-resolution data necessary to determine the atomic structures of proteins, nucleic acids, and viral particles (Grabowski, M., Cooper, D. R., Brzezinski, D., Macnar, J. M., Shabalin, I. G., Cymborowski, M., ... & Minor, W., 2021). The ability to collect data rapidly and with minimal sample damage has led to substantial advances in drug discovery and structural biology, as over 70% of macromolecular structures deposited in the Protein Data Bank have been determined using synchrotron sources (Wikipedia contributors, 23rd March, 2025). In structural biology, the high brilliance and tunability have enabled researchers to elucidate complex protein structures and molecular assemblies, fueling advances in drug discovery and biochemical research (Li, F., Liu, R., Li, W., Xie, M., & Qin, S., 2024; Renaud, J. P. (Ed.)., 2020).

Furthermore, in chemistry, synchrotron radiation facilitates spectroscopic studies that reveal the electronic structures and reaction mechanisms of complex chemical systems, thereby offering insights that help drive innovation in synthetic and environmental chemistry (Hiden Analytical., 24th March, 2025).

2.6.3 Broader Impact on Scientific Research

The diverse attributes of synchrotron radiation have redefined many research fields by offering capabilities that were previously unattainable with conventional sources. In materials science, the precision and non-destructive nature of synchrotrons techniques have facilitated *in situ* studies of phase transitions, strain, and defect dynamics, thereby accelerating the development of novel materials with enhanced performance characteristics (Silva, M. I., Malitckii, E., Santos, T. G., & Vilaça, P., 2023). Environmental science and geochemistry also benefit from the element-specific sensitivity of synchrotron-based X-ray spectroscopy, leading to improved understanding of complex ecosystems and the behavior of pollutants in natural systems (Luo, L., & Zhang, S., 2010).

Additionally, cultural heritage studies have utilized synchrotron imaging to analyze and conserve priceless artworks and historical artifacts by revealing subsurface structures and compositional details without inflicting damage (Tamura, N., Dejoie, C., & Martinetto, P., 2024.; Dejoie, C., Martinetto, P., & Tamura, N., 2024). The broad spectrum and tunability of the radiation empower experiments that require both macro- and microscopic investigations of matter, thereby bridging the gap between fundamental research and practical applications (Mino, L., Borfecchia, E., Segura-Ruiz, J., Giannini, C., Martinez-Criado, G., & Lamberti, C., 2018).

2.6.4 Integration in Multi-Modal Research

Synchrotron facilities are frequently integrated into multi-modal research centers that combine a variety of experimental techniques - from X-ray crystallography and electron microscopy to spectroscopic and scattering methods - to provide a comprehensive understanding of biological and material systems (Su, B., Li, J., Deng, B., Pianetta, P., & Liu, Y., 2024). This integration is pivotal in collaborative research environments where data from different techniques are combined to create a holistic picture of the sample under investigation. For example, multimodal platform has been instrumental in advancing the understanding of thin-film formation dynamics. For instance, studies have utilized it to reveal how lead precursors influence perovskite crystallization pathways, identifying conditions that lead to undesirable morphologies and reduced device performance. Such insights are critical for developing more efficient and stable photovoltaic materials (Song, T. B., *et al.*, 2020). Conversely, the combination of high-resolution synchrotron X-ray diffraction and cryo-electron microscopy has been particularly successful in the field of macromolecular biology, enabling detailed structural analysis of large protein complexes that are challenging to resolve with a single technique alone (Vénien-Bryan, C., Li, Z., Vuillard, L., & Boutin, J. A., 2017).

Such multi-modal approaches not only enhance the accuracy of the scientific conclusions drawn but also foster interdisciplinary collaborations that drive innovation across traditional boundaries. The advent of hybrid research facilities underscores the growing realization that the complexity of modern scientific challenges demands the integration of complementary techniques, with synchrotron radiation playing a central role in this endeavor (Li, Y., Wei, R., Dong, L., Guo, S., & Li, Z., 2023).

2.6.5 Impact on Scientific Research and Industry

The advent and successive evolution of synchrotron light sources have left an indelible mark on scientific research and industrial applications alike (Fenter, P. A., Rivers, M. L., Sturchio, N., & Sutton, S. R., 2018). In material science, synchrotron-based techniques have become central to the design and testing of new materials with engineered properties, leading to breakthroughs in nanotechnology, semiconductors, and superconductors (Fenter, P. A., Rivers, M. L., Sturchio, N., & Sutton, S. R., 2018). In the pharmaceutical industry, X-ray crystallography enabled by synchrotron radiation has been crucial in the determination of drug-target interactions, thereby accelerating the development of novel therapeutics and vaccines (Takeda, T., Itai, Y., Hyodo, K., Ando, M., Akatsuka, T., & Uyama, C., 1998).

Structural biologists extensively rely on high-resolution diffraction data from synchrotron sources to elucidate the three-dimensional structures of complex biomolecules, which is key to understanding their function and in devising strategies for medical intervention (Clegg, W., 2019). The precise and rapid analysis capabilities of synchrotron facilities have also fostered innovations in environmental monitoring, such as tracking the mobility of heavy metals and metalloids in contaminated soils and water systems (Fenter, P. A., Rivers, M. L., Sturchio, N., & Sutton, S. R., 2018). Across a range of sectors, from aerospace engineering to renewable energy, synchrotron light is used to interrogate the structural and electronic properties of materials, driving innovation and competitive advantage in technology development (Winick, H., 1994).

2.7 Technological Innovations and Instrumental Developments

Technological progress continues to expand the frontiers of synchrotron radiation applications. Recent innovations in detector technologies, beamline instrumentation, and data processing algorithms have substantially improved spatial and temporal resolution, alongside overall data quality (Deutsches Elektronen-Synchrotron [DESY], 2025). The development of pixel array and hybrid pixel detectors has facilitated faster, lower-noise data acquisition, enabling high-throughput structural analysis with enhanced precision (Grabowski et al., 2021). These detectors, when coupled with real-time data processing, allow for near-instantaneous analysis and visualization of results, significantly accelerating experimental workflows (DESY, 2025).

As synchrotron facilities evolve toward fourth-generation light sources—marked by higher brightness and improved coherence—the breadth of scientific inquiry is expected to expand dramatically (DESY, 2025). These sources are poised to drive breakthroughs in ultrafast chemical reaction dynamics, nanoscale imaging of biological systems, and real-time industrial process monitoring (Mills, 1991). Researchers anticipate that these advancements will not only refine existing techniques but also enable novel experimental methodologies tailored to exploit the unique properties of synchrotron radiation (DESY, 2025).

In parallel, architectural innovations such as high-brightness storage ring lattices have significantly enhanced beam quality and stability, further broadening the range of experimental capabilities (Winick, 1994). Modern beamlines, equipped with state-of-the-art monochromators, focusing systems, and detectors, now achieve unprecedented precision in both spatial and temporal domains (Winick, 1994). Dedicated beamlines for single-crystal diffraction have been optimized to accommodate a wide spectrum of sample types, from biological macromolecules to advanced engineered materials, enabling *in situ* and *operando* studies of phase transitions, chemical reactions, and structural dynamics under varied environmental conditions (Clegg, 2019).

Moreover, the incorporation of remote-access capabilities across several synchrotron facilities has democratized access to these advanced tools, allowing researchers worldwide to collaborate and perform experiments without the necessity of on-site presence (Clegg, 2019). These combined developments continue to transform the landscape of synchrotron science, delivering deeper insights into the micro- and nano-scale behavior of matter and expanding the possibilities for interdisciplinary research (Winick, 1994).

2.8 Future Prospects and Emerging Trends in Synchrotrons

Looking ahead, the future of synchrotron radiation research appears promising with continuous innovation in both accelerator physics and detector technology (Winick, H., 1994). Trends such as the push towards fourth-generation light sources, including diffraction-limited storage rings and free-electron lasers (FELs), promise even higher brightness and coherence, enabling experiments that were previously considered impossible (Clark, G. L., 1927). Researchers anticipate that these next-generation facilities will offer superior temporal resolution, allowing real-time visualization of ultrafast processes in chemistry, biology, and condensed matter physics (Clark, G. L., 1927).

The integration of artificial intelligence and machine learning into beamline data processing is also expected to revolutionize the analysis of complex diffraction patterns, thereby dramatically speeding up the discovery cycle in many fields (Clegg, W., 2019). In addition, increased efforts in remote access and automation will further democratize access to high-end facilities, making them available to a broader range of researchers across the globe and fostering cross-disciplinary collaborations (Clegg, W., 2019). With these advancements, synchrotron light sources are poised to not only uncover fundamental scientific truths but also to drive practical innovations in energy technology, environmental conservation, and medical diagnostics (Tamal, M., Althobaiti, M., Alomari, A. H., Dipty, S. T., Suha, K. T., & Al-Hashim, M., 2022).

The push towards fourth-generation synchrotron sources, characterized by even higher brightness, improved coherence, and enhanced tunability (Shin, S., 2021), will undoubtedly open new avenues for scientific exploration. Researchers anticipate that these developments will facilitate experiments at temporal and spatial resolutions that were previously considered unattainable, further refining our understanding of dynamic biological, chemical amd physical processes and the microscopic structure of advanced materials (Cao, M., Zhang, K., Zhang, S., Wang, Y., & Chen, C., 2022).

In addition, the integration of machine learning and advanced data analytics into synchrotron research workflows is expected to revolutionize the way data is processed and interpreted, leading to faster and more accurate scientific discoveries (Wang, C., Steiner, U., & Sepe, A., 2018). Continuous innovation in detector technology, beamline optics, and sample handling techniques promises to further reduce experimental noise and enhance signal quality, thereby broadening the applicability of synchrotron radiation to new and emerging fields (Carini, G., Denes, P., Gruener, S., & Lessner, E., 2012). The commitment of the global research community to pushing the frontiers of synchrotron science ensures that this powerful tool will remain at the forefront of scientific inquiry for many years to come.

2.9 Photovoltaics

2.9.1 Energy Overview

The earth's growing population has prompted the need for a reliable source of energy. The depletion of fossil fuels as a source of energy has not enabled them to meet the high energy demand. Moreover, the use of fossil fuels has led to CO_2 emissions, contributing to the pernicious effects of climate change. Solar energy is a renewable and clean type of energy. As a result, photovoltaic converting light into electricity, have emerged to be one of the most promising alternatives to fossil fuel (Weiss M. *et al*., 2016).

Different kinds of photovoltaic materials have been discovered and their photovoltaic performances studied as discussed in section 2.10.2. However, perovskites have recently emerged as promising candidates in the green solar energy quest among other applications.

2.9.2 Photovoltaic materials

Photovoltaic can be categorized as wafer based and thin films. The wafer based solar cells that exist currently are crystalline silicon (C-Si), Gallium Arsenide (GaAs) and III-V multijunction (MJ) solar cells. Photovoltaic (PV) technologies produced using silicon have currently become the most popular solar cells. Silicon has very high carrier mobility, it is non-toxic, very stable (can last up to 25 years) and has an efficiency ranging within 25 % - 30 % (Bharambe C.A *et al*., 2016). However, despite all these, the manufacturing of pure silicon crystals requires very large amount of energy and therefore making it difficult to be produced (Müller, A., Ghosh, M., Sonnenschein, R., & Woditsch, P., 2006).

GaAs (Gallium Arsenide) as a photovoltaic material has also been shown to have unique electronic properties. Electron race through GaAs crystalline structure is quicker compared to silicon (Kilner J.A *et al*., 2012). It has high optical absorption coefficients, a near optimum direct band gap and mobility that is appropriate to solar spectrum (Jean J. *et al*., 2015) (Miles, R. W. (2006). GaAs solar cells have a power conversion efficiency of almost 28.8 % and 24.1 % for laboratory and modules respectively (Kazmerski, L., Gwinner, D., & Hicks, A., 2010) (Green M.A. *et al*., 2014). The disadvantage of GaAs is the high cost of production (Miles, R. W., Hynes, K. M., & Forbes, I., 2005). This limits its large-scale deployment, restricting their use in space applications where higher efficiencies are required.

Similarly, III-V multijunction based photovoltaic Semi-Conductors (SCs) have also shown very good efficiencies. However, multi-junctions (MJs) are very expensive for large scale terrestrial applications. Therefore, their use is confined to demanding environment of space power generation (Philipps, S. P., Dimroth, F., & Bett, A. W, 2018 and Olson, J. M., Friedman, D. J., & Kurtz, S. 2003)

Commercial thin film SCs like CdTe (Cadmium Telluride) and CIGS (Copper Indium Gallium Selenide) absorb light more efficiently compared to silicon based solar cells. Apart from their comparatively low average efficiency, Tellurium and Indium are also rare material elements. In addition, Cadmium is very toxic, and this may limit their potential for large scale production and deployment (Fthenakis, V., & Zweibel, K. (2003).

Organic solar cells (SCs) have also attracted attention due to their low cost of production. Despite using earth's abundant elements and low cost of energy production, they have low PCE limiting their large-scale production (Schmalensee, R., (2015).

Dye Sensitized Solar Cells (DSSCs) have also gained increasing interest. Apart from their low cost of production, DSSCs have attained a Performance Cell Efficiencies (PCE) of up to 12.3 % (Yella A, *et al*., 2011). The major setback of these SCs is long term stability under solar irradiance and high temperature due to the degradation of the electrolyte used.

New group of highly efficient photovoltaic absorber material called perovskite (Docampo P *et al*., 2013). Due to their high-power conversion efficiency (PCE) which recently stands at about 26.7 % (National Renewable Energy Laboratory, 2020), they have the potential to contribute to large scale solar energy production in the future . Perovskite solar cells have attracted more interest as suitable materials for use as a photovoltaic material due to many reasons.

They are obtained from cheap and abundant elements, long charge carrier diffusion lengths and low recombination losses (Xing, G, *et al*., 2013) (Gonzalez-Pedro V., *et al*., 2014). In addition, they have high carrier mobilities (Stoumpos, C. C., Malliakas, C. D., & Kanatzidis, M. G., 2013), high absorption coefficients (De Wolf, *et al*., 2014), and shallow defect levels (Yin, W. J., Shi, T., & Yan, Y., 2014). They are compatible with not only solution processing but also evaporation techniques (Liu, M., Johnston, M. B., & Snaith, H. J., 2013). Unlike other photovoltaic materials, perovskites cells have a tunable band gap and a greater absorbance in the range over the entire visible to near infrared regions (Ibrahim, Shoukat, A., Aslam, F., & Israr Ur Rehman, M., 2024).

2.9.3 Emergence and evolution of perovskites

Perovkite is a calcium titanium oxide mineral, with the chemical formula $CaTiO_3$. The mineral was discovered in the Ural Mountains of Russia by Gustav in 1839 and is named after Russian mineralogist Lev Perovski (1792-1856) (Chen Q. *et al*., 2015). While the true perovskite mineral is composed of calcium, titanium and oxygen in the form $CaTiO_3$, a perovskite structure is anything that has the generic form ABX_3 and the same crystallographic structure as the perovskite structure. The perovskite structure is simply described as a cubic unit with titanium atoms at the corners (seen as red), oxygen atoms at the mid-points of the edges (seen as gray) and calcium atom (yellow) in the center as seen in Figure 2.9.

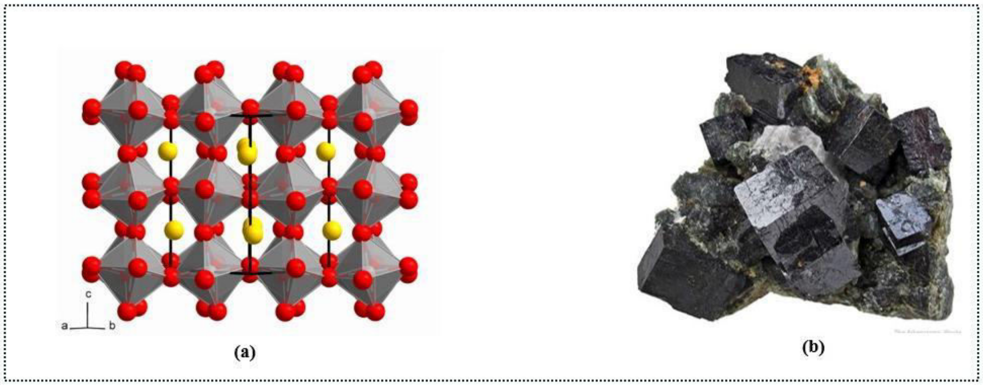

Figure 2.9: (a) Perovskite structure of the basic building block of perovksites of $CaTiO_3$ (b) the perovskite-ore discovered by Gustav Rose (Perovskite-Info., 2025).

Three dimensions (ABX_3 structure) perovskites have predominantly been the talk in perovskites engineering with their ease in fabrication, band gap tuning and high efficiencies (Jin Y. K., *et al.,* 2020). This made them a fascinating topic for many researchers who are interested in surpassing the silicon modules Shockey-Queisser maximum efficiency of 32% (Shockley W. and Queisser H.J., 1961).

In the basic building block of perovskite the ABX_3 structure, A can be organic cation such methylammonium (MA) $CH_3NH_3^+$; formamidine (FA) $CH\ (NH_2)_2^+$) and an inorganic cation such as cesium (Cs). B is (Pb^{2+}; Sn^{2+}; Ge^{2+}) and X is (Cl^-; Br^-; I^-, BF_4^-; PF_6^-; SCN^{-1}) (Hendon *et al*, 2015 and Awino, C. *et al*, 2020). The simple structure consists of a 3-dimensional network of corner-sharing BX_6 octahedra as shown in Figure 2.10.

The first perovskite structure is Methylammonium lead iodide perovskite ($CH_3NH_3PbI_3$) which takes cubic structure at high temperature and tetragonal structure at room temperature with transition temperature of 331 K (Kawamura, Y., Mashiyama, H., & Hasebe, K., 2002). The tetragonal crystal system becomes orthorhombic below 162.2 K

(Frost, J. M., 2014).

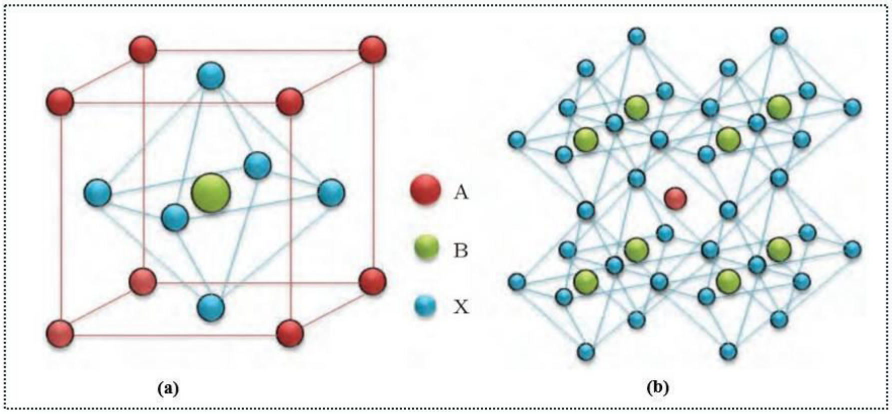

Figure 2.10: Crystal structure of perovskite. (a) cubic structure of perovskite (b) tetragonal structure of perovskite (Kawamura, Y., Mashiyama, H., & Hasebe, K., 2002)

Methylammonium cation in $CH_3NH_3PbI_3$ demonstrated increasing positional disorder as temperature increases from 100 K to 352 K and only stable in the tetragonal phase at temperatures between 165K and 327K (Kawamura, Y., Mashiyama, H., & Hasebe, K., 2002). This high level of orientational motion of methylammonium cation at room temperature gives excellent photovoltaic performance of perovskite and also anomalous hysteresis as reported by Snaith and co-workers (Snaith H.J. *et al.*, 2014). The inorganic part is usually a divalent metal cation for charge balancing while the organic part consists of organic cation which form three -dimensional perovskite structure.

Methylammonium lead iodide, $CH_3NH_3PbI_3$, with a band gap 1.5-1.6 eV (Dittrich T. *et al.*,2015) and is the first absorber for these related solar cells, with high advantages due tunability of its optical properties. The bandgap of this absorber can be tuned by adjusting their inorganic and organic compounds. Being a direct band gap semiconductor, has a high absorption coefficient, long diffusion length, high charge carrier mobility and can function as ambipolar charge transport material for electrons and holes to corresponding collector electrodes (Awino, C. *et al*, 2020). These unique properties rendered it useful as absorber materials for photovoltaic applications.

Due to changes in the ABX_3 structure, perovskites were then classified as pure inorganic oxide perovskite (no MA and FA), non-halide or halide perovskites. Inorganic oxide perovskites are further categorized into intrinsic and doped perovskites (Aïssa, B., Ali, A., & El-Mellouhi, F., 2021). On the other hand, halide perovskites can be grouped into either alkali-halide perovskites or organo-metal halide perovskites. For organic-inorganic perovskites, *A* is the larger mono-valent organic cation (methyl ammonium or formamidinium) or inorganic cesium (Cs) or Rubidium (Rb), B usually Pb^{2+} or Sn^{2+} and X is the halogen (Br, Cl, I) (Fan, Z., Sun, K., & Wang, J., 2015).

Halide perovskites have remarkable structural and composition tunability, with the basic block ($[BX_6]^4$ – metal halide octahedral) being able to be arranged in different ways (Enzheng S., *et al.,* 2018). This makes them to undergo metamorphosis into three dimension (3D), two-dimension (2D) and one dimension (1D) crystal structures (a times 0D) (Li, X., *et al.*, 2024). The highly studied crystal structures of the perovskite are the 3D or 2D formations.

2.9.4 Three dimensional (3D) perovskites

The 3D perovskite are usually used for solar cells applications. The common architectures are $CH_3NH_3PbI_3$ (Which was the first design of the solar perovskite, commonly referred to as MAPI), $CH_3NH_3PbBr_3$ and mixed halide $CH_3NH_3PbI_{3-x}Cl_x$ or $CH_3NH_3PbI_{3-x}Br_x$. The methylammonium in these perovskites is usually abbreviated as MA.

The architecture of these materials can be changed by introducing Formammidum ($FA=CH(NH_2)_2$), Cesium (Cs) or a combination of two or the three cations at the A site, in addition to the variations at the halide site. For instance, when MA is substituted by FA it forms $FAPbI_3$ commonly referred to as FAPI (RaeisianAsl, M., Panahi, S. F. K., Jamaati, M., & Tafreshi, S. S., 2022). If MA and FA are used at A, $MAFAPbI_3$ is formed which is commonly called MAFA (or 2-CAT or double cation) (Zhang, T., Xu, Q., Xu, F., Fu, Y., Wang, Y., Yan, Y., ... & Zhao, Y., 2019) and using Cs, MA and FA, the architecture changes to $CsMAFAPbI_3$ referred to as Cs-MAFA (or 3-CAT and triple cation) (Zhao, J., Liu, X., & Wu, Z., 2023). The variation of A site is in attempt to attain stability, while halide variations change the band gap of the perovskite (usually seen as coloured perovskites with applications in Light Emitting Diodes-LEDs)

2.9.5 Two dimensional (2D) perovskites

2D halide perovskites can be thought of as 'slabs' cut from the 3D parent structures called the Ruddlesden–Popper (RP) phase (Aidan H. C. *et al*., 2023). The general formula of the RP phase takes the structure $L_2A_{n-1}B_n X_{3n+1}$ (L being a large monovalent cation called the ligand such as Butylammonium (BA), Phenyethylammonium (PEA) or 1T,2T,3T… and A being Methylammonium (MA) or Cesium (Cs) while $n = 1,2,3…$), B is a divalent metal cation such as Pb^{2+} or Sn^{2+}, and X is a halide. The variable n is an integer, which indicates the number of metal halide octahedral layers between the two L cation layers.

When the thickness of the 3D ABX_3 perovskites is reduced then 2D perovskites are produced (Sun, S., Yuan, D., Xu, Y., Wang, A., & Deng, Z., 2016). These perovskites are usually called the Dion-Jacobson (DJ) perovskites and are characterized by the chemical formula, $DA_{n-1}M_nX_{3n+1}$, where D is a divalent large organic spacer cation (such as propane-1,3-diammonium (PDA) and 1,4-butanediamonium (BDA), as well as dianthradipyridine (DAN) and di-1-naphthylamine) while ABX are similar as in RP. A very thin 3D sheet changes the chemical formula and is no longer ABX_3 but with a finite ‘‘*n*’’ value. Such structural flexibility and tunability of 2D halide perovskites provide a noble platform for the preparation of interesting nanostructures with excellent electronic properties for a variety of electronics and optoelectronic applications.

2.9.6 Fabrication

Perovskite solar cells are fabricated using various methods. In vapor deposition methods, the substrate is exposed to one or volatile precursors, which react with the substrate and decompose to form the wanted deposit. Vapor deposited hybrid perovskite films are more homogeneous and provide a higher surface coverage than solution processed films (Liu, M., Johnston, M. B., & Snaith, H. J., 2013).

Thermal evaporation requires the creation of a vacuum environment, where enough heat is given to the evaporates to attain vapor pressure required for evaporation. The evaporated materials are allowed to condense on the substrate kept at a suitable temperature (Petrović, M., Chellappan, V., & Ramakrishna, S., 2015) (Abbas H.A. *et al*., 2015). It has been reported that using dual co-evaporation, MAI and $PbCl_2$ obtained highly uniform films with almost 100% surface coverage, high PCE of around 15.4 % and pin-hole free layers were achieved. However, the use of this method requires high amount of energy for film fabrication (Liu, M., Johnston, M. B., & Snaith, H. J., 2013).

Spray coating is a scalable deposition technique ideal for large-area fabrication of perovskite films (Alanazi, T. I., 2023). In this method, a fine mist of perovskite precursor solution is atomized and sprayed onto a substrate, forming a uniform thin film after solvent evaporation and thermal annealing. The process is compatible with roll-to-roll manufacturing and enables flexible control over film thickness and morphology (Roth, B., Søndergaard, R. R., & Krebs, F. C., 2015). Spray coating is particularly attractive for its ability to conform to non-flat surfaces and its high-throughput potential. However, controlling droplet size, uniformity, and solvent evaporation rates are critical to achieving high-quality perovskite layers with consistent optoelectronic properties (Zhao, X., Gao, W., Dong, H., Zhou, Y., Huang, H., Wu, Z., & Ran, C., 2024).

Slot-die coating is one of the most promising techniques for industrial-scale production of perovskite solar cells due to its high material utilization efficiency and precision in film thickness control. In this method, the perovskite precursor is dispensed through a narrow slot onto a moving substrate, enabling continuous and uniform film deposition (Shin Thant, K. K., *et al*., 2025). This technique is inherently compatible with roll-to-roll processing, making it well-suited for large-area, high-throughput manufacturing (Roth, B., Søndergaard, R. R., & Krebs, F. C., 2015). Compared to spin coating, slot-die coating minimizes waste and is more environmentally and economically viable for commercial deployment. Challenges include managing solvent drying dynamics and crystallization to ensure uniform film formation (Duarte, V. C., & Andrade, L., 2024 and Shin Thant, K. K., *et al*., 2025).

Inkjet printing offers a digital, additive approach to fabricating perovskite layers, where droplets of precursor solution are deposited in a highly controlled, patternable manner

(Mathies, F., List-Kratochvil, E. J., & Unger, E. L., 2020). This technique enables mask-free fabrication and precise material placement, making it especially suitable for complex device architectures or multi-junction cells. Inkjet printing reduces material waste and allows for customization in production, such as printing on demand or adjusting composition gradients (Cohen, T. A., 2022). Nonetheless, achieving uniform film coverage, controlling droplet coalescence, and ensuring consistent crystallization remain areas of active research to optimize performance and yield using this method (Cohen, T. A., 2022).

Spin coating offers advantages like *ease of use*, *low cost*, and *the ability to control film thickness* and *morphology*, *making it a standard method for perovskite fabrication in labs* (G2V Optics., 2025). Spin coating methods include: one step, two step/sequential deposition Li C. *et al*., 2008) (Burlakov C.A. *et al*., 2014). In spin coating the metal halide and organic halide are dissolved in organic solvents, followed by deposition on a substrate and formation of the perovskite through annealing around 100^0C. However, it is not suitable for large-scale production due to material waste and potential exposure to harmful chemicals (G2V Optics., 2025)

2.9.7 Crystallization and phase changes in perovskites

Hybrid lead perovskite precursor is a low-viscosity solution that can form colloidal aggregates in solution and take complicated nucleation and growth pathways during drying process (Yan, K. *et al*., 2015). However, during fabrication, the solvents are usually removed, thus the solvent removal rate together with diffusion of the constituents and crystallization process play a critical role in perovskite films morphology. Factors such as precursor solvents (Jeon, N. J. *et al*, 2014), sources of lead (Zhang, W. *et al.*,

2014) and additives affect both crystallization and the microstructure formation in the process of perovskite film growth.

Hybrid halide perovskites evolve progressively from the precursor solution phase to the final cubic (black color) α-phase through the intermediate non-perovskite hexagonal (orange, brown, and yellow colors) δ-phase as seen in Figure 2.11 (Xiang, W. *et al*., 2022) taken for all the three cations. However, the cubic α-phase is very unstable in ambient conditions which tends to regress into the photo-inactive hexagonal 2*H*,4*H*,6*H* and 8*H* δ-phase and some lead iodide also appearing. Hexagonal phase has a wider band gap, larger defect density and poor quantum efficiency and is therefore unsuitable for photovoltaic applications (Ma F. *et al*., 2017 and Han O. *et al*., 2016).

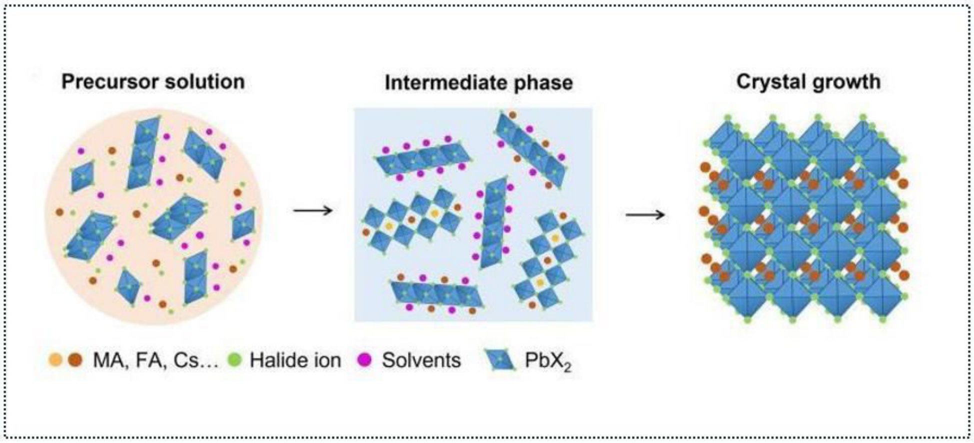

Figure 2.11: The perovskite phase transition of the perovskite from the precursor solution through the intermediate phase to the final phase (Xiang, W. et al., 2022)

The Goldschmidt tolerance factor, *t*, is an important index for engineering stable halide perovskite solar cells. It is usually used to construct a structure map to study the formation of cubic perovskites. The tolerance factor is calculated using the iconic radii of the A, B, and X ions in the ABX_3 perovskite as given in equation 2.3.

$$t = \frac{\mathrm{r_A}+\mathrm{r_X}}{\sqrt{2(\mathrm{r_B}+\mathrm{r_X})}} \qquad 2.3$$

where r_A, r_B, and r_X are ionic radii of A, B, and X ions in ABX_3 perovskite, respectively. The tolerance factor (*t*) for a cubic perovskite structure is typically between 0.8 and 1.0 (Bakar A. *et al*., 2022; Sun, Q., & Yin, W. J., 2017 and Li, Z. *et al*., 2016). When *t* is close to unity ($t = 1$), it gives the ideal cubic perovskite structure which is stable at ambient conditions (Bakar, A. *et al*., 2022). When $t < 0.8$ or $t > 1.0$, usually results in non-perovskite structures or simply distorted perovskite structures, typically hexagonal, orthorhombic, or phases other than perovskite. (Li, Z. *et al*., 2016 and Yamada, I., Takamatsu, A., & Ikeno, H., 2018).

To explain these phases, synchrotron techniques have widely been employed through GIWAXS/GISAXS which provides experimental validation of the structural predictions made by the Goldschmidt tolerance factor (Li, Z., *et al*., 2016). While the tolerance factor predicts likely structural forms based on ionic radii, GIWAXS/GISAXS confirms the actual structure, detect distortions, and monitor phase stability (Kennard, R. M.,*et al.*, 2021). All these help refine or challenge the assumptions behind using the tolerance factor for a given perovskite.

Studies of perovskites using X-ray imaging, spectroscopy, and scattering microscopies have been used in the understanding of the internal workings of perovskites (Kodur, M., *et. al*., 2020). Halide perovskites have remarkable structural and composition tunability, with the basic block ($[BX_6]_4$ – metal halide octahedral) being able to be arranged in different ways (Enzheng S., *et al.,* 2018).

Many studies have been conducted both *ex situ* and *in situ* observations made on the crystallization kinetics of the perovskite materials (Schlipf, J., 2015). Literature has reported the chemical pathways from the plumbate intermediates (Barrows, A. T. *et al*., 2016 and Guo, Y. *et al*. 2015) or metastable phase (Aguiar, J. A. *et al*., 2016 and Wang B. *et al*., 2015) to perovskite crystal identified using *in situ* X-ray diffraction.

However, time evolution of crystallization and phase transition *in situ* cases usually begins with the prepared solvent to intermediated complex film and finally to the perovskite crystal (Sánchez, S., Pfeifer, L., Vlachopoulos, N., & Hagfeldt, A., 2021). This approach is vital in understanding the crystallization growth of the perovskite starting from the solution phase into the solid phase to enable deep understanding of the full transformation process to pure perovskite. Some reports discuss perovskite crystallization from drop-casting solution to dry films in which full transformation process to pure perovskite was not achieved with existence of by-products in the final dried film (Soultati, A., Tountas, M., Armadorou, K. K., bin Mohd Yusoff, A. R., Vasilopoulou, M., & Nazeeruddin, M. K., 2023).

Quin H. *et al.* presented a comprehensive investigation of perovskites crystallization dynamics and morphology evolution from the very original precursor solution of $CH_3NH_3PbI_3$ pristine to solid phase crystals *in situ* and in real time (Quin H. *et al*., 2017). They used *in situ* grazing incidence X-ray diffraction (GIXD) with *in situ* Fourier transform infrared spectroscopy (FTIR) to reveal the crystalline formation and chemical composition reactions of perovskite materials over relevant time and temperature scales. In their work, they applied on-line characterization techniques to systematically investigate the crystallization kinetics and growth mechanism from the precursor solution to the films. They found out that a perovskite crystal intermediate, comprised of an octahedral $[PbI_6]^{+4}$ centre surrounded by cooperative ions. The ion cage species had close packing which led to the formation of perovskite crystallites, which then deposited onto the supported substrate to form photo-active thin film.

Furthermore, it was observed that (Quin H. *et al*., 2017) elevated-temperature annealing led to a periodic crystallization growth habit, forming concentric ring patterns and increasing the rate of solvent evaporation by involving the HAQ process, the morphology was kinetically trapped, leading to smooth films state that were better placed for thin-film opto-electronic devices.

Aidan *et al*., (Aidan H. C. *et al*., 2023) introduced a 2T ligand (bio-thiophene 2T ligand) to develop quasi-2D perovskite with n = 7 which had had not been reported elsewhere. From their findings, adding initially a poorly coordinating solvent (gamma-butyrolactone) and subsequent addition of dimethylsulfoxide and methanol the vertical orientation and Z-uniformity is improved as observed by the GIWAXS and advanced optical characterization.

A custom-made *in situ* multi-modal spin coater system (MMSC) with an integrated heating stage coupled with synchrotron-based GIWAXS/GISAXS was designed by Aidan and co-workers (Chenhui Z., *et al*., 2023). This system has an adoptable experimental chamber with ability to accommodate several auxiliary probes (Photoluminescence, visible optical cameras – IR/Vis imaging) which gives true Multi-Modal characterization with correlated data analysis. The structural evolutions such as perovskite crystallization can be monitored with millisecond temporal resolution throughout the film fabrication process.

The perovskite Cuboid crystallization correlates highly with surface morphology changes under various growth conditions for static samples. *Ex situ* studies do not sufficiently provide information on the perovskite growth mechanism; however, *in situ* reports vividly demonstrate chemical pathways from plumbate (Barrows, A. T. *et al.*, 2016; and Guo, Y. *et al.*, 2015) intermediates of meta-stable (Aguiar, J. A. *et al.,* 2016 and Wang, B. *et al.*, 2015) phases to some perovskite crystals.

However, the time evolution of crystallization and phase transition in *in situ* cases usually begins from prepared precursor solution to the solvent-intermediated phase then to the solid phase. Drop-casting solution to dry film procedures done before (Chang, C. Y., Huang, Y. C., Tsao, C. S., & Su, W. F., 2016) did not achieve full transformation to pure perovskite. Formation of periodic patterns during the growth process is usually attributed to a competition between the linear growth of crystals and a depletion of crystallizable materials.

2.9.8 Stability in air (Moisture and Oxygen)

Water (H_2O) and oxygen (O_2) play a significant role in compromising the chemical stability of perovskite solar cells (PSCs), leading to the degradation of the perovskite material, typically indicated by a color change from dark brown to yellow. Wang *et al.* investigated the hydrolysis of $MAPbI_3$ under humid conditions explaining various chemical changes (Wang Q. & Abate A., 2018).

To enhance PSC stability, a hydrophobic buffer layer is introduced on top of the perovskite layer which has proven effective (Zeng X. *et al.*, 2018; Wang Q. & Abate A., 2018). Another approach involves incorporating more stable and water-resistant compositions, such as MAPI $(I_{1-x}Br_x)_3$(Noh J.H. *et al*., 2013). Snaith *et al.* observed that moisture exposure during fabrication can partially solvate the methylammonium component and facilitate a reorganization of the perovskite lattice. This structural rearrangement reduces trap density and enhances both open-circuit voltage (V_{oc}) and photoluminescence (Eperon G.E. *et al*., 2015). Aristidou *et al*. reported that oxygen-induced degradation leads to a substantial decline in the yield of photo-generated charge carriers (Aristidou, N. *et al.*, 2015).

The mixed-cation, mixed-halide perovskite $Cs_{0.05}(FA_{0.83}MA_{0.17})_{1-x}Pb(I_{0.83}Br_{0.17})_3$ exhibits improved structural and thermal stability due to the incorporation of Cs^+ and a FA-rich matrix. Br^- substitution enhances moisture resistance but introduces a risk of halide phase segregation. Li explains the hydrolysis of ethyl that modifies the surface of perovskite films with a general mechanism of the water induced degradation of perovskites (Li, Q., 2024).

In ambient air, the material remains vulnerable to moisture- and oxygen-induced degradation, primarily through hydrolysis (Perovskite plus water goes to a sum of FAI MAI, PbI_2 and others) and phase segregation mechanisms $(I/Br^- \xrightarrow{moisture + air} I - rich\, and\, Br - rich$ domains). Performance losses are accelerated under humidity cycling and light exposure. Stability can be significantly improved through encapsulation, surface passivation, and the use of hydrophobic or additive-based protection strategies explained by Hu *et al.* (Hu, L., Liu, K. Q., Li, F., Li, H. Y., Wang, W., Fang, H. L., ... & Wang, Z. X., 2024).

The hybrid perovskite $Cs_{0.1}FA_{0.9}PbI_3$ demonstrates improved phase and thermal stability compared to pure $FAPbI_3$, primarily due to the incorporation of 10% cesium, which helps stabilize the black photoactive α-phase and suppress the formation of the yellow δ-phase at room temperature. However, the material remains vulnerable to degradation when exposed to moisture and oxygen in ambient air. Moisture can trigger hydrolysis, leading to the breakdown of the perovskite into PbI_2 and decomposition of the organic formamidinium cation.

In parallel, oxygen, especially under illumination, facilitates photo-oxidative degradation via the generation of reactive oxygen species such as superoxide (O_2^-), which attack the organic components and accelerate structural decomposition. These effects are amplified under humidity cycling, which promotes ion migration, lattice strain, and irreversible phase transitions. To mitigate these degradation pathways, phenylethylammonium chloride (PEACl) passivation has emerged as an effective strategy. PEACl forms a quasi-2D layer at the perovskite surface or grain boundaries, passivating defects, reducing ion migration, and acting as a hydrophobic barrier against moisture.

This passivation improves both environmental stability and optoelectronic performance by suppressing non-radiative recombination and enhancing resistance to moisture and oxygen ingress. When combined with encapsulation or additional barrier layers, PEACl-treated $Cs_{0.1}FA_{0.9}PbI_3$ demonstrates significantly enhanced durability under real-world operating conditions as expained by Hu, R. *et al.* (Hu, R., Zhang, Y., Paek, S., Gao, X. X., Li, X. A., & Nazeeruddin, M. K., 2020).

2.9.9 Structural, optical and electronic properties

Both experimental studies and first-principles calculations have been conducted to investigate the structural, optical, and electronic band structure of hybrid halide perovskites.

Electronic structure analyses indicate that the electronic properties are primarily governed by the interaction of Pb 6*p* and halide *p* orbitals. Calculated exciton binding energies (E_x) using the hydrogenic model show that increasing chlorine content leads to a rise in E_x. This trend is mainly attributed to a reduction in the dielectric constant of the material, while the reduced effective mass remains nearly constant at approximately $0.07m_e$ (Buin A. *et al.*, 2015).

The mixed-cation, mixed-hybrid halide perovskite $Cs_{0.05}(FA_{0.83}MA_{0.17})_{1-x}Pb(I_{0.83}Br_{0.17})_3$ exhibits improved phase stability and film uniformity due to the combined effects of cesium and bromide incorporation, which help suppress δ-phase formation and reduce defect density. Its optical bandgap is slightly widened (~1.62–1.68 eV), offering tunable absorption and moderate photoluminescence efficiency. In contrast, $Cs_{0.1}FA_{0.9}PbI_3$, when passivated with phenylethylammonium chloride (PEACl), shows enhanced structural integrity with larger grains and significantly reduced surface defects.

This passivation improves photoluminescence intensity, extends carrier lifetimes, and lowers trap-state density without markedly altering the bandgap (~1.55–1.60 eV). The electronic performance is further enhanced by increased carrier mobility and reduced non-radiative recombination, making PEACl-treated $Cs_{0.1}FA_{0.9}PbI_3$ a more stable and efficient material under ambient conditions compared to its mixed-halide counterpart.

CHAPTER THREE
METHODOLOGY

3.1 Materials and equipment

3.1.1 Salts

Methyl Ammonium iodide (MAI) 99.9 % TCI, Methylammonium Bromide (MABr) 99.9 % TCI Formammidium Iodiode (FAI) 99.9 % TCI, Lead Iodide 99.9 % Sigma Aldrich, Cesium Iodide 99.9 % Sigma Aldrich, phenylethylammonium chloride (PEACl) 99.9 % Sigma Aldrich and 2,8-Bis(diphenyl-phosphoryl)-dibenzo[b,d]furan (PPF) 96.9 % TCI.

3.1.2 Solutions

Dimethylformamide (DMF) and dimethyl sulfoxide (DMSO), Chlorobenzene (CB)/ethyl-acetate (EA) at 15 mg/ml solution (anti-solvents), Distilled water, Detergent made of 2 % mucasol, acetone Lab grade 99.5% and Isopropanol Thermo fisher scientific 99.5%.

3.1.3 Other materials and experiment equipment

Indium doped tin oxide (ITO) glass substrate (Lumtec, size 1x1 cm^2, resistivity of about 50 Ω /sq). Glovebox filled with nitrogen, two-step spin-coater, programmed hot-plate, weighing balance, electric shaker/mixer, UV-Ozone Cleaner/inert plasma cleaner, sonicating machine, beakers, pipette tips, multi-meter and Sample packing tins/cans.

3.1.4 Characterization Equipment

Synchrotron techniques; Grazing Incident Wide Angle X-ray Scattering (GIWAXS) beamline, Micro Diffraction Beamline. PL measuring instrument, Scanning Electron Microscope (SEM), Atomic Force Microscopy (AFM), and UV-Vis spectroscopy.

3.2 Experimental procedures

Perovskite films were prepared in nitrogen filled glove box for *static* measurements and on hot stage in the *in situ* measurements at the Molecular Foundry, Lawrence Berkeley National Laboratory, CA, USA.

3.2.1 Preparation of the ITO glass substrates

The ITO glass substrates were tested using the multi-meter to determine the conducting side by measuring the resistance of the substrate. Then they were subsequently cleaned in the detergent, then rinsed with deionized water, followed by cleaning in acetone, then DI water and finally in iso-propanol for 15 minutes at every stage. After which, the substrates were dried with nitrogen and thereafter treated with ozone (generated by ultra -violet (UV- light shown in Appendix 1) for 20 minutes to activate the surface (Kegelmann L. *et al.*, 2017)

3.2.2 Three Dimension (3D) perovskites)- $Cs_x(FA_{0.83}MA_{0.17})_{1-x}Pb(I_{0.83}Br_{0.17})_3$

$MAPbI_3$, $FAPbI_3$, $MAPbBr_3$ **p**erovskites was prepared by reaction of organic halide precursor solution with an in-organic halide precursor salt. For $MAPbI_3$ one mole of CH_3NH_3I (159 mg) and one mole of PbI_2 (461 mg) was dissolved in 700 µl of dimethylformamide (DMF) and 71 µl dimethyl sulfoxide (DMSO) (Kegelmann L. *et al.*, 2017). $FAPbI_3$ was prepared by mixing 1M of FAI (171.97 mg) and 1.09M of PbI_2

(502.5 mg), which $MAPbBr_3$ was prepared by mixing 0.2M MABr (22.394 mg) and 0.2M $PbBr_2$ (289.95 mg). Each of these was dissolved in 800 μl DMF and 200 μl DMSO. 259.81 mg of CsI was dissolved in 1000 μl of DMSO. The solutions were mixed using the electric shakers overnight at room temperature in a nitrogen filled glovebox.

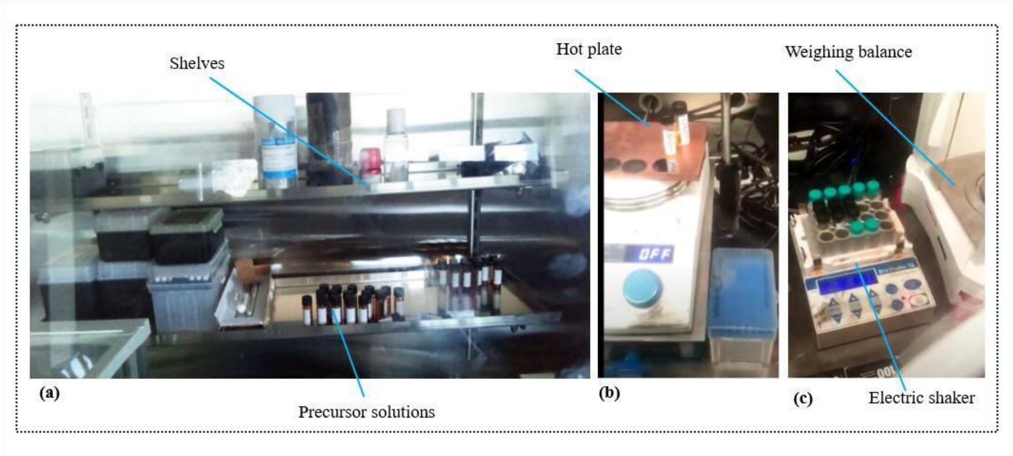

Figure 3.1: Inside the glovebox with (a) vials and precursor solutions (b) Hot plate, Electric shaker and (c) the hot-plate.

The inside of the glove box fitted with shakers, hot plate and weighing balance is shown in Figure 3.1 (a) to (d). To prepare $Cs_x(FA_{0.83}MA_{0.17})_{1-x}Pb(I_{0.83}Br_{0.17})_3$, we first took 400 μl of the precursor solution of $FAPbI_3$ and 80 µl of $MAPbBr_3$ solution then mixed to give percentages of 83% to 17% respectively to make the precursor solution of $FA_{0.83}MA_{0.17}Pb(I_{0.83}Br_{0.17})_3$. The solution of CsI was added to the solution of $FA_{0.83}MA_{0.17}Pb(I_{0.83}Br_{0.17})_3$ in varying ratios, for x = 0 (0 μl of CsI), 0.05(25.26 μl of CsI), 0.10(50.52 μl of CsI), 0.15(75.78 μl of CsI) (Saliba M. *et al., 2016*, and Meng L. *et al.,* 2020).

The films were prepared by spin coating in two steps of 1000rpm for 10s at an acceleration of $1m/s^2$ and 3000 rpm for 20s at an acceleration of $3m/s^2$ onto the substrate.

chlorobenzene and Ethyl acetate anti-solvent was dropped 5 seconds to the end of the spin coating to hep in solvent evaporation. Finally, the films were annealed at 100 ^{0}C for 10 minutes on the hot plate. Figure 3.2 shows the procedural steps of spin-coating.

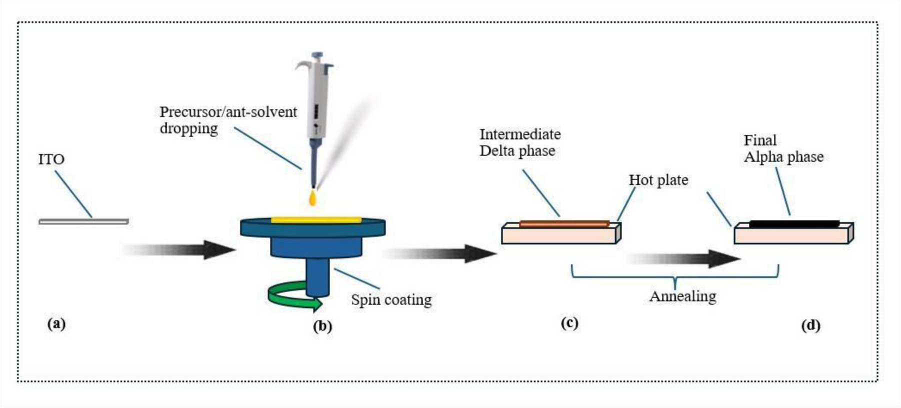

Figure 3.2: Schematic diagram showing the procedural steps of the spin coating process.

The transparent ITO substrate was placed on the spin-coater on which the precursor solution was dropped as shown in Figure 3.2 (b)**.** On dropping the anti-solvent, the film automatically changed colour to dark brown as seen in Figure 3.2 (c), implying some phase formation and on annealing the cubic dark phase appears as seen in Figure 3.2 (d).

3.2.3 Three Dimension (3D) perovskites- $Cs_{0.1}FA_{0.9}PbI_3$

The solution of $Cs_{0.1}FA_{0.9}PbI_3$ perovskite were prepared by reaction of an inorganic precursor salts of cesium iodide (CsI), and lead iodide (PbI_2) with an organic halide precursor solution of formammidium iodide (FAI).

Precursor solutions were prepared by following the compositions outlined by Pan, Yining, *et al* (Pan, Yining, *et al.*, 2024). For the control precursors in which 0.023 g of 99.9 % Sigma Aldrich CsI, 0.294 g of 99.9% TCI FAI and 0.830 g 99.9% PbI_2 99.9 % Sigma Aldrich were dissolved in 200 μl of DMSO and 800 μl of DMF in 1:4 v/v ratio.

Target solutions were made by introducing varied concentrations of PEACl in three vials containing 0.03 wt%, 0.75 wt% and 1.5 wt% each with similar salts/solvent compositions with the control precursor. The PPF was added to the antisolvent in concentrations of 0.00 g/mol, 0.01 g/mol and 0.02 g/mol. The the solutions of the precursor and the PPF-antisolvents mixtures were mixed by electric mixers in the nitrogen filled glove box overnight at room temperature.

3.3 DATA acquisition Methods

3.3.1 Synchrotron-based *ex situ* GIWAXS experiment in helium

Ex situ GIWAXS measurements were conducted at beamline 7.3.3 at the Lawrence Berkeley National Laboratory shown in Figure 3.3. The experiments in the hatch were controlled by the Labview inter-phase. The wavelength of X-ray was 1.23984 Å (at 10 keV) and the scattering signals was collected by the Dectris pilatus 2M for 7.3.3. The sample to detector distance ranged: 270–280 mm and was optimized depending on the q-range (scattering vector) and detector size. The incident angle was kept at between 1.5° to 2° to enhance the signal resolution with a frame exposure time of between 10 s to 60 s. The spot size ranged from 0.02 mm to 0.03 mm depending on the alpha angle.

For static measurements, the samples were placed on the scanning stage bar and tests made subsequently. The shutter was opened to set the stage active then the beam stop was tested. Next alpha X-Y positioning was set, however the Y-stage was set to range between 8 to 10 cm while the X-stage was varied depending on the position of the scanning stage bar. The scan was then started to determine the positioning of the sample, thereafter the sample was adjusted and positioned at the center since the penetration depth was not linear, by moving the motor. The process of scanning was repeated for several other positions of the sample. Figure 3.5 shows the sample being scanned on the GIWAXS stage as viewed by the cameras using the LabVIEW software.

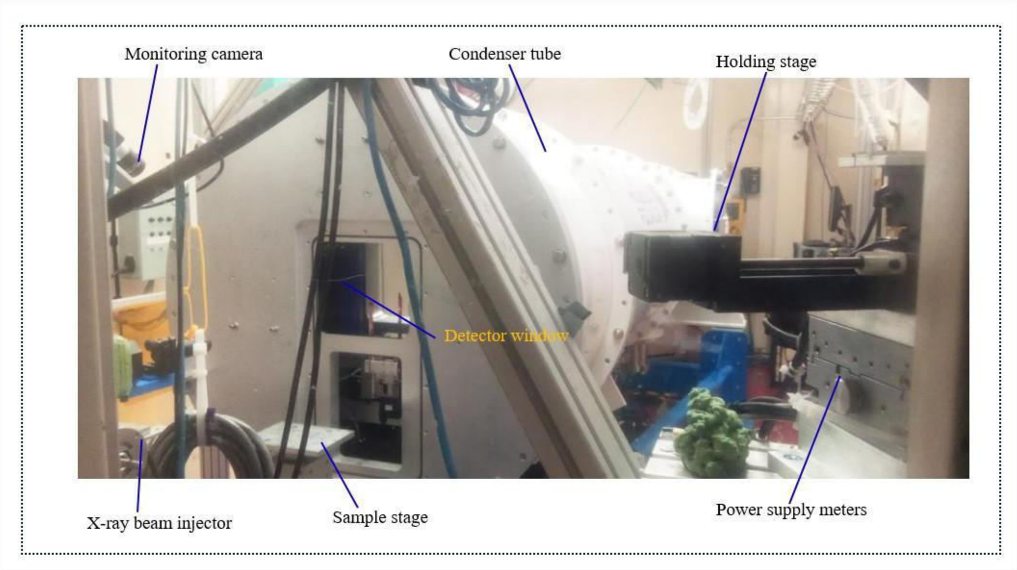

Figure 3.3: The beamline 7.3.3 at Advanced Light Source. The GIWAXS/GISAXS components shown to include the sample stage, x-ray beam injector, condenser tube, monitoring camera, holding stage and the power supply.

The 2D GIWAXS detector images were calibrated with silver behenate (AgB) for standard sample refinement and calibration to convert the patterns into the q-space. The mask was created, which blocked unnecessary intensities. Typical azimuthal averaging or line cuts to form a 1D intensity versus *q* which allowed for more qualitative analysis of peak evolution during crystallization (Coffey, A. H., Yang, S. J., Gómez, M., Finkenauer, B. P., Terlier, T., Zhu, C., & Dou, L., 2023; Coffey, A. H., Slack, J., Cornell, E., Yang, L. L., Anderson, K., Wang, K., ... & Zhu, C., 2023;). We employed the Igor Pro software installed with NIKA in the data analysis.

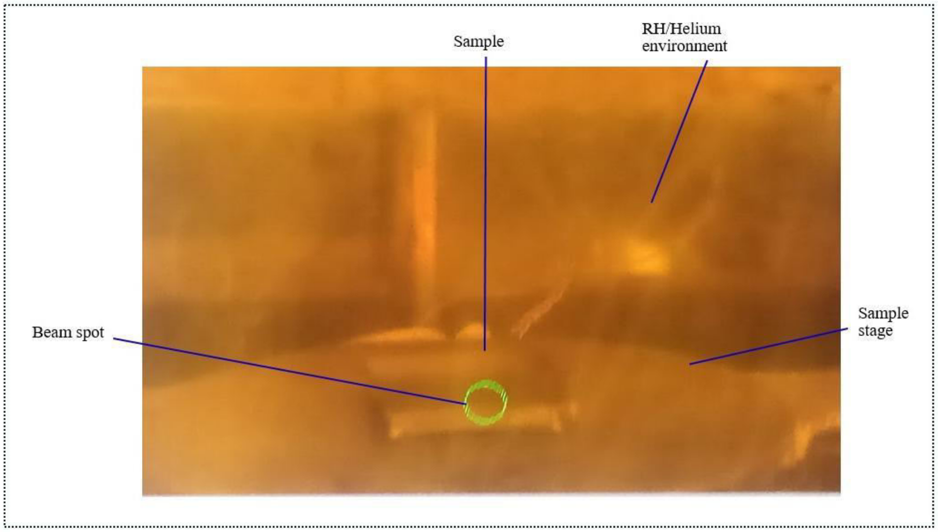

Figure 3.4: A lab-view window as observed from the camera showing the sample undergoing static testing in a helium environment and RH subjected.

3.3.2 Synchrotron-coupled relative humidity (RH)

The humidity sensor was tested by parameter ramping with Relative Humidity values ranging from 10 % RH to 120% RH in a non-equilibrium condition. This RH tester was controlled by the LabVIEW inter-phase at beamline 7.3.3. Figure 3.5 (a) shows the RH apparatus being tested before connection while Figure 3.5 (b) shows when the RH are connected and measurements being taken.

The humidifier was used to moisturize the chamber mounted on the GIWAXS stage. The custom made partially transparent chamber had auxiliary provisions to which the humidity probe and the communication sensor was connected. The humidifier was fitted with a reader interface monitor that could take humidity measurements. It had a water section connected to a hose-tube that had a probe to the chamber. In-twin with the hose-tube, there was a communication sensor cable also connected to the helium chamber on the GIWAXS stage that constantly monitored the humidity environment in the chamber (on the film) as explained by others (Huang, H., *et al*., 2021 and Sun, K., 2023).

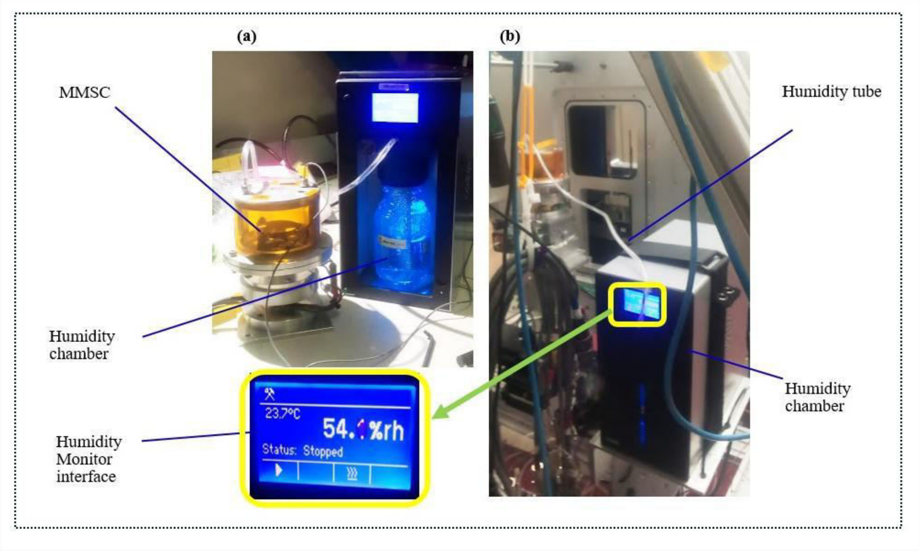

Figure 3.5. (a) Shows the Relative Humidity apparatus being tested on the MMSC before mounting in the hutch. (b) Shows the RH apparatus connected on to the MMSC, mounted on the GIWAXS stage.

The system was controlled by the lab-view interface, whereby the relative humidity levels were reduced by purging the moisture in the chamber using helium; helium gas was used to limit the oxygen content in the chamber which could have had an overall degradation effect on the films. The measurements were taken at room temperature 25 ^{0}C ± 0.5 ^{0}C. The values of RH on the helium chamber were ramped from 0 % RH to 110 % RH. It took on average 20 minutes for the non-equilibrium conditions to be realized. It should be noted, beyond the 100% RH mark, the non-equilibrium conditions set-in and the air became supersaturated; with the absence of condensation nuclei in the chamber the environment fairly remained vaporized.

3.3.3 Synchrotron-based *ex situ* X-ray micro-diffraction experiment in air

The synchrotron-based X-ray micro-diffraction experiment was conducted at Beamline 12.3.2, as shown in Figure 3.6. The beamline had a superbend source, with an energy range of 6 keV to 22 keV, and a wavelength range of 0.56 Å - 2.1 Å with a high revolving power of 6000 radians. The beam size was approximately 1 micrometer at the sample position which was set by a pair of Kirkpatrick–Baez (KB) mirrors that were elliptically bent and placed in a vacuum box with the alpha angle set at 2^0. This enabled a reduced beam foot print for maximum beam depth.

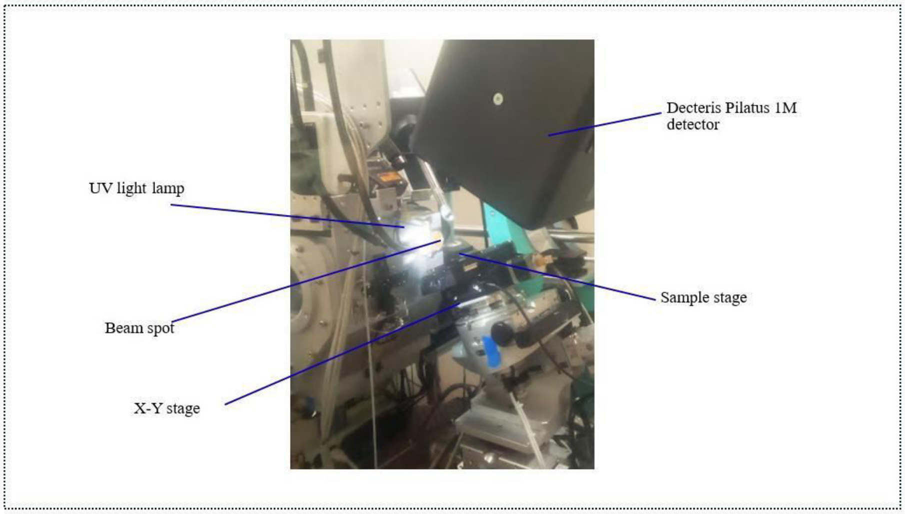

Figure 3.6. The Micro-Diffraction end-station at Beamline 12.3.2 showing various components.

A 10 keV monochromatic X-ray beam was used to measure the structural behavior of perovskite material. The monochromator and KB mirrors were placed inside a compact Plexiglas box filled with a helium atmosphere to improve thermal stability and reduce X-ray air scattering and absorption. The diffraction patterns were collected with the Pilatus3 1M detector. The sample was mounted in a 45° active geometry. The detector was placed on a vertical slide at approximately 180-190 mm for 12.3.2 from the sample area illuminated by the beam. This allows for the collection of a large solid angle in the reciprocal space without having to move the detector.

3.3.4 *In situ/Operando* Experiments

The schematic diagram of the multimodal spin-coater fitted with pyrometer, Photoluminiscence, and camera probes as shown in Figure 3.7.

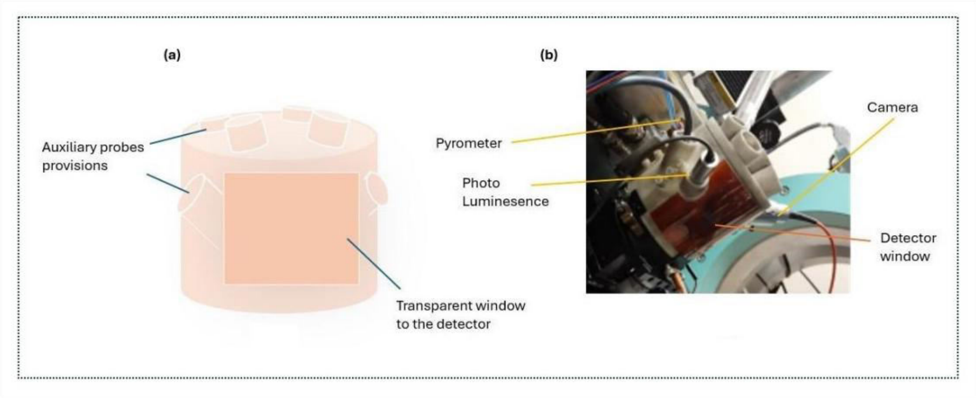

Figure 3.7: (a). The schematic diagram of the multimodal spin-coater fitted with with pyrometer, Photoluminiscence, and camera ports (b). The multimodal spin-coater mounted on the sample stage at beamline 12.3.2.

The set-up consisted of a spin-coater and a motorized syringe for remote injection of the precursor. 70 μl of the precursor solution was spin coated onto a 10 mm by 10 mm ITO substrate of resistance 30 Ω in two-steps of 1000 rpm for 10 s then 5000 rpm for 35 s. After the perovskite precursor is dropped on the substrate, concomitant GIWAXS measurement as explained in the *ex situ* procedure and sample spinning was triggered simultaneously, with a programmed helium injection on the spinning film during the 30 s spinning process at 1500 rpm.

100 μl of anti-solvent was introduced after 10 s prior to the end of spin coating to evaporate the solvent from the film. The films were annealed at 100 ^{0}C for 5 minutes on

a hot plate. The spinning parameters, temperature controls and data acquisitions were done by the XRDsol, Labview interface.

3.3.5. *In situ* experiment parameters

The schematic diagram of the multimodal spin-coater fitted with with pyrometer, Photouminiscence, and camera probes. The precursor solution was spin coated onto an ITO substrate in two-steps. Figure 5.9 (a) shows the spin motor revolutions plot as a function of time**.** The first step lasted for about 10 s before the 35 s during long for the second step.

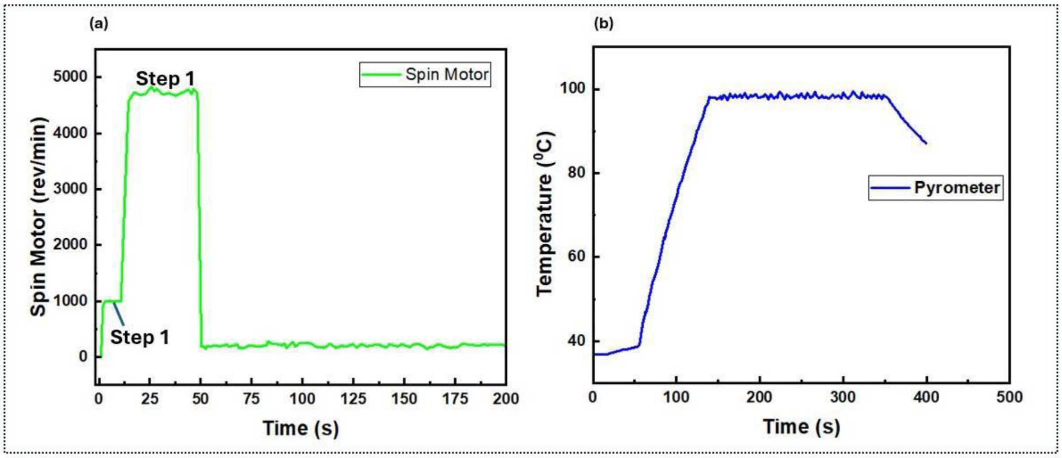

Figure 5.8: Parameters for the *in situ* process; a. The two step spin-coating profile b. The pyrometer profile c. The variation of heater voltage, mono energy and the beam current during the *in situ* process.

The films were annealed at 100 ^{0}C (shown by the pyrometer scale in Figure 5.9 (b)) for 5 minutes on a hot. The whole spinning and annealing process took approximately 350 s. The spinning parameters, temperature controls and data acquisitions was done by the XRDsol and Labview interface. The challenges of overheating and the sample 'flying off' from the rotating disk were reported during the measurements. These were taken care off by subsequently cooling the spinning stage, and alternate use of different sample holders.

3.3.6 *In Situ* Photo-luminescence Fluorescence and UV-Vis spectroscopy.

In situ PL was performed both at the molecular foundry and at ALS beamline 12.3.2 during the *in situ* GIWAXS measurements. At the molecular foundry, the nikon LP camera was used to detect the emission produced by the film during both the spinning and the film annealing process.

The camera was placed at a sample-detector distance of about 150 mm. During spinning, the precursor solution was dropped on the substrate and commenced the spinning process. The film was then transferred on a hot plate and annealed at 100 ^{0}C for 5 minutes. The PL data was acquired by the external computer controlled by the bluetooth connected mouse in the glovebox. The OceanView 2.0.13-EZ software was used in data acquisition in which the data update rate was set at 5 ms, an automatic integration time of 10 s, and scan averages were set to range between 100 to 200 counts. The experiment was performed in the dark to eliminate noise.

For the ALS PL measurements, a Nikon LP-EPILED microscope with a Pixelink PL-B742FF camera was attached above the spin-coating system, in one of the ancillary ports to observe the kinetics of crystallization of the perovskite solution. The spin parameters and hutch operations remained the same as for *in situ* GIWAXS, since the PL measurements was done simultaneously with the GIWAXS. Lenses with 40× and 60× magnifications was used. The image stacks were processed by the LabVIEW software.

In situ UV-Vis Spectroscopy (or Spectrophotometry) was done at the glovebox during the fabrication process. The UV-Vis wavelength range was set at 190 nm to 2.5 μm. The optical white light was positioned below the sample and the detector camera placed above the sample. The OceanView 2.0.13-EZ software was used in data acquisition as in the PL measurements, however, the acquisition mode was set to transmission mode and the absorption was a percentage difference of the transmission. The data update rate was set at 5 ms, with an automatic integration time of 100 s, and scan averages of 10 counts. The white beam was set to background before commencing the experiment.

3.3.7 AFM, SEM and EDS Measurements

Asylum Cypher ES Atomic Force Microscope at the molecular foundry was used. This microscope had a 40-micron scanner with high precision sensors which allowed molecular lattice resolved imaging in a closed loop measured. The integrated optics were excellent and allowed precise positioning of the sample before engagement. The integrated optics was adjusted to accommodate the 15 mm samples in length. Kelvin probe surface potential imaging was used during the measurements. VRS sample stage was set at approximately 10 frames per second for high speed scanning then following procedure; Selected a measurement sample, installed an AFM probe, aligned the laser optics, determine the AFM cantilever resonance frequency for tapping mode operation, adjusted the interaction force, optimized the scan parameters, engaged the AFM probe, scanned the sample surface, and finally analyzed the scan.

FEI Phenom tabletop Scanning Electron Microscope at the Molecular Foundry was used SEM measurements, which had a light optical camera with a magnification of 20-134x, and an electron optical magnification range of 200-1,000,000x (and down to 10 nm particle resolution). It was used to handle sample sizes of 15 mm in length. Energy-Dispersive X-ray Spectrometer (EDS) was coupled with the SEM for mapping and elemental analysis. SEM was used to reveal information about the sample including external morphology (texture), chemical composition, and crystalline structure and orientation of materials making up the sample.

3.4 Data analysis Techniques

3.4.1 GIWAXS 7.3.3 Analysis

Igor Pro (shown in appendix 2) commercial software installed with Nika was used for data analysis. The 2D GIWAXS detector images were calibrated with Nika General Binary parameters 1475 X 1679 for $x \times y$ number of points, with a CCD pixel size of 0.172 (mm), sample detector distance ranging from 270 mm – 280 mm then optimized depending on the *q*-range (scattering vector) and detector size. X-ray energy of 10 keV set from the main window. This was followed by the refinement of the beam center and calibration using the silver behenate (AgB) sample.

Typical line cuts sections were performed to form a 1D intensity versus reciprocal vector in *q,* which allowed for more qualitative analysis of peak evolution during crystallization (Aidan H. C. *et al*., 2023 and Chenhui Z. *et al*, 2023). 2D images were processed using the 'WAXStools' window in which the parameter for, CCD pixel size, sample detector distance, X-ray energy, and the alpha angle were set then we developed then a log file in the *r*-space finally developed to generate the 2D images in *q* space.

3.4.2 Micro-diffraction and *in situ* GIWAXS at 12.3.2 Analysis

The custom-made XRDSol software (Appendix 3) at beamline 12.3.2 was utilized, in which loading the calibration image of Alumina into the main visualization window was the initial step. The calibration parameters included an energy bandpass (polychromatic beam) ranging from 5 keV to 30 keV, along with a monochromatic beam setting of 10 keV and a wavelength of 1.24 Å.

Powder diffraction measurements were performed using standard Al_2O_3, with a 2θ range of 5 ^{0} to 30 ^{0} and a Chi range of -20 ^{0} to 20 ^{0}, maintaining a resolution factor of 0.1. Scan processing involved full 2θ integration, peak development, and generating CSV data files, which was converted from 2θ to q-space. The resulting CSV files were then used to develop 1D peaks using Origin software and python script.

3.4.3 *In situ* PL and UV-Vis

The data collected using the OceanView 2.0.13-EZ software was to serve as the foundation for further spectral analysis. The raw output was processed to generate both two-dimensional (2D) spectral maps and one-dimensional (1D) intensity profiles. For this purpose, a customized and dedicated Python script within the Anaconda environment, tailored specifically to handle, visualize, and interpret the data efficiently was developed. The script enabled automated extraction, normalization, and plotting of the spectra, that ensured consistent and reproducible analysis across multiple datasets.

CHAPTER FOUR
RESULTS AND DISCUSSION

$Cs_{0.05}(Fa_{0.83}Ma_{0.17})_{0.95}Pb(I_{0.83}Br_{0.17})_3$ Stability Under Non-Equilibrium Humidity Conditions Through *Ex Situ* Giwaxs And Micro-Diffraction Analysis

4.1 Chapter Introduction

The results obtained herein were presented as *ex situ* measurements satisfying objective one. The structural analysis on the fabricated perovskites identified the phases inherent before performing GIWAXS techniques with humidity tolerance. The surface dynamics of the films were then performed by SEM, and AFM methods optimizing the triple cation from the Molecular Foundry, published in (Shatsala M., *et al*. 2025).

4.2 Phase identification using μ-XRD with chlorobenzene and ethyl acetate antisolvent treatment

Static x-ray micro-diffraction microscopy was used to identify the type of films through the micro-peaks which is a technique that use small spots on samples with strong gradients in composition, to determine contaminations and inclusions in the films. The 3-CAT results were compared with the MAPI which was the specific modus operandi; presented in form of maps and diffraction peaks. The comparison was of essence since not only did it produce finite compositions in the material but also supported strong discussions from the GIWAXS reports.

The pattern maps obtained for both MAPI treated in EA and CB show peaks with typical perovskite peaks at $2\theta^0 = 14.01^0$ as seen in Figure 4.1. The experiment, having been performed with anti-solvents technique, discovered that the film formation mechanism extremely depended on anti-solvents used, with peaks delineating different planes for various anti-solvents comparable to peaks reported with others (Luo, S. *et al*., 2016).

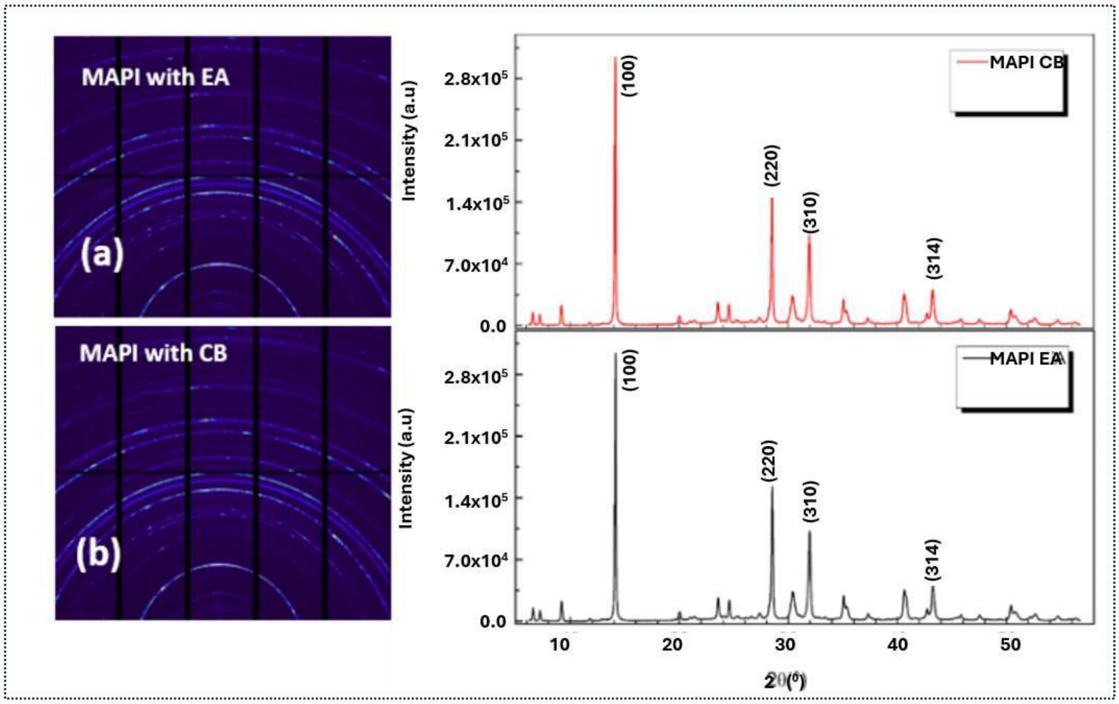

Figure 4.1: Micro-diffraction synchrotron maps (a) MAPI treated with EA (b) MAPI treated with CB and their corresponding 1D line-cut plots.

Pure EA (ethyl acetate) used for both triple cation (3-CAT) shown in Figure 4.1(a) and Methylammonium Lead Iodide (MAPI) given in Figure 4.2(a) produced similar peaks with CB (chlorobenzene), which illustrated typical perovskite peaks of (100) with small peaks of crystal planes of (220), (310) and (314) that corresponded to plane angles of 14.1^0, 28.5^0, and 34.1^0, respectively (Shatsala M., *et al*. 2025), as discussed in other researches (Zhao H. *et al*., 2019).

However, EA produced some diminished peaks at 8.3^0 and 9^0 for both MAPI and 3-CAT as exhibited in Figure 4.1(a), and Figure 4.2(a) respectively, which was presumed to be due to non-converted perovskite precursors (Rahim A. *et al.*, 2015). These parasitic peaks created pinholes in the film, increasing resistance and consequently reducing charge transport. CB treatment eliminated these peaks at 8.3^0 and 9^0 for 3-CAT films and introduced more perovskite crystal plane of (112), (211), (220), (310) and (314) at $2\theta^0$ = 20.0^0, 25.0^0, 28.8^0,32.1^0 and 43.0^0, respectively (Shatsala M., *et al.* 2025), as seen in Figure 4.2 (b) (Zhao H. *et al.*, 2019), (Rahim A. *et al.*, 2015), (Basumatary P. and Pratima A. 2020) and (Mirhendi S. M. *et al.*, 2017). Both EA and CB treatment in MAPI produced small peaks before 10.0^0 which were attributed to incomplete precursor conversion to perovskite phase.

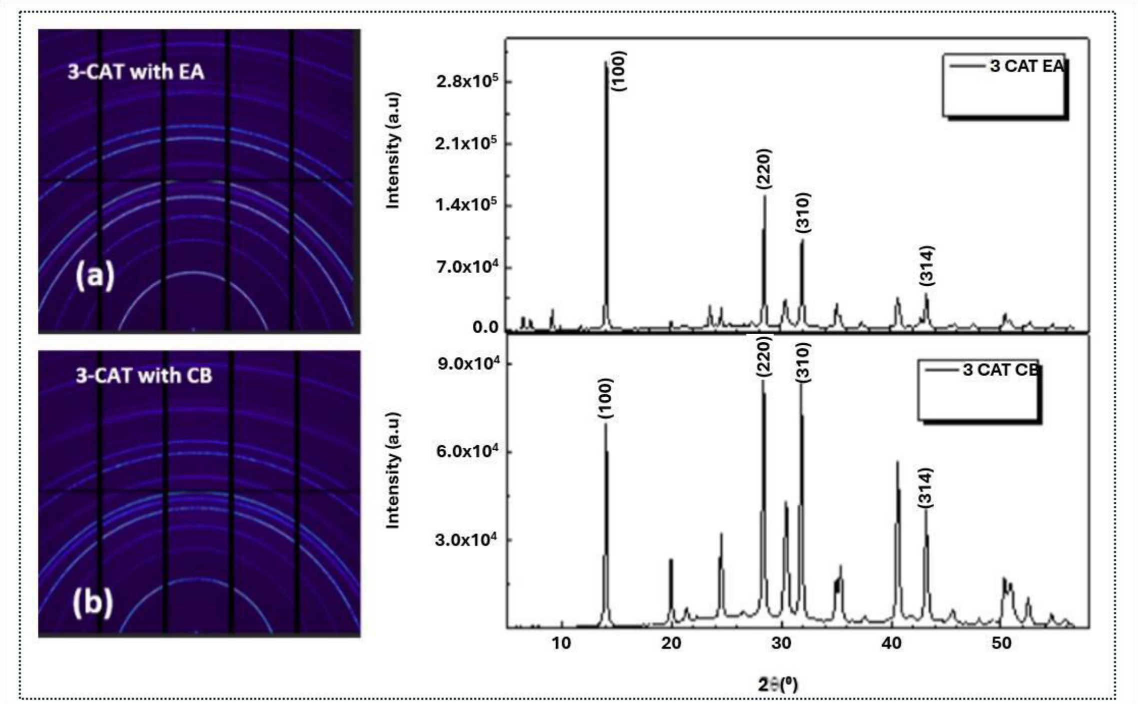

Figure 4.2: Micro-diffraction peaks for 3-CAT dissolved in both EA and CB. Sharp peaks of the perovskite phase (100) with small peaks of crystal planes of (220), (310) and (314) corresponding to plane angles of 14.1^0, 28.5^0, 34.1^0 and 43.6^0 respectively as seen from the line-cut 1D plots.

A comparative study of the crystal planes produced for 3-CAT as presented in Figure 4.2, gave CB an edge over EA; however, there was no effect on MAPI with treatment of both EA and CB (Figure 4.1) due to reduced parasitic peaks. Furthermore, the intensities of the peaks produced by EA were lower with maximum intensity values of 3.0 x 10^5 (arb. un.) for both MAPI and 3-CAT, while CB, engendered a maximum peak of 7.0 x 10^5 (arb. un.) as shown in Figure 4.2(b). This implied that CB caused a greater amount of crystals with distinct spacing (Franklin & Marchall C., 2024).

The peaks were also thinner which corresponded to bigger crystal formation and the larger grain size. This contributed to longer carrier lifetime and smaller carrier transport resistance (Rong S.S., *et al.*, 2021), together with credible information on the reduced recombination in the perovskite films fabricated (Franklin & Marchall C., 2024), which were beneficial for solar cell devices.

4.3 GIWAXS Results on $Cs_{0.05}(FA_{0.83}MA_{0.17})_{0.95}Pb(I_{0.83}BR_{0.17})_3$

4.3.1 Effects of varying the concentration of cesium cation in the triple cation

Triple cation films were fabricated by varying the percentage of cesium, where cesium cation ($Cs^{+)}$ was added in $FA_{0.83}MA_{0.17}Pb(I_{0.83}Br_{0.17})_3$ to form $Cs_x(FA_{0.83}MA_{0.17})_{1-x}Pb(I_{0.83}Br_{0.17})_3$ with x= 0 %, 5 %, 10 %, 15 % and, 20 %. Subsequently, the crystal phases of the films as exhibited by static GIWAXS analysis was determined. Figure 4.3(a) shows the GIWAXS maps of the peaks when no Cs^+ was added to the triple cation. The peaks appeared at q = 0.9 $Å^{-1}$ and at q = 0.83 $Å^{-1}$, which corresponded to PbI_2 and the δ-intermediate yellow phase of $FAPbI_3$, respectively, while the α-black phase (100) at q = 1.0 $Å^{-1}$ was sheer insignificant.

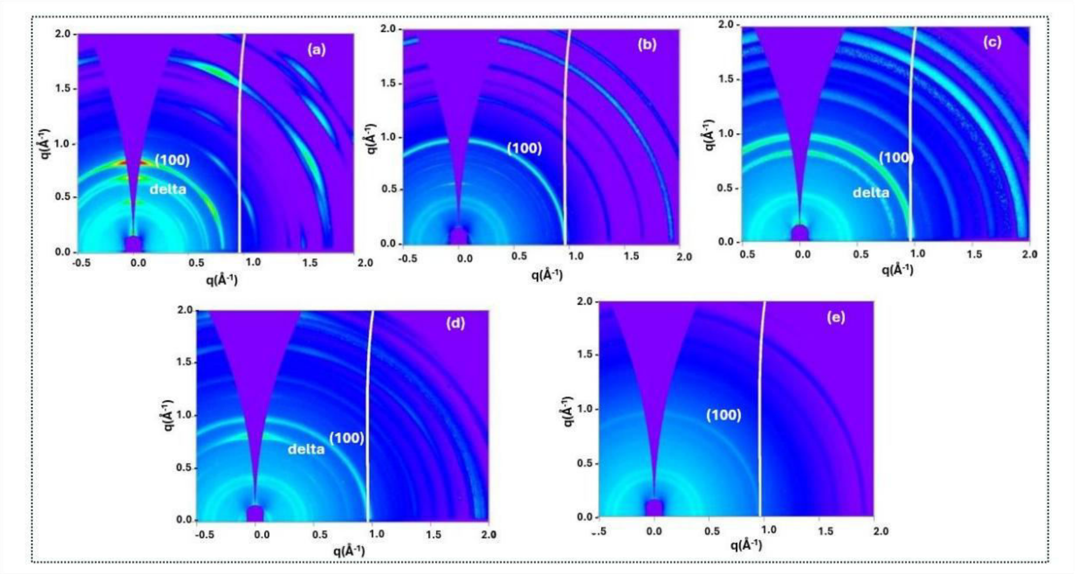

Figure 4.3: GIWAXS maps of triple cation (3-CAT) with varying cesium concentration in triple cation at (a) 0% Cs ; (b) 5% Cs; (c) 10% Cs; (d) 15% Cs and (e) 20% Cs.

However, addition of cesium to the triple cation improved the crystallization process with the formation of the α-black phase at (100) conspicuously appearing at q =1.0 Å^{-1} when the percentage of cesium was increased to 5%, 10%, 15% and 20% as shown in Figure 4.3 (b - e). It was noted that, 5% cesium produced the best crystal structure formation with no δ-intermediate hexagonal phase of $FAPbI_3$ or PbI_2 peaks.

In contrast, 10%, 15% and 20% produced PbI_2 peaks were produced and the intermediate phases which resulted from incomplete conversion to α-cubic phase of perovskite due to large cation compositions or dense crystal points that delayed the transition process (Shatsala M., *et al*. 2025). It was postulated that the films needed to be annealed within the annealing window with optimized temperature conditions to avoid the formation of intermediate phases in the process of crystallization (Qin M. *et al*., 2019).

Remarkably, the addition of 5% cesium in the mixed perovskites improved the crystallization of the perovskite film (Saliba M. *et al.*, 2018) by-passing the hexagonal phase during spin coating process. Furthermore, it was observed during spin-coating when ethyl acetate (EA)/chlorobenzene (CB) was added some 5s to the end of process that, a brown phase appeared which was responsible for the peaks at q = 0.86 $Å^{-1}$, observations which were not made when Cs^+ was not added. With slight annealing time of approximately 3-5 min the α-black phase was formed. This indicates that Cs^+ markedly enhances the crystallization of the desired α-black perovskite phase, in agreement with previous reports by Mittal et al. (2023) and Jeon et al. (2015).

4.3.2 Phase Segregation on the Relative Humidity (RH) probing

a. Effects of RH on 5% Cs triple cation

Figure 4.4 shows the GIWAXS maps for 5% Cs which was an exposition of its phase segregation when subjected to humidity. In Figure 4.4 (a) the bright peak at $q = 1.0$ $Å^{-1}$ clearly depicts the cubic perovskite phase that demonstrates that no segregation to intermediate phases when not exposed to humidity. When the films were exposed to low relative humidity of 11%, parasitic peaks were immediately seen as shown in Figure 4.4 (b).

The upshot showed a weak peak at $q = 0.83$ $Å^{-1}$ after an exposure time of 10s, although the intensity of the peak at q=1.0 $Å^{-1}$ was still brighter and stronger. The peak at $q = 0.83$ $Å^{-1}$ showed that the film slightly segregates into hexagonal phase, with the cubic phase still remaining stable (Qin M. *et al.*, 2019; Dang H.X. *et al.*, 2019 and Guo X., *et al.*, 2021).

Similar results were also observed with other values of RH as shown in Figure 4.4(c) for RH value of 44%, and Figure 4.4 (d) for RH value of 88%, respectively. For a RH value of 88% the peak at q = 0.83 Å^{-1} brightened that give more information about the phase changes (Shatsala M., *et al*. 2025).

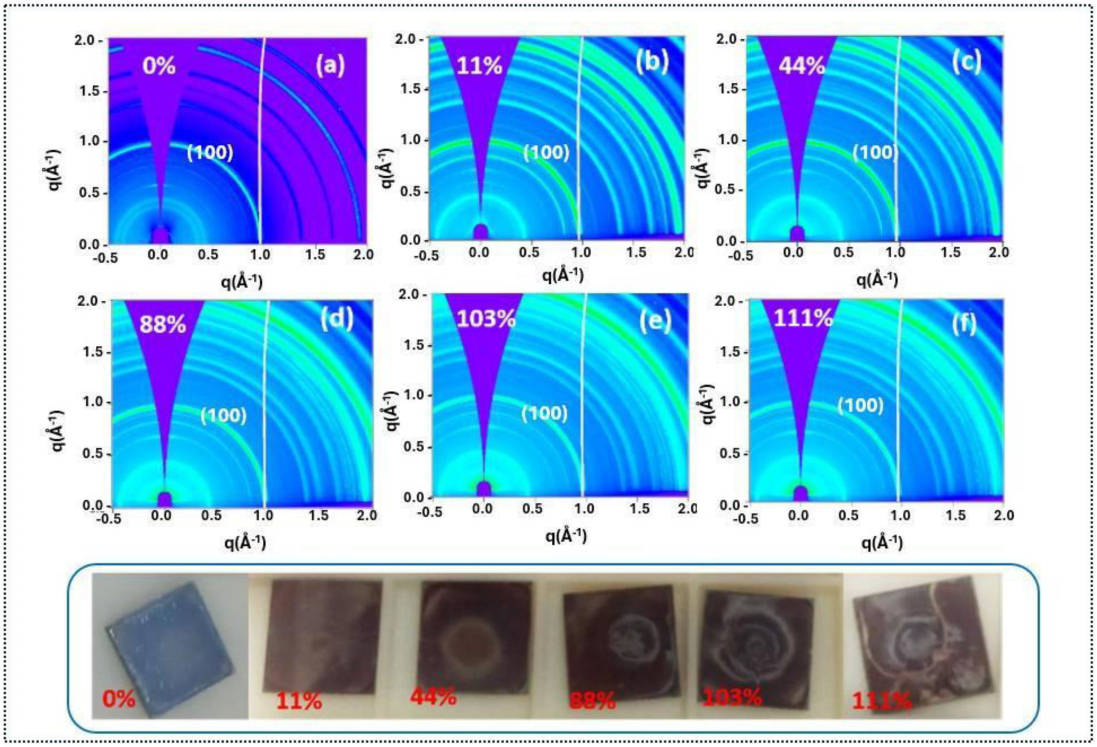

Figure 4.4: GIWAXS maps of triple cation (3-CAT) upon exposure to moisture of relative humidity for (a) 0% (b) 11 % (c) 44 % (d) 88 % (e) 103% and (f) 111 %. The real perovskite films with respective humidities are shown.

However, when the RH values were elevated beyond 100% the intensity of the peak at q = 1.0 Å^{-1} lost its strength and became weaker. There was accretion of more peaks with a double peak appearing at q = 0.83 Å^{-1} and q = 0.9 Å^{-1}. These peaks occurred because the perovskite films could no longer withstand the elevated humid conditions hence the cubic phase disintegrated into the hexagonal phase and also sets up the PbI_2 phase.

Figure 4.5 reports the 1D peaks drawn from the RH value of 111%, which showed an evident cubic perovskite (100) phase still withstanding the humid conditions at q = 1.0 Å^{-1} (Shatsala M., *et al*. 2025).

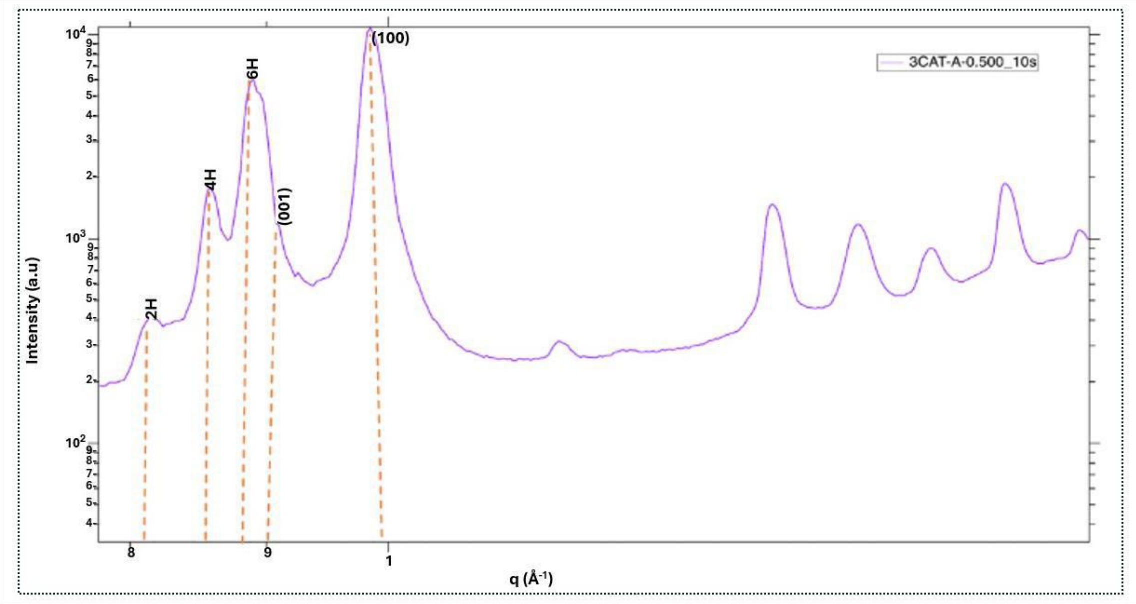

Figure 4.5: GIWAXS of triple cation with 5% Cs in q-space for RH of 111%.

However, there were accompanied crystal planes at q = 0.83 Å^{-1} (2H), double peaks at q = 0.86 Å^{-1} (4H) & 0.87 Å^{-1} (6H) and a minor peak at 0.89 Å^{-1} (PbI_2) which were as a result of phase segregation; recounting the hexagonal phases which were similar to other results reported elsewhere (Guo X. *et al.*, 2021; Li, D. *et al.*, 2016 and Kazemi M. *et al.*, 2023). The segregation of 3-CAT back to intermediate phases due to humidity exposure was attributed to hydrophilic bonds introduced during the 3-CAT formation, which made humidity prey on them leaving the film disoriented. In addition, the annealing window and anti-solvent dripping time and amounts of solvent and anti-solvents were all paramount in full perovskite phase conversion and phase stability (Shatsala M., *et al.* 2025).

b. Effects of RH on MAPI

The same tests were performed on MAPI for purposes of comparision with 3-CAT as shown in Figure 4.6**.** It was evident that humidity had little influence on MAPI as compared to 3-CAT, unlike temperature which vaporizes MA in MAPI but 3-CAT remains stable (Palazon F. *et al.*, 2018). The maps in Figure 4.6 (a) obtained from the GIWAXS measurements displayed that without relative humidity (RH), MAPI does not show PbI_2 and intermediate phases.

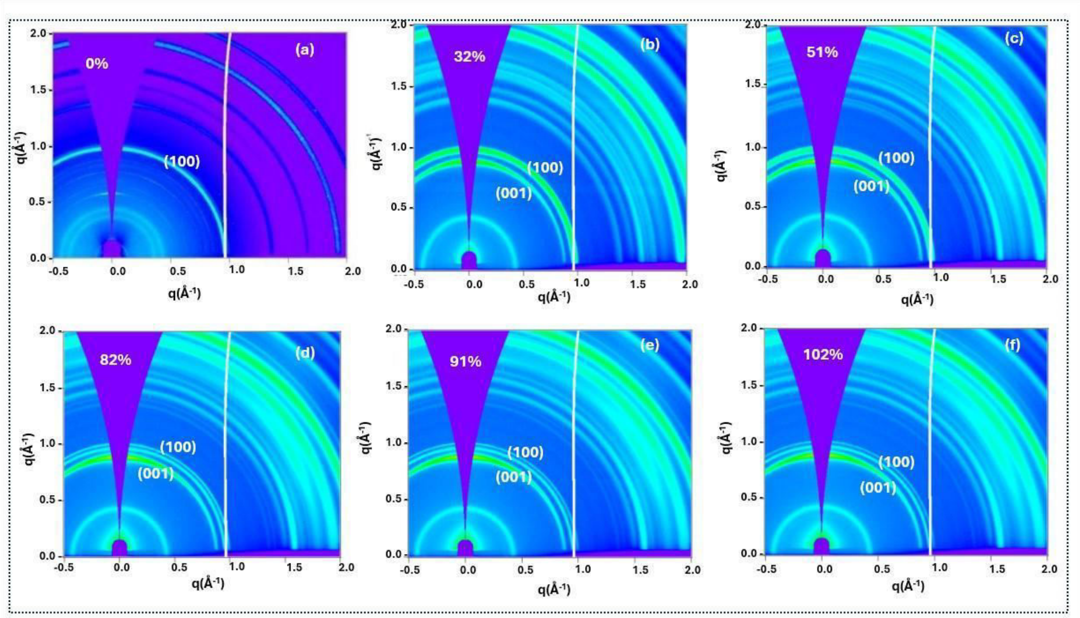

Figure 4.6. GIWAXS maps of MAPI when exposed to relative humidity (RH) of (a) 0% % (b) 32%; (c) 51% (d) 82% (e) 91% and (f) 102%.

These results were also supported by the *q*-space plot as shown in Figure 4.7 (a). However, RH values of 32% Figure 4.6 (b), 51% Figure 4.6 (c), 82% Figure 4.6 (d), 92% Figure 4.6 (e) and 102% Figure 4.6 (f) for an exposure time of 10s, presented distinct peaks at $q = 1.0$ Å^{-1} corresponding to the typical perovskite phase of (100). In addition, there was a small peak at $q = 0.9$ Å^{-1} that correlated to (001) PbI_2 phase, which was also supported by 1D line cuts in Figure 4.7 (b). It was also concluded that, with increasing RH levels from 32% to 102%, MAPI (100) perovskite phase remains stable with slight shift back to (001) phase corresponding to PbI_2 at 0.9 Å^{-1} (Shatsala M., *et al.* 2025). `

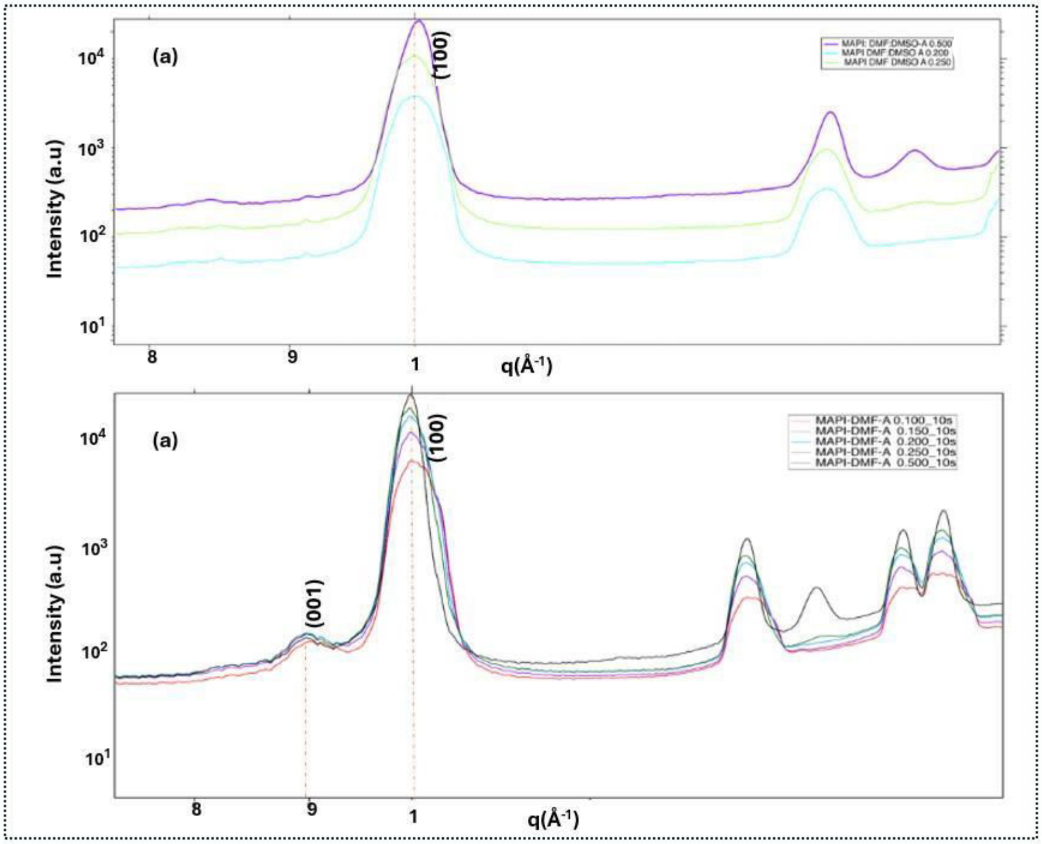

Figure 4.7: GIWAXS peaks of MAPI when exposed to relative humidity (RH).

In Figure 4.6 (b-d) perovskite the peak of (100) at q = 1.0 Å^{-1} was still intensely seen with other smaller peaks that appeared at q value of 0.9 Å^{-1}. The small peak at q = 0.9 Å^{-1} was as a result of segregated films back to the (001) phase which intensified as RH was increased. It was deduced that, although humidity had an effect on the crystallization of MAPI, the crystals remain slightly resistant to low value of RH stress and slightly degraded to PbI_2 phase as RH values were increased, to (001) crystal planes as reported by other findings (Dohert T.A.S. *et al.*, 2021).

4.4 AFM and SEM results

4.4.1 Atomic Force Microscopy Report.

The atomic force microscopy (AFM) topographical maps for $Cs_x(MA_{0.17}FA_{0.83})_{1-x}Pb(I_{0.83}Br_{0.17})_3$; x = 0.05, 0.10 were presented as shown in Figure 4.8. For the x = 0.15, 0.20. The films of triple cation perovskites demonstrated good topographical surface morphologies which was paramount for high efficiencies. The data revealed the root-mean-square (RMS) roughness of average grain size 18.5 nm and 28.5 nm for 0.05 and 0.10, respectively.

However, smoothness of the film deteriorated when Cs levels were increased to 0.20. Therefore, only AFM results were presented for x = 0.05 and 0.10. The results revealed smooth films which were comparable to the data presented by Dong and co-workers. Their topography data showed root-mean-square (RMS) roughness of 20.3 nm, 27.8 nm, 19.2 nm, and 22.7 nm for coloured films of $MAPbI_3$, $MAPbBrI_2$, $MAPbBr_2I$, and $MAPbBr_3$, respectively (Dong C., *et al.* 2016).

Moreover, similar findings were also presented for 3D/2D perovskite films morphology studied by Abbas, M. S. *et al.*, using AFM in the tapping mode which showed that the 3D/2D films formed smoother surfaces and long grain size as compared to pristine perovskite film (Abbas, M. S. *et al.*, 2020). They opined that, AFM images for FA^+ and Cs^+ (total 3 cations ; MA^+, An^+ and FA^+, or Cs^+ ions in the molar ratio of 0.8: 0.15: 0.5, respectively, in the perovskite precursor solution) displayed smoother perovskite films with crystal grain size larger than pure 3D $MAPbI_3$ but fractionally less than 2D/3D perovskites without FA^+ or Cs^+ ions.

The AFM data obtained agreed well with this work, in which the addition of Cs ions in the MA^+, FA^+ cations increased the crystallization of the perovskites which improved the general surface morphology. Cs^+ compacts the ions which reduced the surface voids and further decreased the crystal grain size which implied high functionality (Zhang X. *et al.*, 2018 and Chen W. *et al.*, 2020).

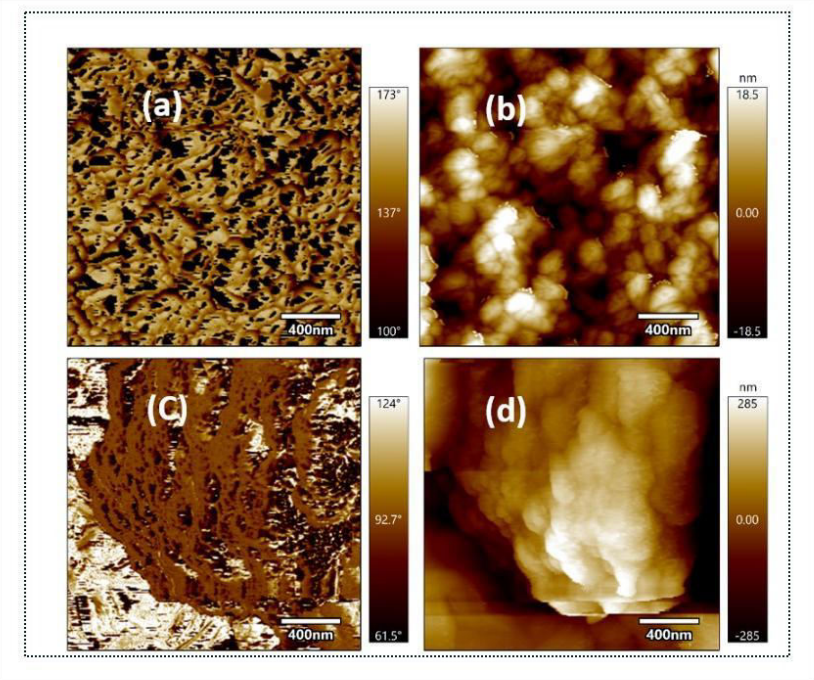

Figure 4.8: The AFM topographical maps for typical perovskite surfaces of $Cs_{0.05}(MA_{0.17}FA_{0.83})_{0.95}Pb(I_{0.83}Br_{0.17})_3$: (a) 0.05 with CB (b) 0.05 with EA. (c) 0.10 with CB and (d) 0.10 with EA.

The perovskite films were further treated with chlorobenzene (CB) and ethyl-acetate (EA) as anti-solvents. Figure 4.8 (a) showed the 5% Cs in the triple cation perovskite treated with CB anti-solvent, while in Figure 4.8 (b) it was treated with EA. This results demonstrated smoother films obtained with EA treatment as compared to CB. Similar results were depicted also when the 3-CAT perovskite films were treated with 10% Cs, as seen in Figure 4.8 (c) for CB and Figure 4.8 (d) for EA, respectively (Shatsala M., *et al*. 2025). The results compared well with the findings of S. Paek *et al.*, who discussed the treatment of perovskite films with five different anti-solvents ; trifluoro toluene (TFT), toluene, chlorobenzene (CB), xylene, ether and without any treatment, (Paek S. *et al.*, 2017). They observed that TFT produced smoother films compared to CB. Furthermore, AFM images of $FA_{0.3}MA_{0.7}PbI_{2.46}Br_{0.54}$ and $Cs_{0.05}FA_{0.3}MA_{0.7}PbI_{2.51}Br_{0.54}$ perovskite films on the ITO/PEDOT : PSS substrates showed a root mean square (RMS) value of 11.85 nm (Pang S *et al.*, 2018). Introducing Cs^{+} ions increased the RMS roughness of $Cs_{0.05}FA_{0.3}MA_{0.7}PbI_{2.51}Br_{0.54}$ films to 12.37 nm. This result shows that EA treatment smooths the film surface—an effect that enhances perovskite device performance.

4.4.2 Scanning Electron Microscopy Result

The grain size and morphology of the perovskite crystals were studied using SEM microscopy with both CB and EA treatment. In this section, measurements were made for the triple cation and for single cation (MAPI). The aim was to compare the grain size of the triple cation with well-established MAPI formation.

The results demonstrates that MAPI generated larger crystal grains as compared to 3-CAT as shown in Figure 4.9 (a) and 4.2 (c), respectively, for a scale factor of 100 nm. Similar results were obtained for a scale factor of 200 nm as shown in Figure 4.2 (b) and 4.2(d) (Shatsala M., *et al*. 2025). This was attributed to the decrease in the crystal sizes after introduction of Cs ions as observed from their Scanning Electron Microscope (SEM) images (Zhang, X. *et al*., 2020 and Chen W. *et al*., 2020).

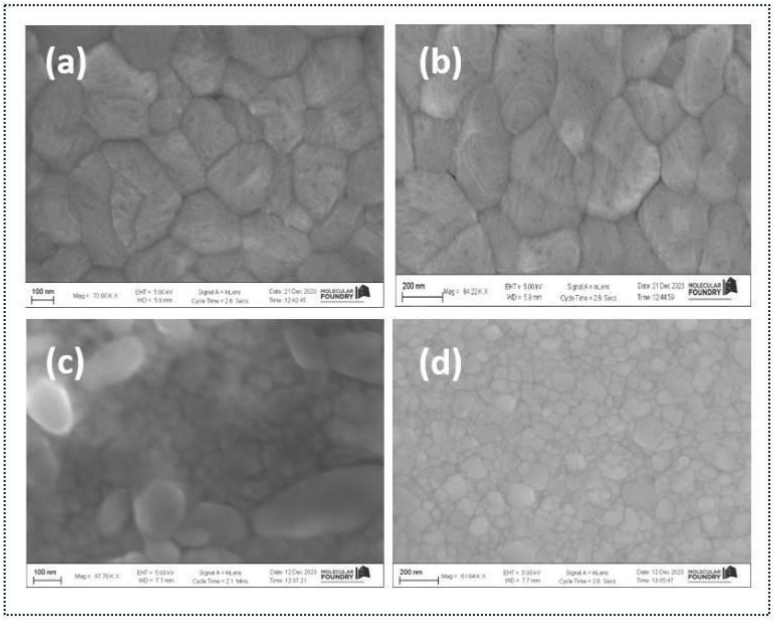

Figure 4.9: Scanning Electron Microscope Maps for typical triple cation perovskite materials. (a) MAPI with CB (b) MAPI with EA (c) 5% Cs 3-CAT CB (d) 5% Cs 3-CAT EA.

The decrease in the grain sizes solemnly, was because of slow conversion of non-perovskite hexagonal phase to the cubic perovskite phase (Ren X. *et al*., 2016; Muscarella, L. *et al*., 2019 and Chiang, C.H. *et al*., 2016). However, MAPI demonstrated larger grain sizes due to fast perovskite phase conversion.

SEM morphological characterization on MAPI and 3-CAT of 5% Cs were performed to determine the shape, crystal size and coverage of the films with CB and EA solvent treatment. The grain sizes changed significantly for a single cation perovskite (MAPI) and triple cation (3-CAT). The morphology showed that the triple cation film was dense and compact whereas MAPI films presented a less intense crystal structure as observed in Figure 4.9 (a) and 4.9 (b).

On the contrary, 3-CAT films showed mixed crystal sizes with others having larger grains while other with smaller grains as seen in Figure 4.9 (c). The larger crystals similar to MAPI, demonstrated that there was complete conversion to cubic perovskite phase structure, while the smaller crystals showed the non-converted phases of PbI_2 and hexagonal perovskite phases. These results matched with the findings obtained from synchrotron data presented in the GIWAXS measurements.

4.5 Chapter Summary

The μ-XRD pattern maps obtained for both MAPI and 3-CAT treated in EA and CB showed maps with typical perovskite peaks at $2\theta = 14.01^0$. A comparative analysis of the crystal planes produced for MAPI and 3-CAT gave CB an edge over EA; however, there was no effect on MAPI when treated with both EA and CB.

GIWAXS analysis on triple cation perovskite showed 5% cesium produced the best crystal structure formation with no δ-intermediate hexagonal or PbI_2 peaks, as compared to 10%, 15% and 20% cesium. Humidity had a strong influence on the crystallization of MAPI and 3-CAT. For MAPI, the crystals remained slightly resistant to low value of RH stress and degraded to PbI_2 phase as RH values were increased, with only (001) crystal planes appearing. When 3-CAT was subjected to RH, and the values elevated beyond 100% the intensity of the peak at $q = 1.0$ Å^{-1} became weaker. There was accretion of more peaks with a double peak appearing at $q = 0.83$ Å^{-1} and $q = 0.9$ Å^{-1}. These peaks occurred because the perovskite films could no longer withstand the elevated humid conditions hence the cubic phase disintegrated into the hexagonal and PbI_2 phase.

AFM results showed EA produced smooth films compared to CB which could be the best candidate for perovskite save for its extra peaks produced during film formation. MAPI produced larger grains than 3-CAT from the SEM findings. This was attributed to slow conversion of the hexagonal phase to the cubic perovskite phase although with a compact structure.

The complex information, real time structural evolution and more knowledge of the crystallization pathways of triple cation by GIWAXS measurements still needed further research. For instance, understanding the crystallization kinetics of triple cation (3-CAT) was rather complex due to the stoichiometry of the perovskite compositions that could have been better preserved by applying the anti-solvent via carrier-gas free spraying (Telschow, O. *et al*. 2022).

Optimization of the anti-solvent dropping time and quantities for EA to limit the pre-perovskite phase emergence was proposed. The studies on anti-solvent dropping conditions on 3-CAT perovskite films under inert conditions at room temperatures revealed that, CB with right combination of relative humidity and anti-solvent dropping time could affect the (100) orientation of crystal growth and can result in pinhole-free perovskites (Hosseinmardi, A., A. *et al.*, 2020).

CHAPTER FIVE

RESULTS AND DISCUSSION

In-Situ Insights Into $Cs_{0.1}Fa_{0.9}PbI_3$ Perovskite Evolution PEACl-PPF Co-Passivated Thin Film Growth

5.1 Chapter Introduction

In situ GIWAXS and photoluminescence of $Cs_{0.1}FA_{0.9}PbI_3$ film, passivated with PEACl and PPF, revealed that co-passivation suppressed the transient δ-phase, and promoted direct α-phase formation. PEACl-PPF synergy modulated crystallization kinetics where it stabilized precursor complexes, slowed nucleation, and fostered controlled crystal growth. PPF's coordination with Pb^{2+} and halide ions minimized δ-phase nucleation and supported stable α-phase development, this offered valuable insights into perovskite films for advanced optoelectronic applications. The design of the *in situ* process and is given in Figure 5.1. This chapter gives results for objective two and three.

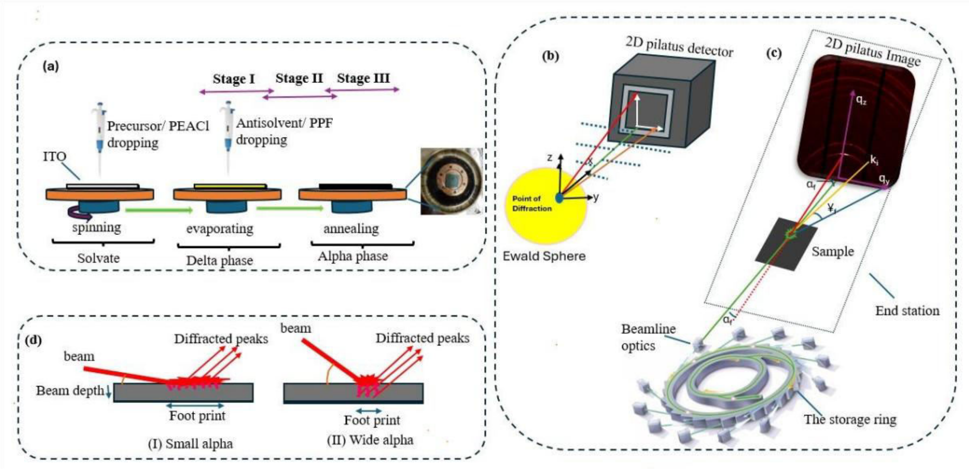

Figure 5.1: **(a)** Systematic growth of the perovskite from solvate to alpha phase final film, (b) Ewald's sphere of diffraction, (c) Beamline diffraction procedures (d) Small/Wide angle diffraction.

5.2 Perovskite growth with GIWAXS and Photoluminesence analysis

In situ GIWAXS studies of un-passivated and PEACl/PPF-passivated $Cs_{0.1}FA_{0.9}PbI_3$ films revealed a detailed crystallization pathway.

5.2.1 Passivation with 1.5 wt% PEACl

Initially, concentration of 1.5 wt% PEACl was used and it introduced a 2D peak, and some solvate phase still appeared in the film as shown in Figure 5.2 (a). The mole percentage of PEACl played a critical role in the passivation process. Increased PEACl levels disrupted the gradual conversion to the cubic phase, and from other results (Qin, Zhaotong, *et al.*, 2023 and Cheng, Peirui, *et al.*, 2019), there is a potential shift of the 3D perovskite structure into a 2D configuration.

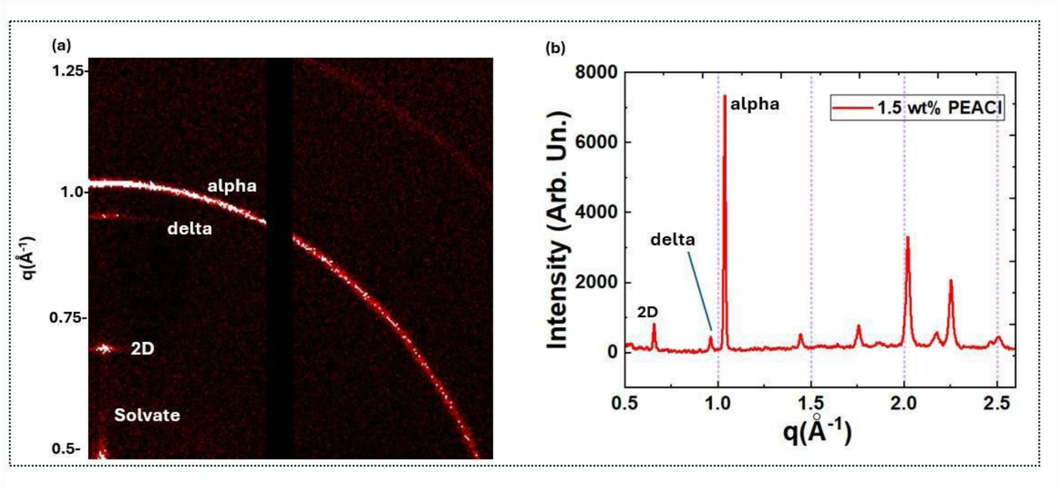

Figure 5.2: 1.5 wt% PEACl withou PPF a. A 2D peak (n_1) is introduced, with some residual solvate (n_0) present in the film. The δ-phase and α-phase are represented by peaks P_1 and P_2, respectively. b. The 1D peaks illustrate the intensity of emissions, with the PEACl peak showing significant contribution.

Additionally, the intensities displayed in Figure 5.2 (b) indicated no significant quenching of the perovskite α-phase when PEACl was increased to 1.5 wt%, which exhibited intensities that exceeded 7000 units. However, an optimized concentration of 0.03 wt% PEACl (Li, Wang, *et al.*, 2023) was identified as the preferred value due to its ability to decelerate the crystallization dynamics effectively.

5.2.2 0.03 wt% PEACl and 0.02g/mol PPF incorporation independently

In the absence of a passivant, the perovskite peaks emerged immediately upon anti-solvent deposition, which was attributed to the rapid formation of the δ-phase at $q = 0.88$ $Å^{-1}$. This lasted for less than 10 seconds then rapidly shifted to the α-phase at $q = 0.99$ $Å^{-1}$ (Figure 5.3 (a) control).

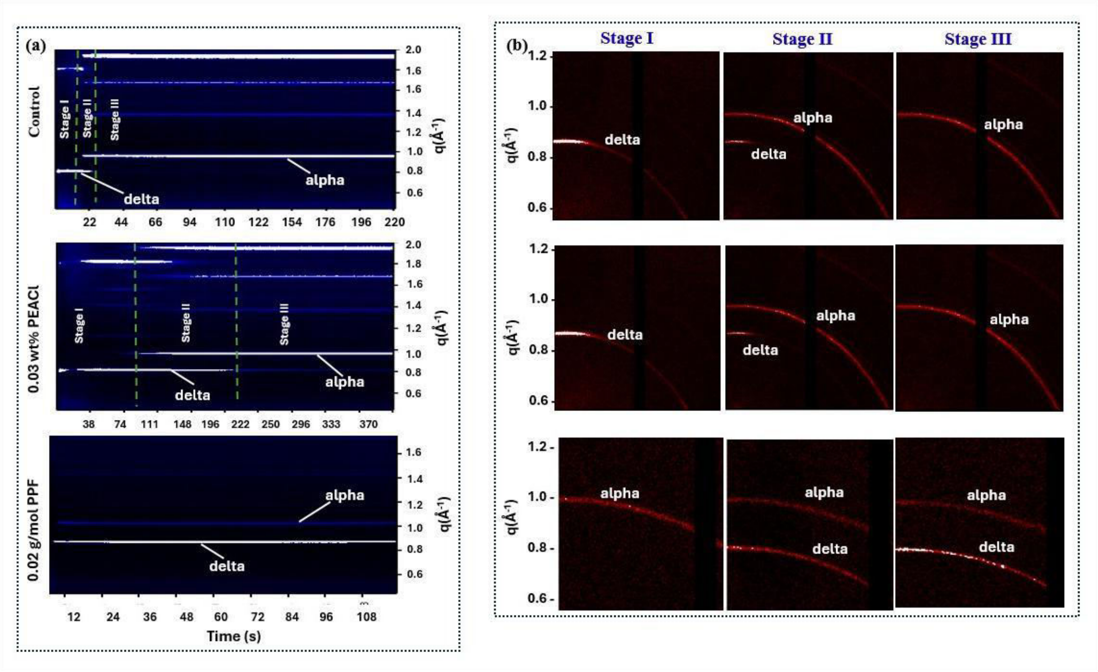

Figure 5.3: *In situ* GIWAXS studies of $Cs_{0.1}FA_{0.9}PbI_3$ films; (a) Depicts phase growth time, (b) sequential growth and phase transformations.

The progressive evolution of the perovskite phases was illustrated by XRDSol images in Figures 5.3 (b), which demonstrates the transition from the δ-phase to the final α-phase that aligned with explanations given by Qiu *et al.*, (Qiu, Shudi, *et al.*, 2024).

The δ-phase observed, corresponded to the initial stage (Stage I) of film growth, captured 15 seconds into the process. At 22 seconds there was inflection point (Stage II α-phase & δ-phase co-existed), where the δ-phase begins to transit into the α-phase. Finally, a complete conversion to the α-phase (Stage III), was observed at 200 seconds, which agreed with findings of Marronnier and others (Marronnier, Arthur, *et al.*, 2024). However, the rapid film growth and instant change from δ-phase to α-phase had detrimental effects on the stability of the photo-conductive cubic perovskite phase (Kim, Souk Y., *et al.*, 2023).

Passivated films with 0.03 wt% PEACl showed no peaks during the initial spinning process. Immediately the anti-solvent was dropped, a peak emerged at q = 0.88 Å^{-1} (Figure 5.3 PEACl) which persisted for about 200s, after which it begun to fade. Notably, as the q = 0.88 Å^{-1} peak diminished, the α-phase peak at q = 0.99 Å^{-1} gradually sets in from about the 80th second, then became more dense. The Pilatus detector images in Figures 5.3 (b) showed the maturing of the α-phase from the primitive solvate and δ-phases.

The incorporation of 0.02 g/mol PPF revealed compelling findings. Figure 5.3 (a) (PPF) showed both δ-phase and α-phase appeared immediately after abou 6 seconds. However, the α-phase at q = 0.99 Å^{-1} was greatly suppressed, but δ-phase at q = 0.86 Å^{-1} peak was enhanced. Another observation was a slight shift in the q values with PPF. The δ-phase peak shifted from q = 0.88 Å^{-1} to q = 0.86 Å^{-1}. Likewise, the α-phase shifted from q = 0.88 Å^{-1} to q = 1.01 Å^{-1}. This shift was attributed to crystal orientation (Cho, N., *et al.* 2016 and Zheng, G., et al. 2018). Other values in g/mol compositions are given in appendix 4.

The 1D profiles were derived from the sequential film growth demonstrated in Figure 5.4, which highlighted the δ-peak and α-peak growth rate in terms of the magnitude of intensities. Control and PEACl passivated films showed δ-peak that diminished with time, while α-peak at q = 0.99 Å^{-1} emerged and grew with time.

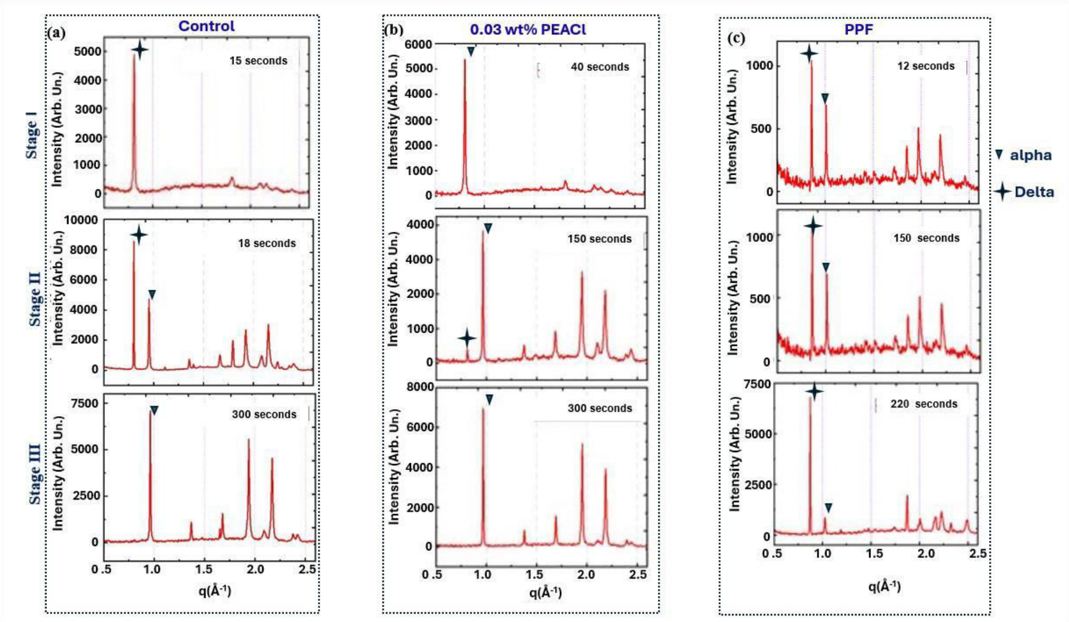

Figure 5.4: 1D profiles were derived from the sequential film growth for Cs0.1FA0.9PbI3 , 0.03 wt% PEACl and 0.02 g/mol PPF, highlighting the δ-peak and α-peak growth rate in terms of the magnitude of intensities.

The final α-phase showed good emmisivity with recorded intensity higher than 6000 units. This transition from δ-phase to α-phase, unique to the PEACl-passivated films, highlighted the effectiveness of passivation in improved film stability, that aligned with similar findings (Kodalle, T., *et al*., 2024) in which PEACl was introduced in the antisovent and significantly slowed down the crystallization process. The PPF 1D emmision intensity was observed Figure 5.4(c). For 0.02 g/mol concentration of PPF, a distinct peak appeared at q = 0.86 Å^{-1}, corresponding to the (6H-hexagonal) δ-phase

(Zakeeruddin, M., *et al*., 2022 and Shatsala, Miller, *et al*. 2025). The emission intensities of the δ-phase at $q = 0.86$ Å^{-1} increased as compared to the α-phase.

5.2.3 PEACl/PPF co-passivation

The 0.03 wt% of PEACl was combined with 0.01 g/mol and 0.02 g/mol concentrations of PPF, the δ-phase was unexpectedly eliminated during the evolution process, while the α-phase becomes more dominant. At PPF concentrations of 0.01 g/mol, the α-phase showed a comparatively faster growth rate, that started at around 15 seconds Figure 5.5 (a). However, when PPF was increased to 0.02 g/mol, it significantly delayed δ-phase perovskite formation (Figures 5.5(a)). The α-phase appeared after approximately 26 seconds, notably slower compared to completely unpassivated and PEACl passivated perovskites as observed in Figure 5.3 (a).

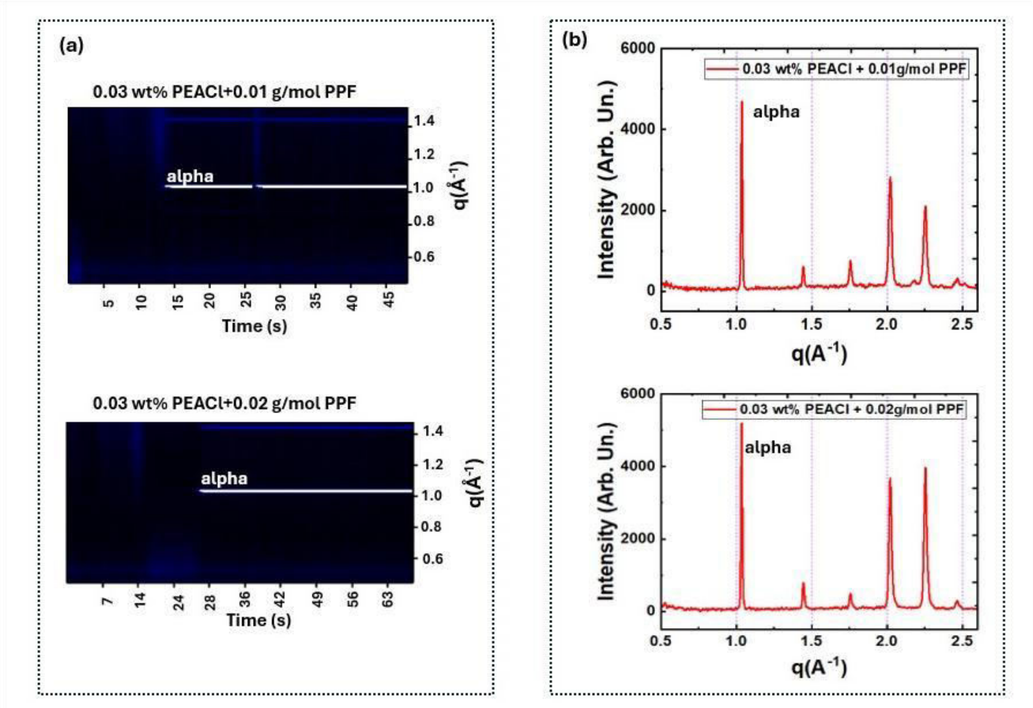

Figure 5.5: (a) XRDsol maps for $Cs_{0.1}FA_{0.9}PbI_3$, co-passivated with 0.03 wt% PEACl and 0.02 g/mol PPF, (b) 1D Intensity plots from the growth process.

Interestingly, while the α-phase formed more rapidly with PPF than with PEACl alone, the immediate formation of the δ-phase in PEACl-passivated films could have influenced the crystallization process. A major important finding was the complete elimination of the δ-phase due to PPF incorporation which was a key advantage (Wu, Xiao, *et al*., 2023 Wang, Shaofu, *et al.* 2020 Liu, Xueping, *et al*., 2023). Another significant benefit was the enhanced photo-emission observed in the co-passivated films, which reached to over 4500 units when 0.01g/mol PPF and 5000 units when 0.02 g/mol PPF was used for the α-phase, as shown in Figures 5.5 (b).

5.3 *In situ* Photo-Luminisence result

In situ photo-luminescence (PL) mapping of perovskite films is a powerful tool for monitoring real-time changes in their optoelectronic properties (Zhang, Jing, *et al*., 2020 and Schötz, Konstantin, and Fabian Panzer, 2021). Passivants in the exchange solution greatly increased the intensity of the peaks which suggested defects passivation mechanism, hence high crystallisation (Tong, Y., *et al*., 2023). The results in Figure 5.6 (a) presents an *in situ* PL contour maps for perovskite thin films subjected to various surface passivation treatments: untreated (Control), PEACl, PPF, and a combined PEACl/PPF treatments. The progressive growth of the emission contours are given in appendix 5.

The PL evolution was monitored as a function of emission wavelength (y-axis) and time (x-axis), where color gradients represented the PL intensity in arbitrary units. Compared to the control, both individual passivation strategies (PEACl and PPF) resulted in a marked enhancement in PL intensity. This was likely due to the suppressed grain boundary defects that resulted from the passivants percolation. The PEACl/PPF dual-passivated sample exhibited the most substantial PL intensity growth, which suggested a synergistic interaction between the two agents that contributed to more effective defect passivation. Across all samples, the PL peak position remained centered around 760–780 nm, and showed no significant red-shift or blue-shift (Shengliang, H., Trinchi A., Atkin P., and Ivan C., 2015), which was consistent with the emission of the perovskite phase (Liu, F. *et al*., 2017; Kong, W., Ye, Z., Qi, Z., Zhang, B., Wang, M., Rahimi-Iman, A., & Wu, H., 2015).

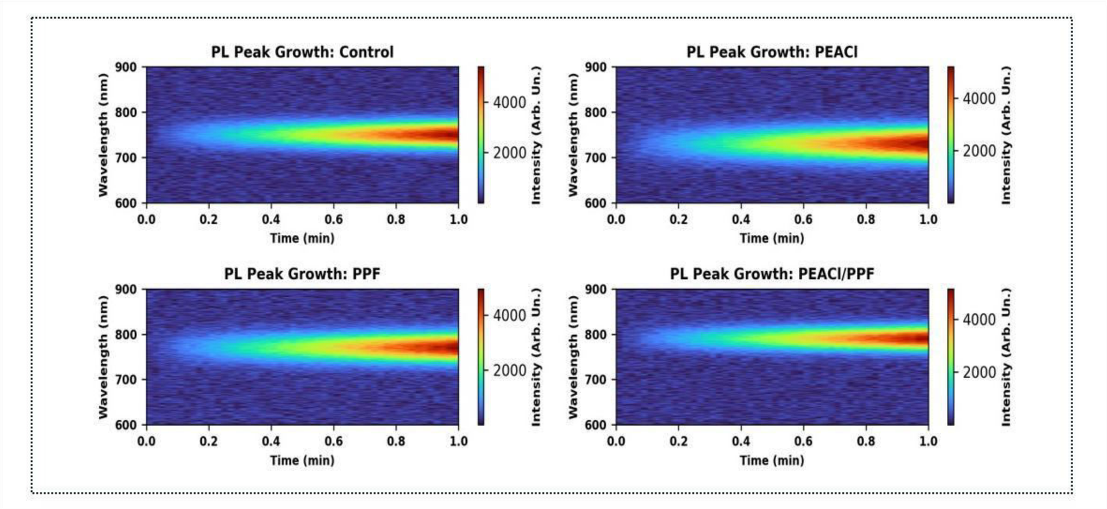

Figure 5.6: The *in situ* PL contour maps for perovskite thin films subjected to various passivation treatments: untreated (Control), PEACl, PPF, and a combined PEACl/PPF treatment.

Crystallographic orientation did not significantly affect the position of the PL peak within the wavelength spectrum, meaning that the peak wavelength remained largely unchanged regardless of the crystal orientation. However, variations in crystal quality, strain, and grain size, influenced PL characteristics to some extent (Muscarella, Loreta A., *et al.*, 2019 and Zou, Y. *et al.,* 2024).

Similar results were observed when PEACl/PPF co-passivated perovskite films were fabricated under a nitrogen atmosphere as shown in Figure 5.7. During *in situ* spin-coating, the steady-state PL spectrum, featured a dominant peak at about 1.63 eV comparable to other results (Basumatary, Pilik, Juhi Kumari, and Pratima Agarwal. 2022 and Wang, Y., Ye, S., Lim, J. W. M., Giovanni, D., Feng, M., Fu, J., & Sum, T. C. 2023).

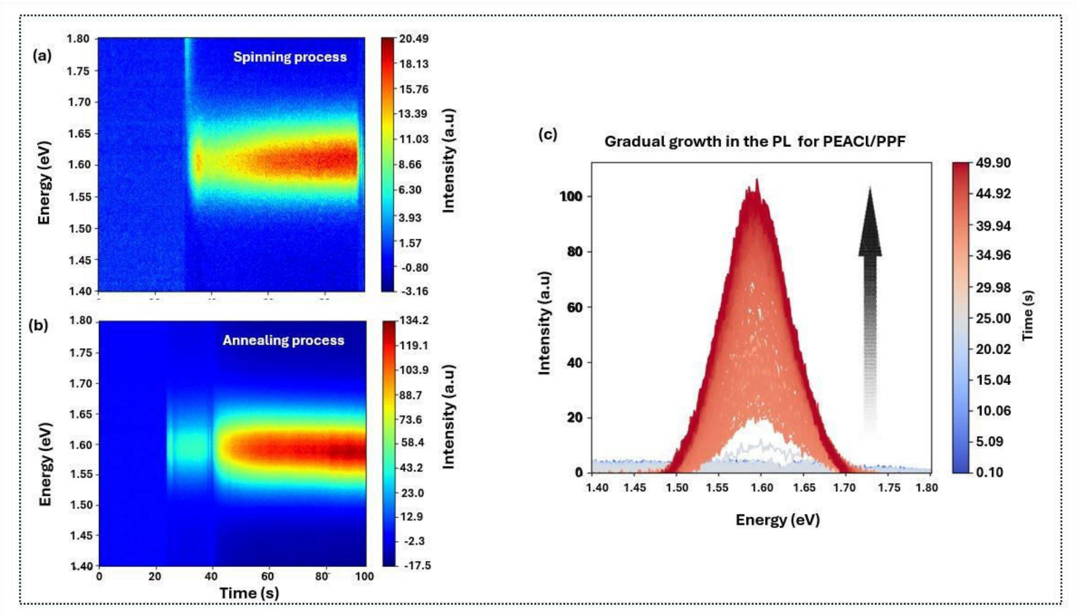

Figure 5.7: PEACl/PPF co-passivated perovskite films were fabricated under a nitrogen atmosphere; (a) spin-coating process, (b) annealing process (c) sequential tracking of the emission from the films with the intensity rising from the gray plots to the dark red plots.

The PL spectrum is dominated by bulk radiative recombination, with a weaker secondary peak arising from trap-state emission (Remmerswaal, W. H. M., 2024). PL mapping showed emission onset around 30 seconds into spin-coating, followed by a steady increased intensity, this indicated uniform nucleation, reduced non-radiative decay, and improved film formation due to effective co-passivation.

In contrast, the annealing process led to a more gradual evolution of the PL signal. The PL spectrum remained centered at about 1.63 eV with minimal trap-related features, consistent with high crystallinity and passivation. *In situ* PL data revealed a smooth, continuous increased emission intensity, which reflected progressive grain growth and further trap-state suppression as explained in other studies (Péan, E. V., Dimitrov, S., De Castro, C. S., & Davies, M. L., 2020 and Kudilatt, H., Hou, B., & Welland, M. E., 2020). While spin-coating triggered rapid nucleation, annealing facilitated a slower, thermally driven refinement of the film's microstructure, reinforcing the role of PEACl/PPF in enhanced film uniformity and optoelectronic performance. The sequential tracking of the emission from the films was given in Figure 5.7 (c) with the intensity rising from the gray plots to the dark red plots.

These results underscored the significance of interface engineering in tuning the optoelectronic properties of perovskite films and demonstrates the potential of combinatorial passivation strategies to enhance performance metrics relevant for optoelectronic devices as reported by others (Zhao, C., Zhang, H., Krishna, A., Xu, J., & Yao, J., 2024; Zhao, C., Zhang, H., Krishna, A., Xu, J., & Yao, J., 2024). Appendix 5 and appendix 6 showed a tracking of the PL for the films.

These findings were novel and had not been previously reported for PPF. The unique characteristics of PEACl-PPF co-passivation, particularly the suppression of the δ-phase and the substantial improvement in photo-emission, positively influenced the performance and stability of the resulting films. This made co-passivation with PEACl and PPF a highly promising strategy for advancing perovskite film development.

5.4 Discussion of the results

Passivating perovskite films with a combination of PEACl and PPF introduces significant changes to the crystallization kinetics and growth dynamics. These effects stem from the chemical and structural interactions of the passivating agents with the perovskite precursors and the growing film.

Initially, strong coordination between the ammonium additives (PEACl and PPF) and PbI_2 (Ferdowsi, Parnian, Ullrich Steiner, and Jovana V. Milić., 2021), drove the formation of stable precursor complexes (Rojo et al., 1992; Davidovich et al., 2009). These robust interactions with lead iodide altered the crystallization pathway, modifying nucleation and growth kinetics (Ferdowsi et al., 2021). As a result, the film morphology and phase purity were markedly improved. The phosphoryl groups (-P=O) in PPF coordinate with Pb^{2+} ions, reducing the availability of free Pb^{2+} for rapid nucleation and growth. This coordination often result in a 'hemidirected' geometry, where the Pb^{2+} ion exhibited an uneven distribution of bond lengths, leaving a 'gap' to accommodate its lone pair of electrons, a characteristic that arise from the unique electronic configuration of lead (II) ions (Persson, Ingmar, *et al.* 2011).

The phosphoryl groups possessed strong Lewis basicity (Laurence, Christian, Jérôme Graton, and Jean-François Gal., 2011 and Lin, Yu-Kuan, *et al.*, 2023), which allowed them to coordinate effectively with Pb^{2+} ions. These controls the equilibria between PbI_2, PbI_3^-, and PbI_4^{2-} shifting them to a higher coordinated plumbate species, which retard the fast crystallization of PbI_2 and intermediate phases in the precursor solution (Li, Bo, *et al.* 2019), as shown in Figure 5.8(a). This coordination modifies the crystallization kinetics, decreases the likelihood of δ-phase nucleation (Figure 5.8(b)) and enhance the uniformity of the films.

The photoemison peak intensities shifted upon the addition of PPF to the precursor solution, moving from q = 0.99 $Å^{-1}$ to q = 1.01 $Å^{-1}$. This shift is attributed to changes in the chemical environment of the phosphorus nuclei due to the interaction of the -P=O groups, as observed by Lin, Yu-Kuan *et al.* (Lin, Yu-Kuan, *et al.*, 2023). Here, the perovskite/PPF mixture causes a similar shift in phosphorus nuclear magnetic resonance (PNMR) intensities. The shift is highly associated with the microstrain in the crystal lattice due to small variations in the lattice spacing across different regions of the crystal. However, the shift is negligible at ($q = 1 \pm 0.01\,Å^{-1}$). The peaks being very narrow indicates a very low microstrain within the material (Shai, X., *et al.*, 2018 and Yang, Bowen, Dmitry Bogachuk, Jiajia Suo, Lukas Wagner, Hobeom Kim, Jaekeun Lim, A., *et al.*, 2022).

PEACl on the other hand stabilizes halide ions (I^-) potentially forming coordination complexes where the halide ions act as ligands by donating electron pairs to the positively charged nitrogen atom of the PEACl molecule (Ghosh, Sandeep, and Liberato Manna., 2018 and Li, Bo, *et al.*, 2019). The presence of PEACl in the precursor solution and PPF in the antisolvent increases the viscosity, slowing the evaporation of solvents (Rezaee, Ehsan, Wei Zhang, and S. Ravi P. Silva., 2021). This extended solvent retention delays rapid supersaturation needed for nucleation.

There is a reduction in active nucleation sites due to the introduction of PEACl and PPF. PEACl formed a passivating layer (Barua, Pranta, and Inchan Hwang., 2023 and Shao, He, *et al.*, 2020) on the initial nuclei, limiting the number of active nucleation sites. On the other hand, the bulky structure of PPF creates steric hindrance (Gao, Wenhuan, *et al*., 2024, He, Dongmei, *et al*., 2023 and Miao, Yanfeng, *et al*., 2021) at the interfaces of the growing film, thus suppressing excessive nucleation and promotes gradual grain formation.

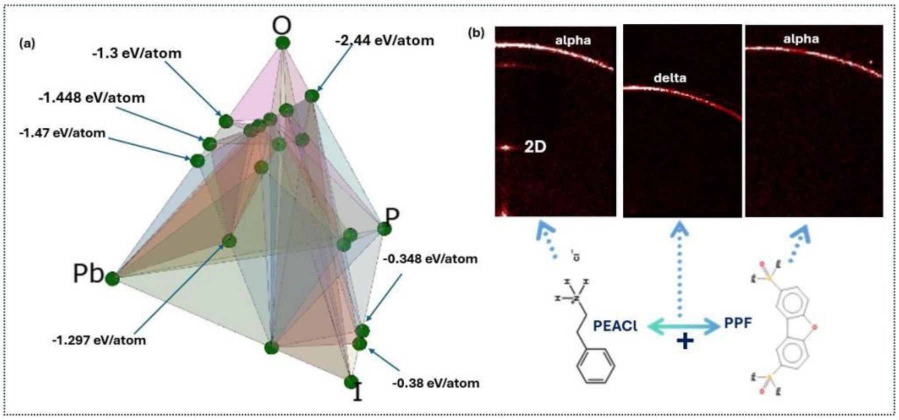

Figure 5.8: (a) Formation diagram for Pb-O-I-P; The Gibbs free energy of formation for various combinations showed that Pb-O has the lowest formation energy at -1.47 eV/atom, while the Pb-I-O combination exhibits a formation energy of -1.297 eV/atom. (b) The pilatus 1M detector images for the final phase when PEACl, PPF and PEACl/PPF is used.

The PEACl stabilizes the intermediate phase by facilitating their formation. These intermediate phases act as precursor reservoirs that release material gradually for 3D perovskite formation (Wang, Sheng, *et al*. 2019). The PPF stabilizes the α-phase by lowering its formation energy (Xie, Li-Qiang, *et al*., 2017 and Xie, Li-Qiang, *et al.*, 2017) to values as low as -1.47 eV/atom for P-O coordination, with the Pb-I-O formation energy of about -1.297 eV/atom (Harvey, M. *et al*., 2015., Jain, A., *et al*., 2013., and Bartel, Christopher J., *et al*., 2018) as shown in Figure 5.8(a). This made the direct formation of the α-phase energetically favorable during *in situ* growth.

The δ-phase is considered a kinetically trapped intermediate (Liu, Xueping, *et al.*, 2023). The strong coordination and passivation effects of PPF slowes down rapid crystallization, allowing sufficient time for the direct formation of the thermodynamically stable α-phase.

Generally, PPF introduces additional halide stabilization and surface passivation, which complements the action of PEACl. The presence of PPF promotes the growth of well-oriented crystals, which are less likely to form the randomly oriented grains characteristic of the δ-phase. Furthermore, PPF's rigid molecular framework (Di, Kaiyuan, *et al.*, 2023) enhances the mechanical and structural stability (Song, Fei, *et al.*, 2024) of the growing perovskite film, which make it less prone to transitions into the δ-phase, that forms under conditions of strain or disorder (Jiao, Yinan, *et al.*, 2021 and Zheng, Xiaojia, *et al.*, 2016).

5.5 Chapter summary

The co-passivation of $Cs_{0.1}FA_{0.9}PbI_3$ perovskite films using PEACl and PPF significantly slowed growth while improving the quality of the resulting films. This was achieved through mechanisms such as delayed grain coalescence, reduced ion mobility, and controlled nucleation. The interaction between PEACl and PPF stabilized precursor ions and intermediate phases, which created a passivating layer that reduced defects and suppressed rapid crystallization. These passivants regulated grain orientation and size distribution, that promoted the direct formation of the thermodynamically stable α-phase while bypassing the defect-prone δ-phase. Their synergistic effects also improved optoelectronic performance, and scalability by ensuring uniform, defect-free films with superior structural stability.

CHAPTER SIX

RESULTS AND DISCUSSION

Suppressing Ion Migration And Non-Radiative Recombination In $Cs_{0.1}Fa_{0.9}Pbi_3$ Through Solvent Engineering Passivation Strategies

6.1 Chapter Introduction

We discuss results for objective four using spectroscopic methods. UV-Vis absorption and photoluminescence (PL) helped to monitor changes in optical, and electrical properties. Scanning electron microscopy (SEM) assessed the surface morphology and defect formation. Energy-dispersive X-ray spectroscopy (EDS) analyzed elemental composition in the perovskite materials. Static GIWAXS provided insights into crystal structure at the nanoscale for radiative inferences.

From a broader perspective, PEACl promoted the growth of larger perovskite grains, which were essential for extending the charge carrier drift length and minimizing charge recombination. Conversely, PPF introduced a distinct bonding pattern-resembling a knit-like structure-that prevented grain cracking and segregation. This structural integrity likely accounted for the suppression of the delta phase, as discussed in Chapter 5. In a nut-shell, the applied passivation strategies enhanced film performance, as evidenced by the absorption, emission, and GIWAXS results presented in this chapter.

6.2 $Cs_{0.1}FA_{0.9}PbI_3$ Co-Passivated with PEACl-PPF

Figure 6.1 (a) shows a sequential procedure of the films growth with trapped charge carriers mechanism in the perovskite films due large grains sizes. The perovskite precursor mixed with PEACl was spin-coated, the chlorobenzene mixed with PPF dropped, then the film was annealed at 100 ^{0}C for 30 minutes.

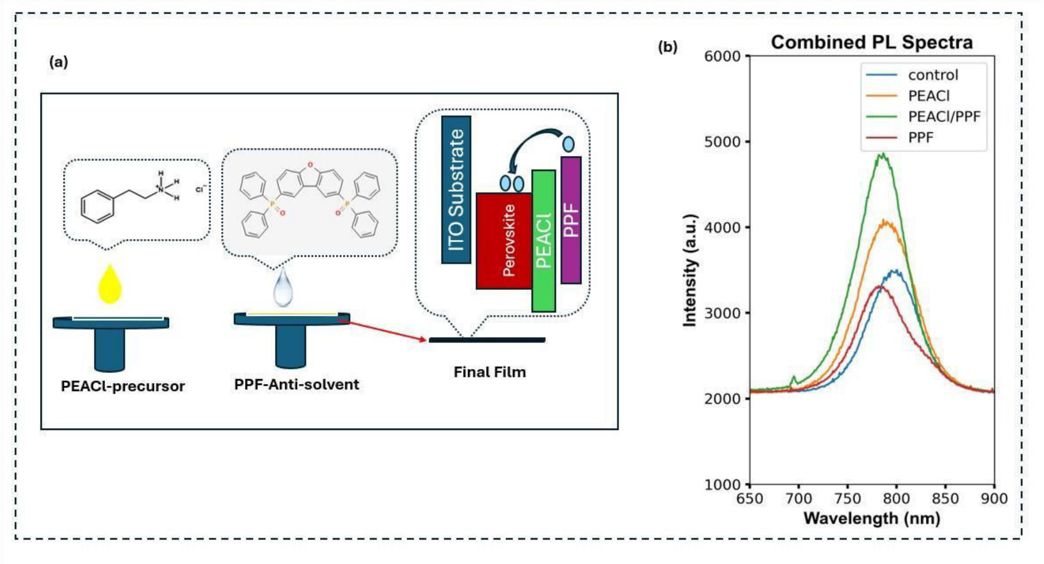

Figure 6.1: (a) Sequential process in the fabrication of the passivated perovskite with PEACl in co-operated into the precursor while PPF in the chlorobenze ati-solvent, showing ion drift back to the perovskite film. (b) the PL profiles from the control, PEACl passivated, PPF passivated, and PEACl/PPF co-passivated films.

6.2.1 Static Photo-Luminescence (PL)

The band gap information derived from the PL spectra shown in Figure 6.1 (b) exhibited sharp peaks, which is a characteristic of direct bandgaps, across all samples ($Cs_{0.1}FA_{0.9}PbI_3$, and with passivation of PEACl/PPF). This indicate minimal defects in the materials. PEACl/PPF produced narrow peaks which significantly reduce trap states and defect-induced recombination, thereby minimizing redshift in the spectrum (Wu, J., *et al.*, 2025). Additionally, the narrower peaks suggested improved grain structure and enhanced crystallinity, leading to a higher quantum yield (efficiency) as explained by Hu, M., *et al*. (Hu, M., Bi, C., Yuan, Y., Bai, Y., & Huang, J., 2015).

There was a noticeable decrease in PL peak intensity when PPF was used alone. This symbolized losses due to non- radiative processes which arose from surface defect passivation that acted as an insulator on the perovskite film. Furthermore, structural modifications were evident in the shifts observed in the PL peaks, where passivation caused an insignificant blue shift (peaks shifting to the left) which was also observed by Yoon and Lee (Yoon, B., & Lee, H., 2025).

The PEACl/PPF passivation results showed a peak at 780 nm, which corresponded to a band gap of 1.6 eV. This showed a positive transformation in the material's electronic structure which agreed with the *in situ* PL results in chapter 5 and results obtained by Singh, H., *et al*. in which potassium-doped $Cs_{0.1}FA_{0.9}PbI_3$ showed shifts in the band gap from 1.51eV to 1.58 eV (Singh, H., *et al.*, 2024). The Max-Normalized and area-normalized Pl spectra are given in appendix 6.

6.2.2 Absorption and Transmission Spectra Analysis.

The absorption and transmission spectra provided a general trend where absorption decreased as the wavelength increased, which was a characteristic of typical perovskite materials. The varying absorption intensities suggested differences in material composition, thickness, or structural properties (Castelli, I. E., Thygesen, K. S., & Jacobsen, K. W., 2015). Notably, PPF exhibited the highest absorption, indicating stronger bonding within its crystal structure compared to the other system as observed in Figure 6.2 (a). A similar trend is observed in the transmission spectra shown in Figure 6.2 (b), where transmission increased with wavelength.

The absorption edge, defined as the wavelength at which absorption drops sharply and transmission increased significantly, is located at 780 nm for PEACl and PEACl/PPF films, while PPF and control films exhibited an absorption edge above 790 nm. This provide an estimate of the optical bandgap of approximately1.6 eV for PEACl/PPF, (see

Figure 6.2 (a)). Another key observation from the absorption spectra was the film quality and uniformity. The smooth spectra with minimal noise or irregularities suggested well-formed films, while roughness or phase segregation would have meant distortions in the plots (Smith, B., 2016; Larruquert, J. I., 2018).

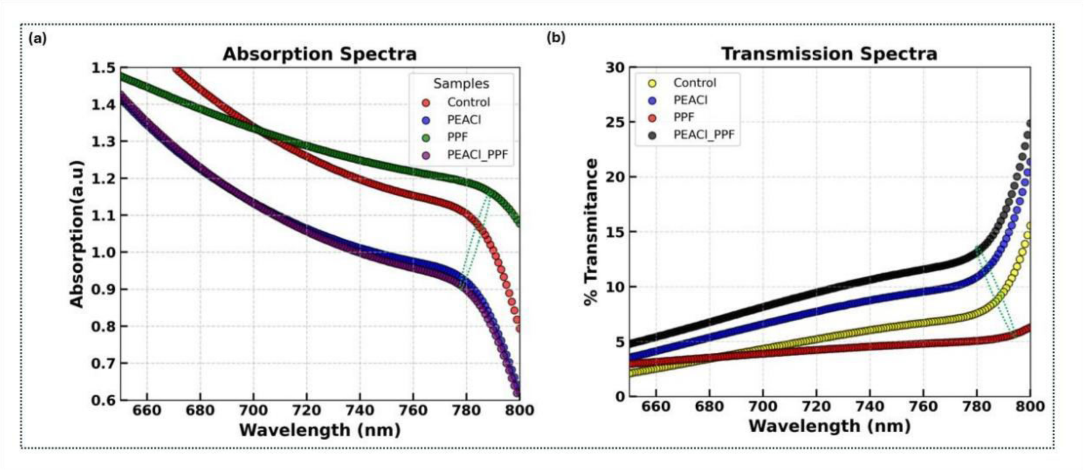

Figure 6.2: (a) Absorption showing absorption and (b) Reflectance spectra ranging between 760nm-790 nm.

In both the absorption and transmission spectra, PEACl/PPF co-passivated films exhibited the lowest absorption and highest transmittance, which indicates the formation of thinner films. In contrast, PPF only films display higher absorption and lower transmission, suggesting greater thickness (Ball, J. M.*et al.*, 2015). The reduced absorption in PEACl/PPF films may be attributed to strong coordination between Pb^{2+} and the oxygen in P-O bonds of PPF, along with Cl^{-} interactions causing strong ionic bonds, leading to a thinner crystal structure (Sun, Q. *et al.*, 2010). This property was crucial for optimizing solar cell performance, where precise control over the thickness of the light-absorbing layer may be essential.

6.2.3 Surface Morphology and Topography Analysis

The surface morphology and topography of the films were analyzed using scanning electron microscopy (SEM) seen in Figure 6.3 (a). All material combinations exhibited a polycrystalline structure ; however, when PPF was used alone, the grain sizes were significantly reduced, which resulted in interwoven crystal formations. Although the crystals were highly compact and dense, the smaller grain sizes negatively impacted the film quality.

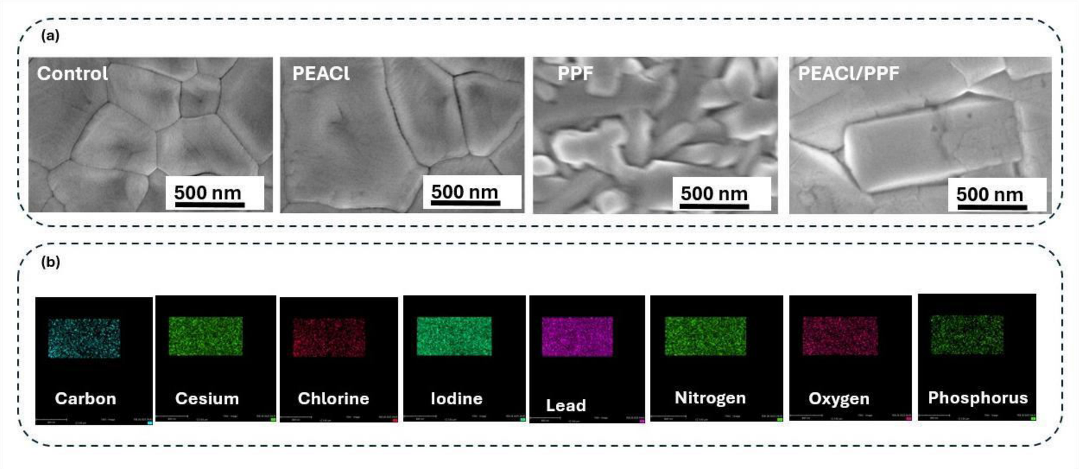

Figure 6.3: (a) Scanning Electron Microscope images showing surface morphology of the films, (b) Energy Dispersive X-ray Spectroscopy (EDS) elemental mapping.

In contrast, the incorporation of PEACl/PPF led to an increased grain size, which was beneficial for enhanced diffusion length and minimized charge recombination (Chen, J., & Park, N. G., 2019). The SEM images also revealed well-defined, sharp, and clean grain boundaries, which indicates fewer defects, improved charge transport, and complete crystallization (Xi, J., Xi, K., Sadhanala, A., Zhang, K. H., Li, G., Dong, H., ... & Wu, Z., 2019).

Additionally, PPF effectively passivated defects and grain boundaries, particularly halide vacancies, which were critical sites for δ-phase nucleation (Gao, Qiaojiao, et al., 2022). There were no voids, pinholes, or cracks observed at the grain boundaries, which prevented moisture ingress and ion migration, thus having an improved material stability.

6.2.4 Energy Dispersive X-ray Spectroscopy (EDS)

To complement the SEM analysis, Energy Dispersive X-ray Spectroscopy (EDS) was employed for elemental composition mapping given in Figure 6.3 (b). The elemental distribution in the PEACl/PPF films included carbon, cesium, chlorine, iodine, nitrogen, lead, oxygen, and phosphorus. However, from the results, the material was predominantly composed of iodine, lead, and nitrogen depicted by their dense coloration while non-intense colour of phosphorus, oxygen, and chlorine depicted the concentration low levels of the elements. In addition, it showed some presence of PEACl and PPF in the films.

The mapping demonstrated a uniform distribution of these elements, confirming the material's homogeneity and even enrichment of both the perovskite and passivating agents. The presence of oxygen ions was particularly noteworthy, as they facilitate coordination with Pb^{2+}, stabilizing the material and preventing its transition back to non-radiative phases (Zhou, W. *et al*., 2024).

However, the EDS results did not outrightly show the potential structure of PEACl, PPF, delta and alpha phases of the perovskite material. Therefore, *ex situ* GIWAXS technique was adopted to explain the morphological intertwines of PEACl/PPF observed from the SEM measurements in Figure 6.3, and low absorption and high transmittance observed in the UV-Vis spectra in Figure 6.2.

6.2.5 Grazing Wide Angle X-ray Scattering (GIWAXS) results

a. Identification of the perovskite (photo-radiative) and non-perovskite (non-radiative).

GIWAXS maps in Figure 6.4(a) showed diffraction patterns collected under a nitrogen-controlled environment. All films exhibited preferential orientation, although residual PbI_2 was detected in the $Cs_{0.1}FA_{0.9}PbI_3$ control sample, as confirmed by the 1D line profiles in Figure 6.4(f). Crystallographic orientation was critical for enhancing charge transport, stability, and overall optoelectronic performance in perovskites (Jiang and Zhang, 2018; Wang *et al*., 2019).

Passivation with PEACl, PPF, and the combined PEACl/PPF yielded highly oriented films, and introduced additional diffraction features. Distinct peaks at $q = 0.5$ Å^{-1} and a new ring at $q = 0.86$ Å^{-1} were observed, corresponding to PEACl and PPF-related phases, respectively (Telschow *et al*., 2023). It was noted that the new ring at $q = 0.86$ Å^{-1} was only observed when PPF was introduced, which did not take the delta notation as observed in chapter 5.

A wide range of small-angle diffraction peaks had been reported for various two-dimensional (2D) perovskite structures, with spacings ranging from d = 57.9 Å ($q = 0.11$ Å^{-1}) for the (001) plane of $PEA_2MAPb_3I_{10}$ to d = 2.88 Å ($q = 2.18$ Å^{-1}) for the (111) plane of $BA_2MAPb_2I_7$ (Qi *et al.* 2022; Stoumpos *et al.* 2016). GIWAXS results (Figure 6.4) for PEACl-$Cs_{0.1}FA_{0.9}PbI_3$ reveal a (001) diffraction ring at $q = 0.3$ Å^{-1}, consistent with the formation of n = 1 Ruddlesden–Popper phases. Upon co-passivation with 0.03 wt% PEACl and 0.02 g/mol PPF, a new diffraction feature emerges at $q = 0.86$ Å^{-1} (Figure 6.4c), a behavior also observed in films passivated solely with PPF (Figure 6.4b).

Increasing the PEACl concentration to 1.5 wt% results in the appearance of additional diffraction peaks (Appendix 12).

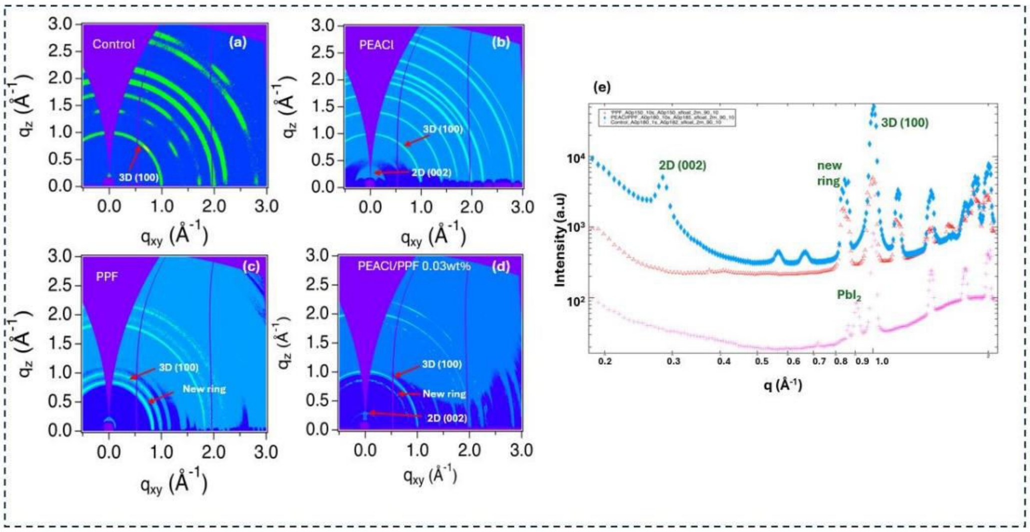

Figure 6.4: GIWAXS patterns of (a) $Cs_{0.1}FA_{0.9}PbI_3$ (b) PEACl-$Cs_{0.1}FA_{0.9}PbI_3$ (c) PPF-$Cs_{0.1}FA_{0.9}PbI_3$, and (d) 0.03wt%PEACl/0.02g/molPPF-$Cs_{0.1}FA_{0.9}PbI_3$ films (e) 1D line-cuts graphs that clearly give the peaks from maps.

At mid-q values (approximately 1.0 Å^{-1}), a strong diffraction ring was observed, corresponding to the (100) reflection of the 3D-like perovskite phase (α-$Cs_{0.1}FA_{0.9}PbI_3$). In the high-*q* region (~2.0 Å^{-1} and above), broader and more diffuse features were present, associated with higher-order reflections like (200) planes and structural disorder as observed in other findings, (Tan, W. L., Cheng, Y. B., & McNeill, C. R., 2020). Table 6.1 shows the phase associated with *q*-ranges and assigned miller indices, while Appendix 6 gives a detailed cubic calculation obtained for cubic $Cs_{0.1}FA_{0.9}PbI_3$ using the discussion from section 2.5.5

Table 6.1: Indexed Diffraction Peaks for PEACl/PPF Passivated $Cs_{0.1}FA_{0.9}PbI_3$ Perovskites.

q (Å^{-1}) Range	Likely Phase	Assignment
0.2–0.5	2D perovskite (PEACl phases)	(00l) stacking (n = 1, 2, 3...)
~1.0	3D perovskite (α-$Cs_{0.1}FA_{0.9}PbI_3$)	(100) reflection
~2.0	3D perovskite (α-$Cs_{0.1}FA_{0.9}PbI_3$)	(200) reflection

b. Defect Passivation and Ion Migration discussion

Controlling ion migration and passivating defects were essential to enhance the stability and optoelectronic performance of $Cs_{0.1}FA_{0.9}PbI_3$ perovskite films. GIWAXS measurements revealed that passivation with PEACl, PPF, and their combination induced highly oriented crystal growth, suppressed residual PbI_2, and introduced new diffraction features linked to improved lattice ordering as mentioned by Kodalle, T., *et al*. (Kodalle, T. *et al*., 2024). These structural modifications correlate with reduced in defect densities and non-radiative recombination pathways, underscoring the critical role of crystallographic alignment and surface passivation in mitigating ionic motion and enhancing radiative efficiency.

Formation of a mixed-phase architecture that consisted of surface 2D perovskite layers templated by PEACl and a bulk 3D-like perovskite phase were beneficial for enhanced stability. 2D phases efficiently passivated surface and grain boundary defects, while the 3D interior supported efficient charge transport.

Additionally, the incorporation of PPF, a bulky phosphine oxide derivative, provided effective surface passivation. Phosphine oxide groups were well-known for coordinating under-coordinated Pb^{2+} ions, that lead to defect passivation and improved optoelectronic properties (Luo *et al.*, 2023). Upon PPF passivation, PbI_2-related peaks were suppressed (Figure 6.4c), crystallinity enhanced (sharper perovskite diffraction peaks), and the emergence of a new diffraction ring at $q = 0.86$ Å^{-1} was observed. These structural changes correlated with decreased photoluminescence (PL) emission for PPF in Figure 6.1(b) and morphological changes in SEM images in Figure 6.3(b). Optimizing the balance between PEACl and PPF co-passivation is recommended to maximize device performance.

6.3 Chapter summary

The synergistic passivation strategies using PEACl and PPF significantly improve the structural, optical, and electronic properties of $Cs_{0.1}FA_{0.9}PbI_3$ perovskite films. Comprehensive characterization using PL, absorption/transmission spectroscopy, SEM, and EDS, confirmed that co-passivation promoted highly oriented crystal growth, reduced defect densities, and suppresses ion migration pathways. GIWAXS analyses revealed the formation of mixed 2D/3D phase architectures, with enhanced crystallinity and preferential alignment along the c-axis, effectively mitigated non-radiative recombination losses.

CHAPTER SEVEN

CONCLUSION AND SUGGESTIONS FOR FURTHER RESEARCH

Perovskite research remains a vibrant and fast-evolving field, with projections suggesting that perovskite solar cell efficiencies could soon reach around 40%, particularly with tandem architectures. Beyond photovoltaics, perovskites have shown great promise in applications such as field-effect transistors, photo-diodes, quantum dots among others.

The humidity had a significant impact on crystallization of perovskites; in particular, 3-CAT exhibited phase breakdown into hexagonal and PbI_2 phases at RH levels exceeding 100%, as evidenced by the appearance of peaks at q = 0.83 and q = 0.9 $Å^{-1}$. AFM analysis showed that EA produced smoother films, while CB, despite generating additional peaks, demonstrated promise due to its ability to minimize pinhole formation. SEM imaging indicated that 3-CAT formed smaller grains, likely due to a slower transition from the hexagonal to the cubic phase.

The interaction between PEACl and PPF played a key role in stabilizing precursor ions and intermediate phases by forming a passivation layer that reduced defects and restrained rapid crystallization. Through *in situ* observation, co-passivation was found to delay crystallization due to increased precursor density and effectively bypass the defect-prone δ-phase, resulting in enhanced phase stability. These passivating agents also influenced grain orientation and size distribution, enabling direct formation of the thermodynamically stable α-phase.

The combined effect of PEACl and PPF enhanced optoelectronic performance and scalability by producing uniform, defect-free films with strong structural integrity. Detailed characterization using PL, absorption/transmission spectroscopy, SEM, and EDS confirmed that co-passivation encouraged well-aligned crystal growth, lowered defect density, and limited ion migration. GIWAXS analysis further revealed the presence of mixed 2D/3D phase structures with improved crystallinity and c-axis alignment, effectively reducing non-radiative recombination losses.

Recommendations for further Research

The crystallization behavior of 3-CAT remains intricate and warranted further investigation through GIWAXS, especially concerning anti-solvent techniques such as carrier-gas-free spraying, optimizing annealing window and anti-solvent dropping protocols, which could improve film orientation and quality under controlled humidity and inert conditions.

Emerging strategies such as synergistic molecular passivation - combining PEACl and PPF - markedly improved film stability (tested to extend the double cation perovskite stability beyond 4008 hours (Appendix 7)), grain orientation, and optoelectronic performance. An optimized combined effect of the co-passivants is needed to enhance optoelectronic performance - especially film thickness to enhance absorption - and scalability by producing uniform, defect-free films with strong structural integrity.

REFERENCES

Abbas, H. A., Kottokkaran, R., Ganapathy, B., Samiee, M., Zhang, L., Kitahara, A., ... & Dalal, V. L. (**2015**). High efficiency sequentially vapor grown nip CH3NH3PbI3 perovskite solar cells with undoped P3HT as p-type heterojunction layer. *APL materials*, *3*(1).

Advanced Light Source (ALS). (**2025**].). *Beamline 7.3.3 – SAXS/WAXS*. Lawrence Berkeley National Laboratory. retrieved [24th March, **2025**] https://als.lbl.gov/beamlines/7-3-3/

Afzal, U. (**2024**). A Comprehensive Tutorial on Graphene Family X-ray Diffraction Analysis: Graphical Representation of Miller Indices. *Siazga Research Journal*, *3*(2), 96-105.

Aguiar, J. A., Wozny, S., Holesinger, T. G., Aoki, T., Patel, M. K., Yang, M., ... & Zhu, K. (**2016**). *In situ* investigation of the formation and metastability of formamidinium lead tri- iodide perovskite solar cells. *Energy & Environmental Science*, *9*(7), 2372-2382.

Aguilar-Marín, P., Angelats-Silva, L., Noriega-Diaz, E., Chavez-Bacilio, M., & Verde-Vera, R. (**2020**). Understanding the phenomenon of x-ray diffraction by crystals and related concepts. *European Journal of Physics*, *41*(4), 045501.

Aiba, M. (**2018, June**). Review of top-up injection schemes for Electron Storage Rings. In *Proc. 9th Int. Particle Accelerator Conf.(IPAC'18)* (pp. 1745-1750).

Aïssa, B., Ali, A., & El-Mellouhi, F. (2021). Oxide and organic–inorganic halide perovskites with plasmonics for optoelectronic and energy applications: a contributive review. *Catalysts*, *11*(9), 1057.

Alanazi, T. I. (2023). Current spray-coating approaches to manufacture perovskite solar cells. *Results in Physics*, *44*, 106144.

Alford, T. L., Feldman, L. C., & Mayer, J. W. (**2007**). X-ray Diffraction. *Fundamentals of Nanoscale Film Analysis*, 129-151.

Ali, A., Chiang, Y. W., & Santos, R. M. (**2022**). X-ray diffraction techniques for mineral characterization: A review for engineers of the fundamentals, applications, and research directions. *Minerals*, *12*(2), 205.

Als-Nielsen, J., & McMorrow, D. (**2011**). *Elements of modern X-ray physics*. John Wiley & Sons.

Ameh, E. S. (**2019**). A review of basic crystallography and x-ray diffraction applications. *The international journal of advanced manufacturing technology*, *105*(7), 3289-3302.

Aristidou, N., Sanchez-Molina, I., Chotchuangchutchaval, T., Brown, M., Martinez, L., Rath, T., & Haque, S. A. (**2015**). The role of oxygen in the degradation of methylammonium lead trihalide perovskite photoactive layers. *Angewandte Chemie*, *127*(28), 8326-8330.

Aspinall, R. J., Marcus, W. A., & Boardman, J. W. (**2002**). Considerations in collecting, processing, and analysing high spatial resolution hyperspectral data for environmental investigations. *Journal of Geographical Systems*, *4*, 15-29.

Awino, C., Barasa, G., & Odari, V. (**2020**). Light induced degradation of the transport length of $CH_3NH_3PbI_3$ studied by modulated surface photovoltage spectroscopy after Goodman. *Organic Electronics*, *77*, 105503.

Ball, J. M., Stranks, S. D., Hörantner, M. T., Hüttner, S., Zhang, W., Crossland, E. J., ... & Snaith, H. J. (2015). Optical properties and limiting photocurrent of thin-film perovskite solar cells. *Energy & Environmental Science*, *8*(2), 602-609.

Bakar, A., Alrashdi, A. O., Fadhali, M. M., Afaq, A., Yakout, H. A., & Asif, M. (**2022**). Effect of pressure on structural, elastic and mechanical properties of cubic perovskites $XCoO_3$ (X= Nd, Pr) from first-principles investigations. *Journal of Materials Research and Technology*, *19*, 4233-4241.

Barkla, C. G. (**1905**). XIII. Polarised röntgen radiation. *Philosophical Transactions of the Royal Society of London. Series A, Containing Papers of a Mathematical or Physical Character*, *204*(372-386), 467-479.

Barrows, A. T., Lilliu, S., Pearson, A. J., Babonneau, D., Dunbar, A. D., & Lidzey, D. G. (**2016**). Monitoring the Formation of a $CH_3NH_3PbI_{3-x}Cl_x$ Perovskite during Thermal Annealing Using X-Ray Scattering. *Advanced Functional Materials*, *26*(27), 4934-4942.

Bartel, C. J., Millican, S. L., Deml, A. M., Rumptz, J. R., Tumas, W., Weimer, A. W., ... & Holder, A. M. (**2018**). Physical descriptor for the Gibbs energy of inorganic crystalline solids and temperature-dependent materials chemistry. *Nature communications*, *9*(1), 4168.

Barua, P., & Hwang, I. (**2023**). Bulk perovskite crystal properties determined by heterogeneous nucleation and growth. *Materials*, *16*(5), 2110.

Basumatary, P., Kumari, J., & Agarwal, P. (**2022**). Probing the defects states in $MAPbI_3$ perovskite thin films through photoluminescence and photoluminescence excitation spectroscopy studies. *Optik*, *266*, 169586.

Bharambe, C. A., Ravankar, A., Kathale, N., & Verulkar, N. M. (**2016**) Silicon Photonics–A Review Paper. *Journal of Electronic Design Engineering*, *2*(3).

Bilderback, D. H., Elleaume, P., & Weckert, E. (**2005**). Review of third and next generation synchrotron light sources. *Journal of Physics B: Atomic, molecular and optical physics*, *38*(9), S773.

Bosch, R. A., May, T. E., Reininger, R., & Green, M. A. (**1996**). Infrared radiation from bending magnet edges in an electron storage ring. *Review of Scientific Instruments*, *67*(9), 3346-3346.

Bragg, W. H., & Bragg, W. L. (**1915**). *X rays and crystal structure*. Bell.

Bragg, W. H., & Bragg, W. L. (**1913**). The reflection of X-rays by crystals. *Proceedings of the Royal Society of London. Series A, Containing Papers of a Mathematical and Physical Character*, *88*(605), 428-438.Buin, A., Comin, R., Xu, J., Ip, A. H., & Sargent, E. H. (**2015**). Halide-dependent electronic structure of organolead perovskite materials. *Chemistry of Materials*, *27*(12), 4405-4412.

Burlakov, V. M., Eperon, G. E., Snaith, H. J., Chapman, S. J., & Goriely, A. (**2014**). Controlling coverage of solution cast materials with unfavourable surface interactions. F*Applied Physics Letters*, *104*(9).

Burwig, T. (**2023**). *Growth and thermal decomposition of metal-halide perovskite thin films analyzed by in situ X-ray diffraction* (Doctoral dissertation, Dissertation, Halle (Saale), Martin-Luther-Universität Halle-Wittenberg, 2023).

Busch, U. (**2023**). Claims of priority–The scientific path to the discovery of X-rays. *Zeitschrift für Medizinische Physik*, *33*(2), 230-242.

Canon. (**2025**). *Synchrotron radiation*. Canon Science Lab. retrieved [24th March, **2025**] https://global.canon/en/technology/s_labo/light/004/02.html

Cao, M., Zhang, K., Zhang, S., Wang, Y., & Chen, C. (**2022**). Advanced light source analytical techniques for exploring the biological behavior and fate of nanomedicines. *ACS Central Science*, *8*(8), 1063-1080.

Castelli, I. E., Thygesen, K. S., & Jacobsen, K. W. (2015). Calculated optical absorption of different perovskite phases. *Journal of Materials Chemistry A*, *3*(23), 12343-12349.

Carini, G., Denes, P., Gruener, S., & Lessner, E. (**2012**). *Neutron and X-ray detectors*. USDOE Office of Science (SC)(United States).

Chang, C. Y., Huang, Y. C., Tsao, C. S., & Su, W. F. (**2016**). Formation mechanism and control of perovskite films from solution to crystalline phase studied by *in situ* synchrotron scattering. *ACS applied materials & interfaces*, *8*(40), 26712-26721.

Cheng, P., Wang, P., Xu, Z., Jia, X., Wei, Q., Yuan, N., ... & Liu, S. F. (**2019**). Ligand-size related dimensionality control in metal halide perovskites. *ACS Energy Letters*, *4*(8), 1830-1838.

Chen, J., & Park, N. G. (2019). Causes and solutions of recombination in perovskite solar cells. *Advanced Materials*, *31*(47), 1803019.

Chen, Q., De Marco, N., Yang, Y. M., Song, T. B., Chen, C. C., Zhao, H., ... & Yang, Y. (**2015**). Under the spotlight: The organic–inorganic hybrid halide perovskite for optoelectronic applications. *Nano Today*, *10*(3), 355-396.

Cho, N., Li, F., Turedi, B., Sinatra, L., Sarmah, S. P., Parida, M. R., & Bakr, O. M. (**2016**). Pure crystal orientation and anisotropic charge transport in large-area hybrid perovskite films. *Nature communications*, *7*(1), 13407.

Clark, G. L. (**1927**). *Applied X-rays*. McGraw-Hill book Company, Incorporated.

Clegg, W. (**2019**). The development and exploitation of synchrotron single-crystal diffraction for chemistry and materials. *Philosophical Transactions of the Royal Society A*, *377*(2147), 20180239.

Coffey, A. H., Yang, S. J., Gómez, M., Finkenauer, B. P., Terlier, T., Zhu, C., & Dou, L. (**2023**). Controlling Crystallization of Quasi-2D Perovskite Solar Cells: Incorporating Bulky Conjugated Ligands. *Advanced Energy Materials*, *13*(33), 2201501.

Coffey, A. H., Slack, J., Cornell, E., Yang, L. L., Anderson, K., Wang, K., ... & Zhu, C. (**2023**). *In situ* spin coater for multimodal grazing incidence x-ray scattering studies. *Review of Scientific Instruments*, *94*(9).

Cohen, T. A. (2022). *Design, Development, and Processing of Perovskite Nanocrystals for Optical Devices*. University of Washington.

Contreras-Torres, F. F. (**2019**). IndexCub: a ready-to-use set of routines for X-ray diffraction line profile analysis. *Powder Diffraction*, *34*(2), 110-118.

Cooper, M., Mijnarends, P., Shiotani, N., Sakai, N., & Bansil, A. (**2004**). *X-ray Compton scattering* (Vol. 5). OUP Oxford.

Cramer, S. P. (**2020**). X-ray spectroscopy with synchrotron radiation. *Biological and Medical Physics, Biomedical Engineering*.

Danby, G. T., Addessi, L., Armoza, Z., Benante, J., Brown, H. N., Bunce, G., ... & Redin, S. I. (**2001**). The Brookhaven muon storage ring magnet. *Nuclear Instruments and Methods in Physics Research Section A: Accelerators, Spectrometers, Detectors and Associated Equipment*, *457*(1-2), 151-174.

Davidovich, R. L., Stavila, V., Marinin, D. V., Voit, E. I., & Whitmire, K. H. (**2009**). Stereochemistry of lead (II) complexes with oxygen donor ligands. *Coordination Chemistry Reviews*, *253*(9-10), 1316-1352.

DEJOIE, C., MARTINETTO, P., & TAMURA, N. (**2024**). Introduction to Synchrotron Radiation: Application to the Study of Cultural Heritage Materials and Biominerals. *Synchrotron Radiation, Cultural Heritage, Biomineralization*, 1-16.

Deutsches Elektronen-Synchrotron (DESY). (**2025**). *How does a synchrotron radiation source work?* Photon Science DESY. Retrieved [24th March, **2025**], https://photonscience.desy.de/research/students__teaching/primers/synchrotron_radiation/index_eng.html

De Wolf, S., Holovsky, J., Moon, S., Löper, P., Niesen, B., Ledinsky, M., Ballif, C. (**2014**). *Organometallic Halide Perovskites: Sharp Optical Absorption Edge and Its Relation to Photovoltaic Performance.* Phys. Chem. Lett.

Dibner, B. (**1968**). *Wilhelm Conrad Ro˜ ntgen and the Discovery of X Rays*. F. Watts.

Di, K., Guo, R., Wang, Y., Lv, Y., Su, H., Zhang, Q., ... & Wang, L. (**2023**). Achieving high-performance narrowband blue MR-TADF emitters by suppressing isomer formation and extending π-conjugate skeletons. *Journal of Materials Chemistry C*, *11*(19), 6429-6437.

Dittrich, T., Awino, C., Prajongtat, P., Rech, B., & Lux-Steiner, M. C. (**2015**). Temperature dependence of the band gap of CH3NH3PbI3 stabilized with PMMA: a modulated surface photovoltage study. *The Journal of Physical Chemistry C*, *119*(42), 23968-23972.

Docampo, P., Ball, J. M., Darwich, M., Eperon, G. E., & Snaith, H. J. (**2013**). Efficient organometal trihalide perovskite planar-heterojunction solar cells on flexible polymer substrates. *Nature communications*, *4*(1), 2761.

Dudley M. (**2023**) https://you.stonybrook.edu/xraycharacterization/techniques/

Duarte, V. C., & Andrade, L. (2024). Recent Advancements on Slot-Die Coating of Perovskite Solar Cells: The Lab-to-Fab Optimisation Process. *Energies*, *17*(16), 3896.

Elleaume, P. (**1990**). Theory of undulators and wigglers.

Enzheng S., Yao G., Blake P. Finkenauer, Akriti, Aidan H. C. and Dou L., (**2018)**, Two-dimensional halide perovskite nanomaterials and heterostructures, ***Chem. Soc. Rev.,*** , 47, 6046, DOI: 10.1039/c7cs00886d, rsc.li/chem-soc-rev

Eperon, G. E., Habisreutinger, S. N., Leijtens, T., Bruijnaers, B. J., van Franeker, J. J., DeQuilettes, D. W., & Snaith, H. J. (**2015**). The importance of moisture in hybrid lead halide perovskite thin film fabrication. *ACS nano*, *9*(9), 9380-9393.

Erdemir, D., Lee, A. Y., & Myerson, A. S. (**2009**). Nucleation of crystals from solution: classical and two-step models. *Accounts of chemical research*, *42*(5), 621-629.

European Organization for Nuclear Research (CERN). (**2025**). *Undulators and wigglers* [Presentation slides].Indico. retrieved [24th March, **2025**] https://indico.cern.ch/event/668489/contributions/2733481/attachments/1562549/2460719/Lecture2Undulatorsandwigglers.pdf

Fan, C., & Zhao, Z. (Eds.). (2018). *Synchrotron radiation in materials science: light sources, techniques, and applications*. John Wiley & Sons.

Fan, Z., Sun, K., & Wang, J. (2015). Perovskites for photovoltaics: a combined review of organic–inorganic halide perovskites and ferroelectric oxide perovskites. *Journal of Materials Chemistry A*, *3*(37), 18809-18828.

Fenner, E. (**2014**). Smashing Atoms and Expectations.

Fenter, P. A., Rivers, M. L., Sturchio, N., & Sutton, S. R. (Eds.). (**2018**). *Applications of synchrotron radiation in low-temperature geochemistry and environmental science* (Vol. 49). Walter de Gruyter GmbH & Co KG.

Ferdowsi, P., Steiner, U., & Milić, J. V. (**2021**). Host-guest complexation in hybrid perovskite optoelectronics. *Journal of Physics: Materials*, *4*(4), 042011.

Fonseca, M. D. C., Araujo, B. H. S., Dias, C. S. B., Archilha, N. L., Neto, D. P. A., Cavalheiro, E., & Franchini, K. G. (**2018**). High-resolution synchrotron-based X-ray microtomography as a tool to unveil the three-dimensional neuronal architecture of the brain. *Scientific Reports*, *8*(1), 12074.

Frost, J. M., Butler, K. T., Brivio, F., Hendon, C. H., Van Schilfgaarde, M., & Walsh, A. (**2014**). Atomistic origins of high-performance in hybrid halide perovskite solar cells. *Nano letters*, *14*(5), 2584-2590.

Fthenakis, V., & Zweibel, K. (**2003**). *CdTe PV: Real and perceived EHS risks* (No. NREL/CP-520-33561). National Renewable Energy Lab.(NREL), Golden, CO (United States).

Fultz, B., & Howe, J. M. (**2012**). *Transmission electron microscopy and diffractometry of materials*. Springer Science & Business Media.

G2V Optics. (n.d.). *How are perovskite solar cells made?* G2V Optics Inc. Retrieved May 20, 2025, from https://g2voptics.com/perovskite-solar-cells/how-are-perovskite-solar-cellsmade/#:~:text=Spin%2DCoating:%20Benefits%20And%20Drawbacks,of%20small%20samples%20in%20labs.

Gao, Q., Qi, J., Chen, K., Xia, M., Hu, Y., Mei, A., & Han, H. (**2022**). Halide perovskite crystallization processes and methods in nanocrystals, single crystals, and thin films. *Advanced Materials*, *34*(52), 2200720.

Gao, W., Ding, J., Ma, Q., Zhang, H., Zhang, J., Zhang, Z., & Chen, C. (**2025**). Synergistic Modulation of Orientation and Steric Hindrance Induced by Alkyl Chain Length in Ammonium Salt Passivator Toward High-performance Inverted Perovskite Solar Cells and Modules. *Advanced Materials*, *37*(1), 2413304.

Ghosh, S., & Manna, L. (**2018**). The many "facets" of halide ions in the chemistry of colloidal inorganic nanocrystals. *Chemical reviews*, *118*(16), 7804-7864.

Godwin, R. P. (1969). *Synchrotron radiation as a light source* (pp. 1-73). Springer Berlin Heidelberg.

Gonzalez-Pedro, V., Juarez-Perez, E. J., Arsyad, W. S., Barea, E. M., Fabregat-Santiago, F., Mora-Sero, I., & Bisquert, J. (**2014**). General working principles of CH3NH3PbX3 perovskite solar cells. *Nano letters*, *14*(2), 888-893.

Grabowski, M., Cooper, D. R., Brzezinski, D., Macnar, J. M., Shabalin, I. G., Cymborowski, M., ... & Minor, W. (**2021**). Synchrotron radiation as a tool for macromolecular X-Ray Crystallography: A XXI century perspective. *Nuclear Instruments and Methods in Physics Research Section B: Beam Interactions with Materials and Atoms*, *489*, 30-40.

Greaves, A. W. (**2011**). *Phase contrast in x-ray imaging* (Doctoral dissertation, Swinburne).

Green, M. A., Ho-Baillie, A., & Snaith, H. J. (**2014)**. The emergence of perovskite solar cells. *Nature photonics*, *8*(7), 506-514.

Guo, Y., Shoyama, K., Sato, W., Matsuo, Y., Inoue, K., Harano, K., & Nakamura, E. (**2015)**. Chemical pathways connecting lead (II) iodide and perovskite via polymeric plumbate (II) fiber. *Journal of the American Chemical Society*, *137*(50), 15907-15914.

Habs, D., & Köster, U. (**2011**). Production of medical radioisotopes with high specific activity in photonuclear reactions with γ-beams of high intensity and large brilliance. *Applied Physics B*, *103*, 501-519.

Harvey, M. J., Mason, N. J., McLean, A., & Rzepa, H. S. (**2015**). Standards-based metadata procedures for retrieving data for display or mining utilizing Persistent (data-DOI) Identifiers. *Journal of Cheminformatics*, *7*, 1-10.

Hasan, S. G. A., Gupta, A. V., & Reddi, B. V. (**2021**). Estimation of size and lattice parameter of magnetic nanoparticles based on XRD synthesized using arc-discharge technique. *Materials Today: Proceedings*, *47*, 4137-4141.

He, D., Li, R., Liu, B., Zhou, Q., Yang, H., Yu, X., & Chen, J. (**2023**). Unraveling abnormal buried interface anion defect passivation mechanisms depending on cation-induced steric hindrance for efficient and stable perovskite solar cells. *Journal of Energy Chemistry*, *80*, 1-9.

Hendon, C. H., Yang, R. X., Burton, L. A., & Walsh, A. (**2015**). Assessment of polyanion (BF^{4-} and PF^{6-}) substitutions in hybrid halide perovskites. *Journal of Materials Chemistry A*, *3*(17), 9067-9070.

Hiden Analytical. (**2025**). *Synchrotron materials science | Light*. Retrieved [24th March, **2025**], from https://www.hidenanalytical.com/applications/fusion-high-energy-physics/synchrotron-materials-science/

Highest Efficiency Perovskite Solar Cells | Ossila, https://www.ossila.com/pages/highest-efficiency-perovskite-solar-cells.

History.com Editors. (**2025**). *German scientist discovers X-rays*. History. Retrieved [23rd March, 2025], from https://www.history.com/this-day-in-history/November-8/german-scientist-discovers-x-rays

Huang, H. H., Ma, Z., Strzalka, J., Ren, Y., Lin, K. F., Wang, L., ... & Chen, W. (**2021**). Mild water intake orients crystal formation imparting high tolerance on unencapsulated halide perovskite solar cells. *Cell Reports Physical Science*, *2*(4).

Hu, L., Liu, K. Q., Li, F., Li, H. Y., Wang, W., Fang, H. L., ... & Wang, Z. X. (2024). Water-ultrastable perovskite $CsPbBr_3$ nanocrystals tailored by surface-confined strategy for amaranth sensing in food samples. *Food Chemistry*, *434*, 137532.

Hu, M., Bi, C., Yuan, Y., Bai, Y., & Huang, J. (2015). Stabilized wide bandgap $MAPbBr_xI_{3-x}$ perovskite by enhanced grain size and improved crystallinity. *Advanced Science*, *3*(6), 1500301.

Hu, R., Zhang, Y., Paek, S., Gao, X. X., Li, X. A., & Nazeeruddin, M. K. (2020). Enhanced stability of α-phase $FAPbI_3$ perovskite solar cells by insertion of 2D (PEA) $_2PbI_4$ nanosheets.

Hu, S., Trinchi, A., Atkin, P., & Cole, I. (**2015**). Tunable photoluminescence across the entire visible spectrum from carbon dots excited by white light. *Angewandte Chemie International Edition*, *54*(10), 2970-2974.

Huxley, H. E., Faruqi, A. R., Bordas, J., Koch, M. H. J., & Milch, J. R. (**1980**). The use of synchrotron radiation in time-resolved X-ray diffraction studies of myosin layer-line reflections during muscle contraction. *Nature*, *284*(5752), 140-143.

Hwang, C. S., Jan, J. C., Chang, C. S., Chen, S. D., Chang, C. H., & Uen, T. M. (**2011**). Development trends for insertion devices of future synchrotron light sources. *Physical Review Special Topics—Accelerators and Beams*, *14*(4), 044801.

Ibrahim, Shoukat, A., Aslam, F., & Israr Ur Rehman, M. (2024). Emerging trends in low band gap perovskite solar cells: materials, device architectures, and performance optimization. *Molecular Physics*, *122*(17), e2316273.

Ice, G. E., & Pang, J. W. (**2009**). Tutorial on x-ray microLaue diffraction. *Materials Characterization*, *60*(11), 1191-1201.

Jain, A., Ong, S. P., Hautier, G., Chen, W., Richards, W. D., Dacek, S., ... & Persson, K. A. (**2013**). Commentary: The Materials Project: A materials genome approach to accelerating materials innovation. *APL materials*, *1*(1).

Jean, J., Brown, P. R., Jaffe, R. L., Buonassisi, T., & Bulović, V. (**2015**). Pathways for solar photovoltaics. *Energy & Environmental Science*, *8*(4), 1200-1219.

Jenkin, J. (**2008**). *William and Lawrence Bragg, father and son: the most extraordinary collaboration in science*. Oxford University Press, USA.

Jeon, N. J., Noh, J. H., Kim, Y. C., Yang, W. S., Ryu, S., & Seok, S. I. (**2014**). Solvent engineering for high-performance inorganic–organic hybrid perovskite solar cells. *Nature materials*, *13*(9), 897-903.

Jiang, C., & Zhang, P. (**2018**). Crystalline orientation dependent photoresponse and heterogeneous behaviors of grain boundaries in perovskite solar cells. *Journal of Applied Physics*, *123*(8).

Jiao, Y., Yi, S., Wang, H., Li, B., Hao, W., Pan, L., & Lu, J. (**2021**). Strain engineering of metal halide perovskites on coupling anisotropic behaviors. *Advanced Functional Materials*, *31*(4), 2006243.

Jungjohann, K., & Carter, C. B. (**2016**). *In situ* and operando. *Transmission electron microscopy: diffraction, imaging, and spectrometry*, 17-80.

Kazmerski, L., Gwinner, D., & Hicks, A. (**2010**). Best research cell efficiencies. *National Renewable Energy Laboratory*, *2*, 0-0.

Kawaguchi, S., Takemoto, M., Osaka, K., Nishibori, E., Moriyoshi, C., Kubota, Y., & Sugimoto, K. (**2017**). High-throughput powder diffraction measurement system consisting of multiple MYTHEN detectors at beamline BL02B2 of SPring-8. *Review of scientific instruments*, *88*(8).

Kawamura, Y., Mashiyama, H., & Hasebe, K. (**2002**). Structural study on cubic-tetragonal transition of $CH_3NH_3PbI_3$. *Journal of the Physical Society of Japan*, *71*(7), 1694-1697.

Kegelmann, L., Wolff, C. M., Awino, C., Lang, F., Unger, E. L., Korte, L., ... & Albrecht, S. (**2017**). It Takes Two to Tango Double-Layer Selective Contacts in Perovskite Solar Cells for Improved Device Performance and Reduced Hysteresis. *ACS applied materials &interfaces*, *9*(20), 17245-17255.

Kennard, R. M., Dahlman, C. J., Chung, J., Cotts, B. L., Mikhailovsky, A. A., Mao, L., ... & Chabinyc, M. L. (2021). Growth-controlled broad emission in phase-pure two-dimensional hybrid perovskite films. *Chemistry of Materials*, *33*(18), 7290-7300.

Kilner, J. A., Skinner, S. J., Irvine, S. J., & Edwards, P. P. (Eds.). (**2012**). *Functional materials for sustainable energy applications*. Elsevier.

Kim, S. Y., Kumachang, C. C., & Doumon, N. Y. (**2023**). Characterization tools to probe degradation mechanisms in organic and perovskite solar cells. *Solar RRL*, *7*(13), 2300155.

Kodalle, T., Byranvand, M.M., Goudreau, M., Das, C., Roy, R., Kot, M., Briesenick, S., Zohdi, M., Rai, M., Tamura, N. and Flege, J.I., (**2024)**. An Integrated Deposition and Passivation Strategy for Controlled Crystallization of 2D/3D Halide Perovskite Films. *Advanced Materials*, p.2309154.

Kodur, M., Kumar, R. E., Luo, Y., Cakan, D. N., Li, X., Stuckelberger, M., & Fenning, D. P. (**2020**). X-Ray microscopy of halide perovskites: techniques, applications, and prospects. *Advanced Energy Materials*, *10*(26), 1903170.

Kong, W., Ye, Z., Qi, Z., Zhang, B., Wang, M., Rahimi-Iman, A., & Wu, H. (**2015**). Characterization of an abnormal photoluminescence behavior upon crystal-phase transition of perovskite $CH_3NH_3PbI_3$. *Physical Chemistry Chemical Physics*, *17*(25), 16405-16411.

Korsunsky, A. M., Hofmann, F., Abbey, B., Song, X., Belnoue, J. P., Mocuta, C., & Dolbnya, I. (**2012**). Analysis of the internal structure and lattice (mis) orientation in individual grains of deformed CP nickel polycrystals by synchrotron X-ray micro-diffraction and microscopy. *International journal of fatigue*, *42*, 1-13.

Kudilatt, H., Hou, B., & Welland, M. E. (**2020**). Quantum dots microstructural metrology: from time-resolved spectroscopy to spatially resolved electron microscopy. *Particle & Particle Systems Characterization*, *37*(12), 2000192.

Kutsaev, S. V. (**2021**). Electron bunchers for industrial RF linear accelerators: theory and design guide. *The European Physical Journal Plus*, *136*(4), 446.

Larruquert, J. I. (2018). Optical properties of thin film materials at short wavelengths. In *Optical Thin Films and Coatings* (pp. 291-356). Woodhead Publishing.

Laurence, C., Graton, J., & Gal, J. F. (**2011**). An overview of Lewis basicity and affinity scales. *Journal of Chemical Education*, *88*(12), 1651-1657.

Lawson, J. D. (**1997**). Early synchrotrons in Britain, and early work for CERN.

Levichev, E., & Vinokurov, N. (**2010**). Undulators and other insertion devices. *Reviews of Accelerator Science and Technology*, *3*(01), 203-220.

Li, B., Binks, D., Cao, G., & Tian, J. (**2019**). Engineering halide perovskite crystals through precursor chemistry. *Small*, *15*(47), 1903613.

Li, C., Lu, X., Ding, W., Feng, L., Gao, Y., & Guo, Z. (**2008**). Formability of abx3 (x= f, cl, br, i) halide perovskites. *Acta Crystallographica Section B: Structural Science*, *64*(6), 702-707.

Li, F., Liu, R., Li, W., Xie, M., & Qin, S. (**2024**). Synchrotron radiation: A key tool for drug discovery. *Bioorganic & Medicinal Chemistry Letters*, 129990.

Lightsources.org. (2025). *Lightsources.org*. Retrieved May 18, 2025, from https://lightsources.org/

Lin, Y. K., Chen, C. H., Wang, Y. Y., Yu, M. H., Yang, J. W., Ni, I. C., ... & Chueh, C. C. (**2023**). Realizing High Brightness Quasi-2D Perovskite Light-Emitting Diodes with Reduced Efficiency Roll-Off via Multifunctional Interface Engineering. *Advanced Science*, *10*(26), 2302232.

Li, Q. (2024). Atomistic Insight into the Chemical Instability of Metal Halide Perovskites from First Principles.

Liu, F., Zhang, Y., Ding, C., Kobayashi, S., Izuishi, T., Nakazawa, N., ... & Shen, Q. (2017). Highly luminescent phase-stable CsPbI3 perovskite quantum dots achieving near 100% absolute photoluminescence quantum yield. *ACS nano*, *11*(10), 10373-10383.

Liu, J. (**2019**), *Local structure of lead halide perovskites for photovoltaic applications* (Doctoral dissertation, Queen Mary University of London).

Liu, X., Luo, D., Lu, Z. H., Yun, J. S., Saliba, M., Seok, S. I., & Zhang, W. (**2023**). Stabilization of photoactive phases for perovskite photovoltaics. *Nature Reviews Chemistry*, *7*(7), 462-479.

Li, T., Senesi, A. J., & Lee, B. (**2016**). Small angle X-ray scattering for nanoparticle research. *Chemical reviews*, *116*(18), 11128-11180.

Li, Wang, *et al*., (**2023**) "Co-passivation of perovskite film towards stable and efficient perovskite solar cell." *Chemical Engineering Journal* 471 : 144561.

Li, W., Dong, H., Wang, L., Li, N., Guo, X., Li, J., & Qiu, Y. (**2014**). Montmorillonite as bifunctional buffer layer material for hybrid perovskite solar cells with protection from corrosion and retarding recombination. *Journal of Materials Chemistry A*, *2*(33), 13587-13592.

Li, X., Aftab, S., Hussain, S., Kabir, F., Henaish, A. M. A., Al-Sehemi, A. G., ... & Koyyada, G. (2024). Dimensional diversity (0D, 1D, 2D, and 3D) in perovskite solar cells: exploring the potential of mixed-dimensional integrations. *Journal of Materials Chemistry A*, *12*(8), 4421-4440.

Li, Y., Wei, R., Dong, L., Guo, S., & Li, Z. (**2023**). Analysis of Scientific and Technological Performance and Impact of Synchrotron Radiation Light Source Based on Beamlines: A Case Study of Advanced Photon Source. *Qualitative and Quantitative Methods in Libraries*, *12*(3), 431-453.

Li, Y., Yang, Q., & Tian, Y. (**2024**). Quasi-monochromatic radiation from a circularly polarized laser pulse cross colliding with a relativistic electron. *Optik*, *313*, 171987.

Li, Z., Yang, M., Park, J. S., Wei, S. H., Berry, J. J., & Zhu, K. (**2016**). Stabilizing perovskite structures by tuning tolerance factor: formation of formamidinium and cesium lead iodide solid-state alloys. *Chemistry of Materials*, *28*(1), 284-292.

Luo, C., Zheng, G., Wang, X., Gao, F., Zhan, C., Gao, X., & Zhao, Q. (**2023**). Solid–solid chemical bonding featuring targeted defect passivation for efficient perovskite photovoltaics. *Energy & Environmental Science*, *16*(1), 178-189.

Luo, L., & Zhang, S. (**2010**). Applications of synchrotron-based X-ray techniques in environmental science. *Science China Chemistry*, *53*, 2529-2538.

Macfarlane, A. (**2021**). *Creative Lives and Works: Antony Hewish, Martin Rees and Neil Turok.* Routledge.

Ma, F., Li, J., Li, W., Lin, N., Wang, L., & Qiao, J. (**2017**). Stable α/δ phase junction of formamidinium lead iodide perovskites for enhanced near-infrared emission. *Chemical science*, *8*(1), 800-805.

Marronnier, A., Roma, G., Boyer-Richard, S., Pedesseau, L., Jancu, J. M., Bonnassieux, Y., *et al*., (**2018**). Anharmonicity and disorder in the black phases of cesium lead iodide used for stable inorganic perovskite solar cells. *ACS nano*, *12*(4), 3477-3486.

Mathies, F., List-Kratochvil, E. J., & Unger, E. L. (2020). Advances in inkjet-printed metal halide perovskite photovoltaic and optoelectronic devices. *Energy Technology*, *8*(4), 1900991.

Maxwell, J. C. (**1873**). *A treatise on electricity and magnetism* (Vol. 1). Clarendon press.

McDowell, C. I. (**2018**). *Unconventional Strategies Toward Efficient Self-Assembly in Solution Processed Small Molecule Organic Photovoltaics* (Doctoral dissertation, University of California, Santa Barbara).

Miao, Y., Chen, Y., Chen, H., Wang, X., & Zhao, Y. (**2021**). Using steric hindrance to manipulate and stabilize metal halide perovskites for optoelectronics. *Chemical Science*, *12*(21), 7231-7247.

Miles, R. W., Hynes, K. M., & Forbes, I. (**2005**). Photovoltaic solar cells: An overview of state-of-the-art cell development and environmental issues. *Progress in crystal growth and characterization of materials*, *51*(1-3), 1-42.

Miller, A. I. (**2014**). *Colliding worlds: how cutting-edge science is redefining contemporary art*. WW Norton & Company.

Mills, D. M. (**1991**). Time-resolved studies. In Handbook on synchrotron radiation. Version V1., Vol. 3 (pp. 291–335): 0 444 87422 4, https://inis.iaea.org/records/wy0jv-ce6511

Mino, L., Borfecchia, E., Segura-Ruiz, J., Giannini, C., Martinez-Criado, G., & Lamberti, C. (**2018**). Materials characterization by synchrotron x-ray microprobes and nanoprobes. *Reviews of Modern Physics*, *90*(2), 025007.

Mishra, R. K., Cherusseri, J., Allahyari, E., Thomas, S., & Kalarikkal, N. (**2017**). Small-angle light and X-ray scattering in nanosciences and nanotechnology. *Thermal and Rheological Measurement Techniques for Nanomaterials Characterization*, 233-269.

Mobilio, S., Boscherini, F., & Meneghini, C. (**2016**). *Synchrotron Radiation*. Springer-Verlag Berlin An.

MULHAUPT, G. (**1995**). Injector Systems. *Synchrotron Radiation Sources-A Primer*, *1*, 59.

Müller, A., Ghosh, M., Sonnenschein, R., & Woditsch, P. (2006). Silicon for photovoltaic applications. *Materials Science and Engineering: B*, *134*(2-3), 257-262.

Muscarella, L. A., Hutter, E. M., Sanchez, S., Dieleman, C. D., Savenije, T. J., Hagfeldt, A., ... & Ehrler, B. (**2019**). Crystal orientation and grain size: do they determine optoelectronic properties of $MAPbI_3$ perovskite?. *The journal of physical chemistry letters*, *10*(20), 6010-6018.

Nambu, A., Yoneyama, A., Takamatsu, D., Konishi, K., & Fujita, R. (**2019**). Advanced Analysis of Materials Using Synchroton Radiation. *Hitachi Review*, *68*(1), 90-91.

Narayanan, T. (**2014**). Small-Angle Scattering. *Structure from Diffraction Methods*, 259-324.

National Institute of Standards and Technology (NIST). (**2025**). *What is synchrotron radiation?* Retrieved [24th March, 2025], from https://www.nist.gov/pml/sensor-science/what- synchrotron- radiation

National Renewable Energy Laboratory. (2020, February 19). *NREL research boosts stability of perovskites, helps silicon solar cells*. U.S. Department of Energy. https://www.nrel.gov/news/press/2020/nrel-research-boosts-stability-of-perovskites-helps-silicon-solar-cells.html

NobelPrize.org. (**2025**). *Charles Glover Barkla – Facts*. Nobel Prize. Retrieved [23rd March, 2025], from https://www.nobelprize.org/prizes/physics/1917/barkla/facts/

Noh, J. H., Im, S. H., Heo, J. H., Mandal, T. N., & Seok, S. I. (**2013**). Chemical management for colorful, efficient, and stable inorganic–organic hybrid nanostructured solar cells. *Nano letters*, *13*(4), 1764-1769.

Olson, J. M., Friedman, D. J., & Kurtz, S. (**2003**). High-efficiency III-V multijunction solar cells. *Handbook of Photovoltaic Science and Engineering*, *2*.

O'Neill, W. (**2024, October**). Seeing the light: key inventions that illuminate our world. In *Journal of Physics: Conference Series* (Vol. 2877, No. 1, p. 012068). IOP Publishing.

Péan, E. V., Dimitrov, S., De Castro, C. S., & Davies, M. L. (2020). Interpreting time-resolved photoluminescence of perovskite materials. *Physical Chemistry Chemical Physics*, *22*(48), 28345-28358.

Perovskite-Info. (**2025**). *Perovskite materials - an introduction*. https://www.perovskite-info.com/introduction

Persson, I., Lyczko, K., Lundberg, D., Eriksson, L., & Płaczek, A. (**2011**). Coordination chemistry study of hydrated and solvated lead (II) ions in solution and solid state. *Inorganic chemistry*, *50*(3), 1058-1072.

Petrović, M., Chellappan, V., & Ramakrishna, S. (**2015)**. Perovskites: solar cells & engineering applications–materials and device developments. *Solar Energy*, *122*, 678-699.

Philipps, S. P., Dimroth, F., & Bett, A. W. (**2018**). High-efficiency III–V multijunction solar cells. In *McEvoy's handbook of photovoltaics* (pp. 439-472). Academic Press.

Prince, E. (**2006**). Mathematical, physical and chemical tables, *International Union of Crystallography,* Chester, England.

Sharp-Paul, N. (**2017**). Synchrotron research solves art mystery.

Shin, S. (**2021**). New era of synchrotron radiation: fourth-generation storage ring. *AAPPS Bulletin*, *31*(1), 21.

Qin, Z., Xue, H., Qin, M., Li, Y., Wu, X., Wu, W. R., ... & Lu, X. (**2023**). Critical Influence of Organic A′-Site Ligand Structure on 2D Perovskite Crystallization. *Small*, *19*(12), 2206787.

Qiu, S., Dong, L., Jang, D., Yang, F., Cerrillo, J. G., Li, C., ... & Egelhaaf, H. J. (**2024**). Printing High-Quality Formanidinum Lead Triiodide Films: Understanding the Critical Role of α-Phase Nucleation Before Thermal Annealing. *Advanced Energy Materials*, *14*(48), 2402616.6.

Qi, Y., Liu, Y., Lin, C., Deng, Y., Bai, P., Gao, Y., ... & Jin, Y. (**2023**). Anisotropic emission of orientation-controlled mixed-dimensional perovskites for light-emitting devices. *Journal of Materiomics*, *9*(4), 762-767.

Pan, Y., Zeng, Q., Li, L., Deng, M., Liao, X., Zhang, M., ... & Liu, F. (**2024**). Aqueous Synthesis of α-$Cs_xFA_{1-x}PbI_3$ Microcrystals for Efficient Perovskite Solar Cells. *ACS Applied Energy Materials*, *7*(15), 6022-6031.

RaeisianAsl, M., Panahi, S. F. K., Jamaati, M., & Tafreshi, S. S. (2022). A review on theoretical studies of structural and optoelectronic properties of FA-based perovskite materials with a focus on FAPbI3. *International Journal of Energy Research*, *46*(10), 13117-13151.

Remmerswaal, W. H. M. (2024). Measuring Voltage with Light: Absolute Photoluminescence of Metal Halide Perovskites.

Renaud, G., Lazzari, R., & Leroy, F. (**2009**). Probing surface and interface morphology with grazing incidence small angle X-ray scattering. *Surface Science Reports*, *64*(8), 255-380.

Renaud, J. P. (Ed.). (**2020**). *Structural biology in drug discovery: methods, techniques, and practices*. John Wiley & Sons.

Rezaee, E., Zhang, W., & Silva, S. R. P. (**2021**). Solvent engineering as a vehicle for high quality thin films of perovskites and their device fabrication. *Small*, *17*(25), 2008145.

Rodríguez-hornedo, N., & Murphy, D. (**1999**). Significance of controlling crystallization mechanisms and kinetics in pharmaceutical systems. *Journal of pharmaceutical sciences*, *88*(7), 651-660.

Rojo, T., Insausti, M., Arriortua, M. I., Hernandez, E., & Zubillaga, J. (**1992**). Thermal decomposition study of some complexes, precursors of mixed oxides, with formula MM'(L)· nH2O (M, M'= Bi, Pb, Sr, Ca and Cu; L= EDTA-like ligands). *Thermochimica acta*, *195*, 95-104.

Romano, R. (1869). *Print connections*. Publisher.

Roth, B., Søndergaard, R. R., & Krebs, F. C. (2015). Roll-to-roll printing and coating techniques for manufacturing large-area flexible organic electronics. *Handbook of flexible organic electronics: Materials, manufacturing and applications*, 171-197.

Saliba, M., Matsui, T., Seo, J. Y., Domanski, K., Correa-Baena, J. P., Nazeeruddin, M. K., ... & Grätzel, M. (**2016**). Cesium-containing triple cation perovskite solar cells: improved stability, reproducibility and high efficiency. *Energy & environmental science*, *9*(6), 1989-1997.

Sanchez, E. R., Powis, A. T., Kaganovich, I. D., Marshall, R., Porazik, P., Johnson, J., ... & Nicolls, M. (**2019**). Relativistic particle beams as a resource to solve outstanding problems in space physics. *Frontiers in Astronomy and Space Sciences*, *6*, 71.

Sánchez, S., Pfeifer, L., Vlachopoulos, N., & Hagfeldt, A. (2021). Rapid hybrid perovskite film crystallization from solution. *Chemical Society Reviews*, *50*(12), 7108-7131.

Schlipf, J., Docampo, P., Schaffer, C. J., Körstgens, V., Bießmann, L., Hanusch, F., ... & Müller-Buschbaum, P. (**2015**). A closer look into two-step perovskite conversion with X-ray scattering. *The journal of physical chemistry letters*, *6*(7), 1265-1269.

Schlipf, J., & Müller-Buschbaum, P. (**2017**). Structure of organometal halide perovskite films as determined with grazing-incidence x-ray scattering methods. *Advanced energy materials*, *7*(16), 1700131.

Schlueter, R. D. (**1994)**. Wiggler and undulator insertion devices. *Synchrotron Radiation Sources±A Primer*.

Schmalensee, R., (**2015**). The future of solar energy: A personal assessment. *Energy economics*, *52*, S142-S148.

Schneider, J. R. (**2010**). Photon science at accelerator-based light sources. *Reviews of Accelerator Science and Technology*, *3*(01), 13-37.

Schötz, K., & Panzer, F. (**2021**). Using *in situ* optical spectroscopy to elucidate film formation of metal halide perovskites. *The Journal of Physical Chemistry A*, *125*(11), 2209-2225.

SEES. (**2025**). Retrieved [24th March, 2025] *Synchrotron radiation*. SEES Science. https://seescience.org/applications-and-techniques/synchrotron-radiation/

Shai, X., Wang, J., Sun, P., Huang, W., Liao, P., Cheng, F., ... & Wang, M. (**2018**). Achieving ordered and stable binary metal perovskite via strain engineering. *Nano Energy*, *48*, 117-127.

Shao, H., Zhai, Y., Wu, X., Xu, W., Xu, L., Dong, B., ... & Song, H. (**2020**). High brightness blue light-emitting diodes based on CsPb (Cl/Br)$_3$ perovskite QDs with phenethylammonium chloride passivation. *Nanoscale*, *12*(21), 11728-11734.

Shatsala, M., Wanyonyi, S., Awino, C., Mageto, M., & Golicha, H. (**2025**). Comparative study of crystallization kinetics and phase segregation of triple cation and methylammonium lead iodide perovskites on moisture probing using synchrotron X-ray based radiation. *Synchrotron Radiation*, *32*(1).

Shi, Y., Chu, W., Zhang, L., Wang, B., Saidi, W. A., Zhao, J., & Prezhdo, O. V. (2025). Band Gap Narrowing in Lead-Halide Perovskites by Dynamic Defect Self-Doping for Enhanced Light Absorption and Energy Upconversion. *Chemistry of Materials*.

Silva, M. I., Malitckii, E., Santos, T. G., & Vilaça, P. (**2023**). Review of conventional and advanced non-destructive testing techniques for detection and characterization of small-scale defects. *Progress in Materials Science*, *138*, 101155.

Simonyi, K. (**2012**). *A cultural history of physics*. CRC Press.

Singh, H., Dhakla, S., Deendyal, P. K., Kumar, A., Kumar, S., Gupta, G., & Kashyap, M. K. (2024). Enhanced structural and optical properties of Cs0. 1FA0. 9PbI3 perovskite thin film with potassium doping for perovskite solar cells. *Journal of Physics and Chemistry of Solids*, *193*, 112145.

Skulls in the Stars. (**2009, June 6**). *Barkla shows that X-rays have polarization (1905)*. Retrieved [24th MARCH, 2025], from https://skullsinthestars.com/2009/06/06/barkla-shows-that-x-rays-have polarization-1905/

Smith, B. (2016). A process for successful infrared spectral interpretation.

Snaith, H. J., Abate, A., Ball, J. M., Eperon, G. E., Leijtens, T., Noel, N. K., ... & Zhang, W. (**2014**). Anomalous hysteresis in perovskite solar cells. *The journal of physical chemistry letters*, *5*(9), 1511-1515.

Song, F., Zheng, D., Feng, J., Liu, J., Ye, T., Li, Z., ... & Yang, D. (**2024**). Mechanical durability and flexibility in perovskite photovoltaics: advancements and applications. *Advanced Materials*, *36*(18), 2312041.

Song, T. B., Yuan, Z., Mori, M., Motiwala, F., Segev, G., Masquelier, E., ... & Sutter-Fella, C. M. (2020). Revealing the dynamics of hybrid metal halide perovskite formation via multimodal *in situ* probes. *Advanced Functional Materials*, *30*(6), 1908337.

Springtime at Daresbury - Symmetry Magazine, https://www.symmetrymagazine.org/article/may-2005/springtime daresbury?language_content_entity=und

Stanik, E., Döhring, T., Schreiber, K., Kätker, A., & Busch, U. (**2023**). The Röntgen Medal: honouring x-ray excellence. In *EUV and X-ray Optics: Synergy between Laboratory and Space VIII* (Vol. 12576, pp. 58-65). SPIE.

Steele, J. A., Solano, E., Hardy, D., Dayton, D., Ladd, D., White, K., ... & Toney, M. F. (**2023**). How to GIWAXS: grazing incidence wide angle X-ray scattering applied to metal halide perovskite thin films. *Advanced Energy Materials*, *13*(27), 2300760.

Stoumpos, C. C., Cao, D. H., Clark, D. J., Young, J., Rondinelli, J. M., Jang, J. I., ... & Kanatzidis, M. G. (**2016**). Ruddlesden–Popper hybrid lead iodide perovskite 2D homologous semiconductors. *Chemistry of Materials*, *28*(8), 2852-2867.

Stoumpos, C. C., Malliakas, C. D., & Kanatzidis, M. G. (**2013**). Semiconducting tin and lead iodide perovskites with organic cations: phase transitions, high mobilities, and near-infrared photoluminescent properties. *Inorganic chemistry*, *52*(15), 9019-9038.

Su, B., Li, J., Deng, B., Pianetta, P., & Liu, Y. (**2024**). Multi-modal X-ray microscopy for chemical analysis. *TrAC Trends in Analytical Chemistry*, *171*, 117491.

Sun, K., Guo, R., Liang, Y., Heger, J. E., Liu, S., Yin, S., ... & Müller-Buschbaum, P. (**2023**). Morphological insights into the degradation of perovskite solar cells under light and humidity. *ACS Applied Materials & Interfaces*, *15*(25), 30342-30349.

Sun, Q., Wang, J., & Shi, J. (2010). Prediction and assignment of site occupation and energy levels for Pb2+ ions in crystal hosts. *Journal of Solid State Chemistry*, *183*(5), 1174-1179.

Sun, Q., & Yin, W. J. (**2017**). Thermodynamic stability trend of cubic perovskites. *Journal of the American Chemical Society*, *139*(42), 14905-14908.

Sun, S., Yuan, D., Xu, Y., Wang, A., & Deng, Z. (**2016**). Ligand-mediated synthesis of shape-controlled cesium lead halide perovskite nanocrystals via reprecipitation process at room temperature. *ACS nano*, *10*(3), 3648-3657.

Szostak, R., de Souza Gonçalves, A., de Freitas, J. N., Marchezi, P. E., de Araújo, F. L., Tolentino, H. C. N., ... & Nogueira, A. F. (**2023**). *In situ* and operando characterizations of metal halide perovskite and solar cells: insights from lab-sized devices to upscaling processes. *Chemical reviews*, *123*(6), 3160-3236.

Takeda, T., Itai, Y., Hyodo, K., Ando, M., Akatsuka, T., & Uyama, C. (**1998**). Medical applications with synchrotron radiation in Japan. *Synchrotron Radiation*, *5*(3), 326-332.

Tamura, L., Hussain, Z., Padmore, H. A., Robin, D. S., Bailey, S., Feinberg, B., & Falcone, R. W. (**2012**). Advanced light source update. *Synchrotron Radiation News*, *25*(3), 25-30.

TAMURA, N., DEJOIE, C., & MARTINETTO, P. (**2024**). Development of the Use of Synchrotron Radiation for the Study of Cultural Heritage Materials. *Synchrotron Radiation, Cultural Heritage, Biomineralization*, 17-67.

Tamura, N., Kunz, M., Chen, K., Celestre, R. S., MacDowell, A. A., & Warwick, T. (**2009**). A superbend X-ray microdiffraction beamline at the advanced light source. *Materials Science and Engineering: A*, *524*(1-2), 28-32.

Tan, W. L., Cheng, Y. B., & McNeill, C. R. (**2020**). Direct assessment of structural order and evidence for stacking faults in layered hybrid perovskite films from X-ray scattering measurements. *Journal of Materials Chemistry A*, *8*(25), 12790-12798.

Telschow, Oscar, Miguel Albaladejo-Siguan, Lena Merten, Alexander D. Taylor, Katelyn P. Goetz, Tim Schramm, Oleg V. Konovalov *et al*. (**2022**)"Preserving the stoichiometry of triple-cation perovskites by carrier-gas-free antisolvent spraying." Journal of Materials Chemistry A 10, no. 37 : 9743-19749.

Thomas, O., Labat, S., Cornelius, T., & Richard, M. I. (**2022**). X-ray diffraction imaging of deformations in thin films and nano-objects. *Nanomaterials*, *12*(8), 1363.

Tubiana, M. (**1996**). Wilhelm Conrad Röntgen and the discovery of X-rays. *Bulletin de l'Academie nationale de medecine*, *180*(1), 97-108.

Tong, Y., Bi, X., Xu, S., Min, H., Cheng, L., Kuang, Z., ... & Wang, J. (**2023**). *In situ* halide exchange of cesium lead halide perovskites for blue light-emitting diodes. *Advanced Materials*, *35*(3), 2207111.

Urwick, A. (**2023**). *Enhancing the Structural Stability of α-phase Hybrid Perovskite Films through Defect Engineering Approaches under Ambient Conditions* (Doctoral dissertation, University of Sheffield).

Vénien-Bryan, C., Li, Z., Vuillard, L., & Boutin, J. A. (**2017**). Cryo-electron microscopy and X- ray crystallography: complementary approaches to structural biology and drug discovery. *Structural Biology and Crystallization Communications*, *73*(4), 174-183.

Wang, B., Young Wong, K., Xiao, X., & Chen, T. (**2015**). Elucidating the reaction pathways in the synthesis of organolead trihalide perovskite for high-performance solar cells. *Scientific reports*, *5*(1), 10557.

Wang, C., Steiner, U., & Sepe, A. (**2018**). Synchrotron big data science. *Small*, *14*(46), 1802291.

Wang, Q., & Abate, A. (**2018**). Strategies toward stable perovskite solar cells. *Advanced Materials Interfaces*, *5*(22), 1800264.

Wang, R., Xue, J., Meng, L., Lee, J. W., Zhao, Z., Sun, P., ... & Yang, Y. (**2019**). Caffeine improves the performance and thermal stability of perovskite solar cells. *Joule*, *3*(6), 1464-1477.

Wang, S., Jin, J., Qi, Y., Liu, P., Xia, Y., Jiang, Y., ... & Zhao, X. Z. (**2020**). δ-$CsPbI_3$ intermediate phase growth assisted sequential deposition boosts stable and high-efficiency triple cation perovskite solar cells. *Advanced Functional Materials*, *30*(7), 1908343.

Wang, S., Yu, J., Zhang, M., Chen, D., Li, C., Chen, R., ... & Yang, X. (**2019**). Stable, strongly emitting cesium lead bromide perovskite nanorods with high optical gain enabled by an intermediate monomer reservoir synthetic strategy. *Nano letters*, *19*(9), 6315-6322.

Wang, Y., Ye, S., Lim, J. W. M., Giovanni, D., Feng, M., Fu, J., ... & Sum, T. C. (**2023**). Carrier multiplication in perovskite solar cells with internal quantum efficiency exceeding 100%. *Nature Communications*, *14*(1), 6293.

Weihreter, E., & Wuestefeld, G. (**1999**). Low energy storage rings with extended spectral range. *Synchrotron Radiation News*, *12*(6), 16-24.

Weiss, M., Horn, J., Richter, C., & Schlettwein, D. (**2016**). Preparation and characterization of methylammonium tin iodide layers as photovoltaic absorbers. *physica status solidi (a)*, *213*(4), 975-981.

Wikipedia contributors. (**2025**). *A Treatise on Electricity and Magnetism*. Wikipedia, The Free Encyclopedia. Retrieved [24th March, **2025**], from https://en.wikipedia.org/wiki/A_Treatise_on_Electricity_and_Magnetism

Wikipedia contributors. (**2025**). *Synchrotron radiation*. Wikipedia, The Free Encyclopedia. Retrieved [23rd March, **2025**], from https://en.wikipedia.org/wiki/Synchrotron_radiation

Willmott, P. (**2019**). *An introduction to synchrotron radiation: techniques and applications*. John Wiley & Sons.

Win, A. A., Chou, K. C., Zeitz, D. C., Todd, C., & Zhang, J. Z. (**2022**). Origin of the near 400 nm absorption and emission band in the synthesis of cesium lead bromide nanostructures: metal halide molecular clusters rather than perovskite magic-sized clusters. *The Journal of Physical Chemistry Letters*, *14*(1), 116-121.

Winick, H. (**1994**). *Synchrotron radiation sources: a primer* (Vol. 1). World Scientific.

Winick, H., Brown, G., Halbach, K., & Harris, J. (**1981**). Wiggler and undulator magnets. *Physics Today*, *34*(5), 50-63.

Winick, H., & Doniach, S. (**2012**). *Synchrotron radiation research*. Springer Science & Business Media.

Wu, J., He, M., Liu, C., & Gao, P. (2025). Charge Dynamics and Defect States under "Spot-Light": Spectroscopic Insights into Halide Perovskite Solar Cells. *Advanced Photonics Research*, *6*(3), 2400110.

Wu, X., Wang, S., Zhang, J., Shiu, H. W., Hsu, Y. J., Yan, H., ... & Lu, X. (**2023**). Bypassing the non-perovskite yellow phase: Revealing and regulating the crystallization pathways for efficient all-inorganic perovskite solar cells. *Nano Energy*, *117*, 108907.

Xiang, W., Zhang, J., Liu, S. F., Albrecht, S., Hagfeldt, A., & Wang, Z. (**2022**). Intermediate phase engineering of halide perovskites for photovoltaics. *Joule*, *6*(2), 315-339

Xiao, C., Zhang, J., Li, Y., Xie, M., & Sun, D. (**2025**). Application of Synchrotron Radiation in Fundamental Research and Clinical Medicine.

Xie, L. Q., Chen, L., Nan, Z. A., Lin, H. X., Wang, T., Zhan, D. P., ... & Tian, Z. Q. (**2017**). Understanding the cubic phase stabilization and crystallization kinetics in mixed cations and halides perovskite single crystals. *Journal of the American Chemical Society*, *139*(9), 3320-3323.

Xi, J., Xi, K., Sadhanala, A., Zhang, K. H., Li, G., Dong, H., ... & Wu, Z. (2019). Chemical sintering reduced grain boundary defects for stable planar perovskite solar cells. *Nano Energy*, *56*, 741-750.

Xing, G., Mathews, N., Sun, S., Lim, S. S., Lam, Y. M., Grätzel, M., ... & Sum, T. C. (**2013**). Long-range balanced electron-and hole-transport lengths in organic-inorganic $CH_3NH_3PbI_3$. *Science*, *342*(6156), 344-347.

Yamada, I., Takamatsu, A., & Ikeno, H. (**2018**). Complementary evaluation of structure stability of perovskite oxides using bond-valence and density-functional-theory calculations. *Science and Technology of advanced MaTerialS*, *19*(1), 101-107.

Yang, B., Bogachuk, D., Suo, J., Wagner, L., Kim, H., Lim, J., ... & Hagfeldt, A. (**2022**). Strain effects on halide perovskite solar cells. *Chemical Society Reviews*, *51*(17), 7509-7530.

Yan, K., Long, M., Zhang, T., Wei, Z., Chen, H., Yang, S., & Xu, J. (**2015**). Hybrid halide perovskite solar cell precursors: colloidal chemistry and coordination engineering behind device processing for high efficiency. *Journal of the American Chemical Society*, *137*(13), 4460-4468.

Yella, A., Lee, H. W., Tsao, H. N., Yi, C., Chandiran, A. K., Nazeeruddin, M. K., ... & Grätzel, M. (**2011**). Porphyrin-sensitized solar cells with cobalt (II/III)–based redox electrolyte exceed 12 percent efficiency. *science*, *334*(6056), 629-634.

Yin, W. J., Shi, T., & Yan, Y. (**2014**). Unusual defect physics in $CH_3NH_3PbI_3$ perovskite solar cell absorber. *Applied Physics Letters*, *104*(6).

Yoon, B., & Lee, H. (2025). Defect passivation with spectral shift for improved efficiency and stability of quasi-2D blue perovskite light emitting diodes. *Applied Surface Science*, *682*, 161623.

Zakeeruddin, M., Dar, M. I., Grätzel, M., & Schreiber, F. (**2022**). Quantifying Stabilized Phase Purity in Formamidinium-Based Multiple-Cation Hybrid Perovskites. *Because you have seen me, you have believed; blessed are those who have not seen and yet have believed.*

Zhang, F. (**2015**). *Determination of the stress field in polycrystalline materials by Laue microdiffraction* (Doctoral dissertation, Ecole nationale supérieure d'arts et métiers-ENSAM).

Zhang, J., Li, C., Chen, M., & Huang, K. (**2020**). Real-time observation of ion migration in halide perovskite by photoluminescence imaging microscopy. *Journal of Physics D: Applied Physics*, *54*(4), 044002.

Zhang, T., Xu, Q., Xu, F., Fu, Y., Wang, Y., Yan, Y., ... & Zhao, Y. (2019). Spontaneous low-temperature crystallization of α-FAPbI3 for highly efficient perovskite solar cells. *Science bulletin*, *64*(21), 1608-1616.

Zhang, W., Saliba, M., Moore, D. T., Pathak, S. K., Hörantner, M. T., Stergiopoulos, T., ... & Snaith, H. J. (**2015**). Ultrasmooth organic–inorganic perovskite thin-film formation and crystallization for efficient planar heterojunction solar cells. *Nature communications*, *6*(1), 6142.

Zhao, C., Zhang, H., Krishna, A., Xu, J., & Yao, J. (2024). Interface engineering for highly efficient and stable perovskite solar cells. *Advanced Optical Materials*, *12*(7), 2301949.

Zhao, J., Liu, X., & Wu, Z. (**2023**) Temperature-dependent Structure and Carrier Dynamics in CsMAFA-based Perovskites. *Interplay of Structural and Light-induced Carrier Dynamics in Metal Halide Perovskites*, 61.

Zhao, X., Gao, W., Dong, H., Zhou, Y., Huang, H., Wu, Z., & Ran, C. (2024). Advanced technical strategies for upscaling perovskite photovoltaics from cells to modules. *Nano Energy*, 109933.

Zheng, G., Zhu, C., Ma, J., Zhang, X., Tang, G., Li, R., ... & Zhou, H. (**2018**). Manipulation of facet orientation in hybrid perovskite polycrystalline films by cation cascade. *Nature communications*, *9*(1), 2793.

Zheng, X., Lei, H., Yang, G., Ke, W., Chen, Z., Chen, C., ... & Fang, G. (**2017**). Enhancing efficiency and stability of perovskite solar cells via a high mobility p-type PbS buffer layer. *Nano Energy*, *38*, 1-11.

Zheng, X., Wu, C., Jha, S. K., Li, Z., Zhu, K., & Priya, S. (**2016**). Improved phase stability of formamidinium lead triiodide perovskite by strain relaxation. *ACS Energy Letters*, *1*(5), 1014-1020.

Zhou, W., Zhou, R., Chen, X., Zhou, Z., He, Y., Qian, C., ... & Yan, H. (2024). Synergy Between Dynamic Behavior of Hydrogen Defects and Non-Radiative Recombination in Metal-Halide Perovskites. *Small*, *20*(46), 2405201.

Zou, Y., Eichhorn, J., Zhang, J., Apfelbeck, F. A., Yin, S., Wolz, L., ... & Müller-Buschbaum, P. (**2024**). Microstrain and crystal orientation variation within naked triple-cation mixed halide perovskites under heat, UV, and visible light exposure. *ACS energy letters*, *9*(2), 388-399.

Zschornack, G. H. (**2007**). *Handbook of X-ray Data*. Springer Science & Business Media.

APPENDIX 1. Uv-Ozoone cleaner

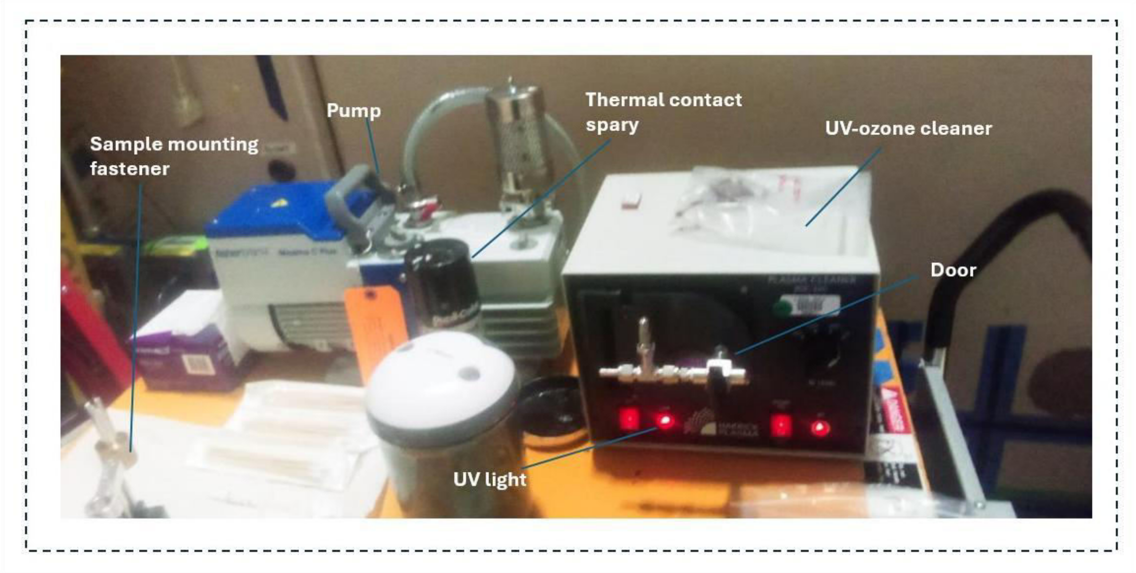

APPENDIX 2. Igor Pro commercial software installed with Nika Interface

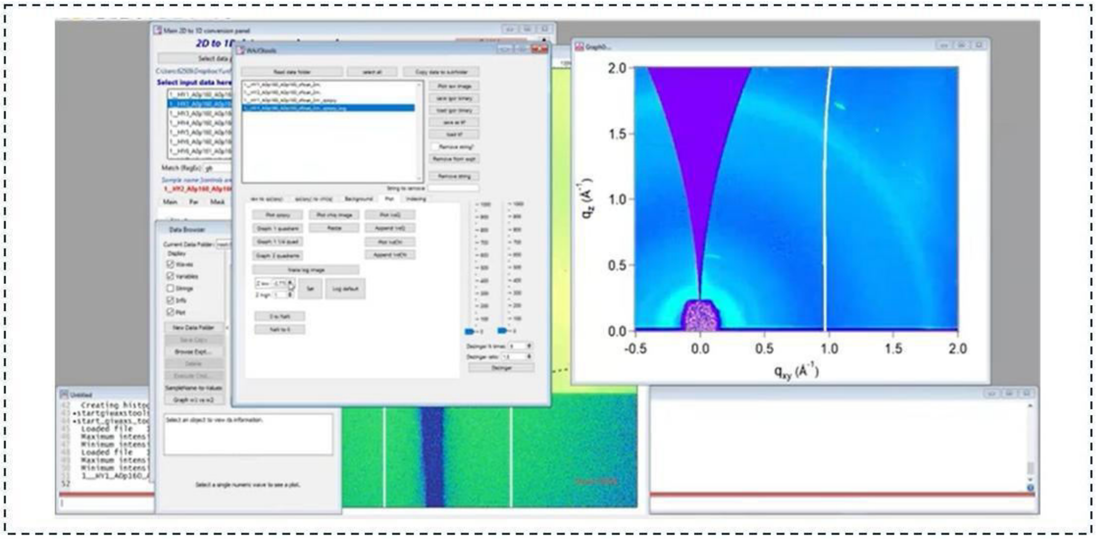

APPENDIX 3. Custom-made XRDSol software

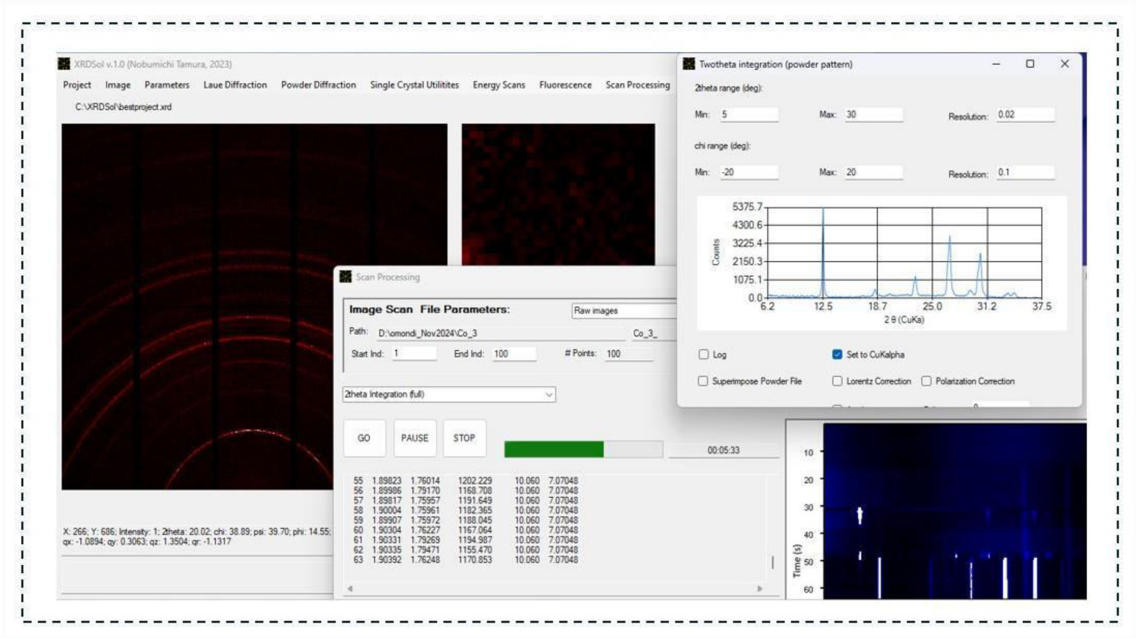

C:\XRDSol\bestproject.xrd

```
X: 266; Y: 686; Intensity: 1; 2theta: 20.02; chi: 38.89; psi: 39.70; phi: 14.55;
qx: -1.0894; qy: 0.3063; qz: 1.3504; qr: -1.1317
```

Raw images

Path: D:\omondi_Nov2024\Co_3 Co_3_

Start Ind: 1 End Ind: 100 # Points: 100

2theta Integration (full)

00:05:33

```
55  1.89823  1.76014    1202.229     10.060  7.07048
56  1.89986  1.79170    1168.708     10.060  7.07048
57  1.89817  1.75957    1191.649     10.060  7.07048
58  1.90004  1.75961    1182.365     10.060  7.07048
59  1.89907  1.75972    1188.045     10.060  7.07048
60  1.90304  1.76227    1167.064     10.060  7.07048
61  1.90331  1.79269    1194.987     10.060  7.07048
62  1.90335  1.79471    1155.470     10.060  7.07048
63  1.90392  1.76248    1170.853     10.060  7.07048
```

2theta range (deg):

Min: 5 Max: 30 Resolution: 0.02

chi range (deg):

Min: -20 Max: 20 Resolution: 0.1

☐ Log ☑ Set to CuKalpha

☐ Superimpose Powder File ☐ Lorentz Correction ☐ Polarization Correction

APPENDIX 4. Final Stage III is reached at 300 seconds for PPF passivated films

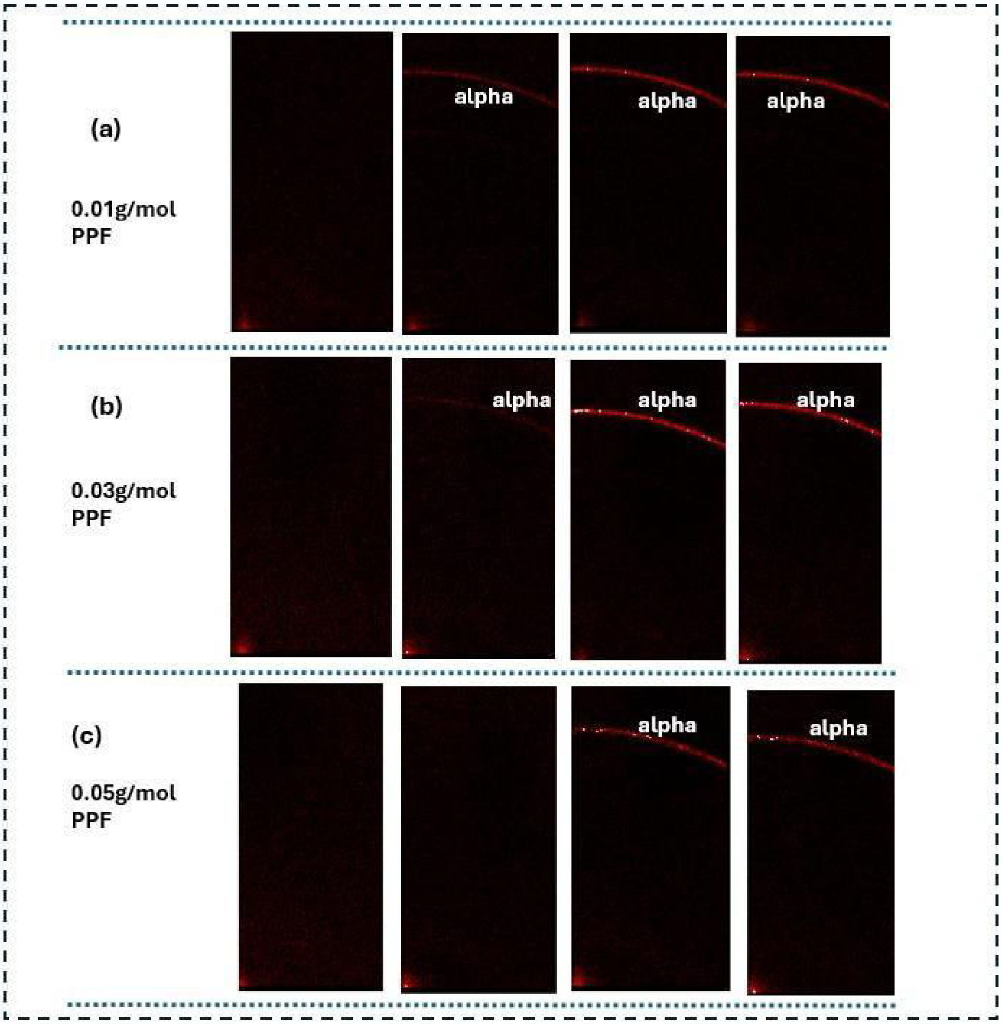

APPENDIX 5. Photo-Luminesence emmision tracking for PEACl/PPF co-passivated $Cs_{0.1}FA_{0.9}PbI_3$

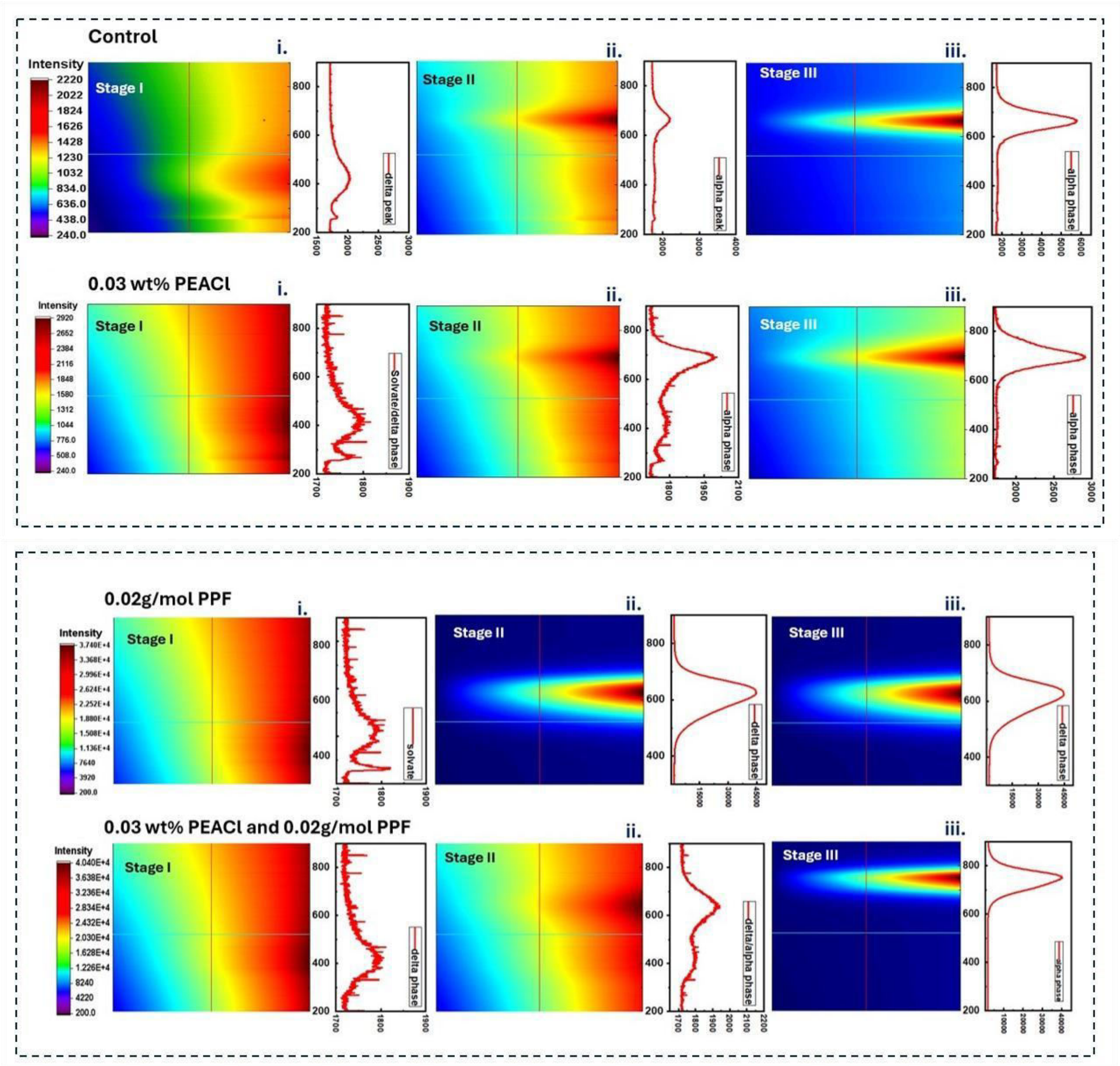

APPENDIX 6. Max-Normalized and Area-Normalized PL spectra

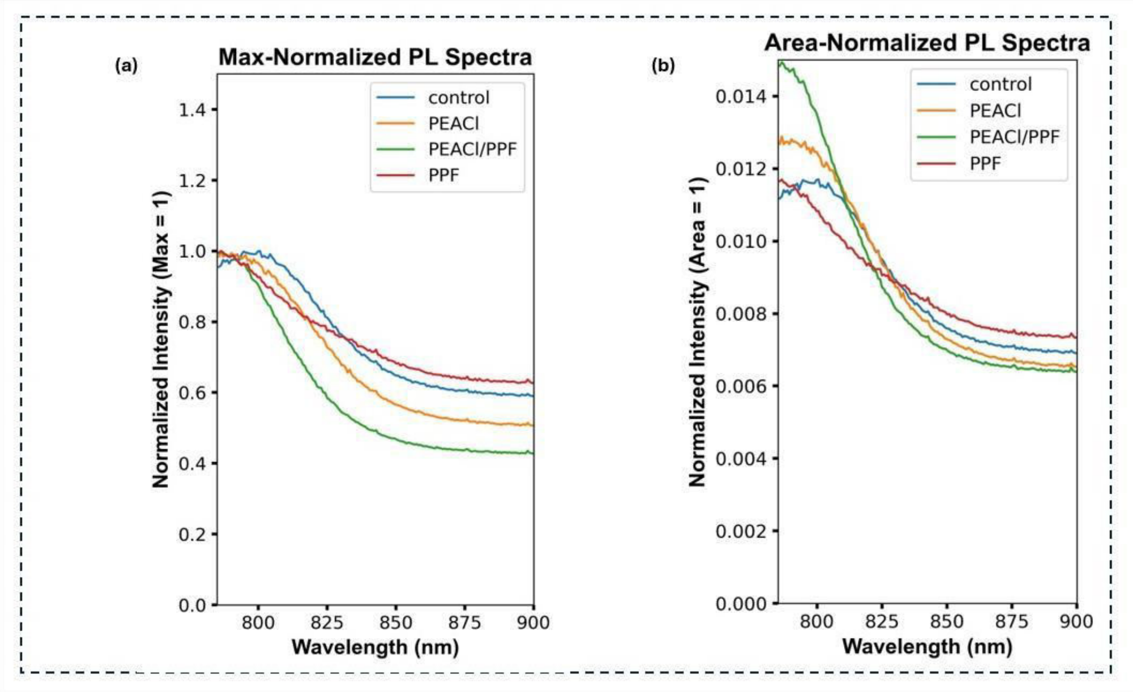

APPENDIX 7. Conversion of q to d-spacing

q ($Å^{-1}$)	d-spacing (Å)	Closest (hkl)	Calculated $d_{(hkl)}$ (Å)
0.2	31.42	(001) superlattice or layered 2D reflection (n1)	-
0.4	15.71	(001) in layered structure / long-range order (n1)	-
0.6	10.47	Possible organic spacing in hybrid perovskites	-
0.8	7.85	n=3 layered perovskite stacking repeat	-
0.9	6.98	PbI_2/Strained or relaxed (100)	-
1.0	**6.28**	**(100)**	**6.30**
1.2	5.24	(110)	4.46 (closer to q ≈ 1.41)
1.4	4.49	(110)	**4.46**
1.6	3.93	Between (110) and (111)	-
1.8	3.49	(111)	**3.64**
2.0	3.14	(200)	**3.15**
2.2	2.86	(210) or mixed-index plane	2.81 (for 211)
2.4	2.62	(211)	**2.81**
2.6	2.42	(220)	**2.23**
2.8	2.24	Between (211) and (220)	-
3.0	2.09	(310) or higher index	~2.05

APPENDIX 7. GIWAXS for 4008 Hours on PEACl/PPF passivated $Cs_{0.1}FA_{0.9}PbI_3$.

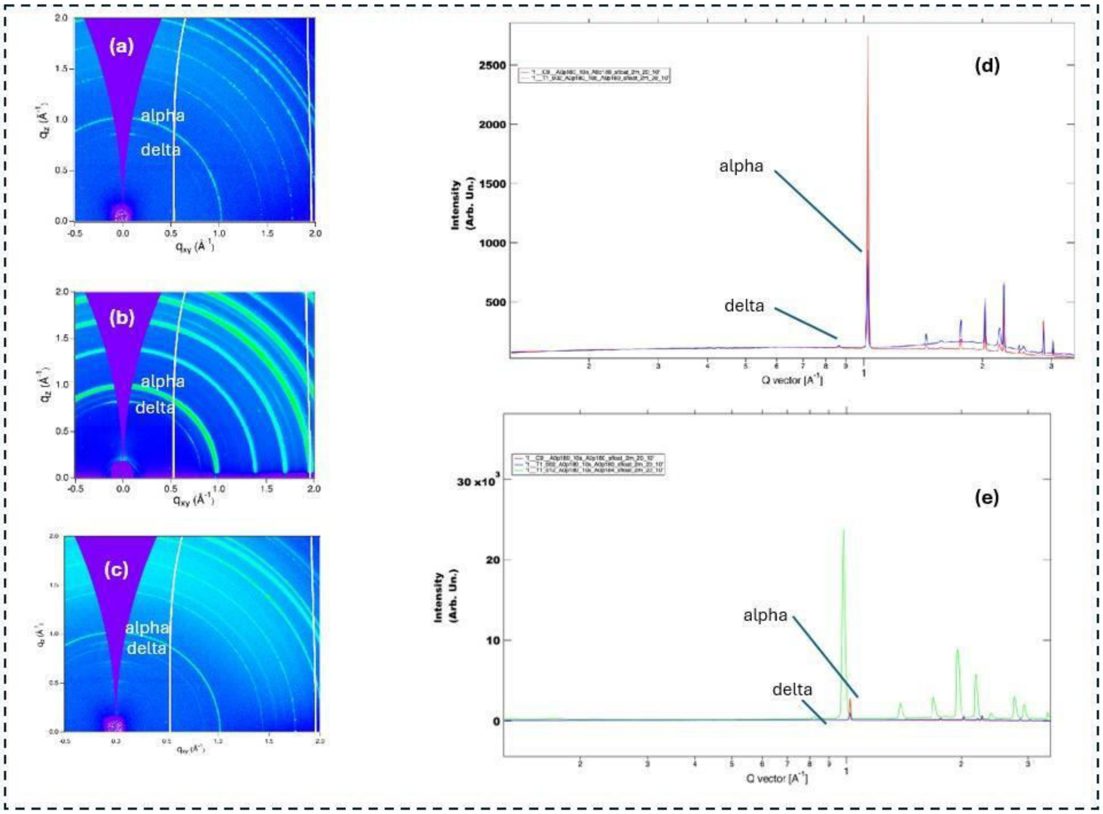

APPENDIX 8. Greek Alphabet

Greek alphabet			
Αα	Alpha	Νν	Nu
Ββ	Beta	Ξξ	Xi
Γγ	Gamma	Οο	Omicron
Δδ	Delta	Ππ	Pi
Εε	Epsilon	Ρρ	Rho
Ζζ	Zeta	Σσς	Sigma
Ηη	Eta	Ττ	Tau
Θθ	Theta	Υυ	Upsilon
Ιι	Iota	Φφ	Phi
Κκ	Kappa	Χχ	Chi
Λλ	Lambda	Ψψ	Psi
Μμ	Mu	Ωω	Omega

APPENDIX 9. Table of physical constants

Symbol	**Quantity**	**Value**[a][b]
$a_0 = \hbar/\alpha m_\mathrm{e} c$	Bohr radius	5.29177210544(82)×10^{-11} m
b[e]	Wien wavelength displacement law constant	2.897771955...×10^{-3} m⋅K
b_entropy	Wien entropy displacement law constant	3.002916077...×10^{-3} m⋅K
b'[f]	Wien frequency displacement law constant	5.878925757...×10^{10} Hz⋅K^{-1}
c	speed of light in vacuum	299792458 m⋅s^{-1}
$c_1 = 2\pi hc^2$	first radiation constant	3.741771852...×10^{-16} W⋅m^2
$c_\mathrm{1L} = 2hc^2/\mathrm{sr}$	first radiation constant for spectral radiance	1.191042972...×10^{-16} W⋅m^2⋅sr^{-1}
$c_2 = hc/k_\mathrm{B}$	second radiation constant	1.438776877...×10^{-2} m⋅K
e	elementary charge	1.602176634×10^{-19} C
$E_\mathrm{h} = \alpha^2 m_\mathrm{e} c^2$	Hartree energy	4.3597447222060(48)×10^{-18} J
$F = N_\mathrm{A} e$	Faraday constant	96485.3321233100184 C⋅mol^{-1}
G	Newtonian constant of gravitation	6.67430(15)×10^{-11} m^3⋅kg^{-1}⋅s^{-2}
$G_0 = 2e^2/h$	conductance quantum	7.748091729...×10^{-5} S
$G_0^{-1} = h/2e^2$	inverse conductance quantum	12906.40372... Ω
g_e	electron *g*-factor	−2.00231930436092(36)
$G_\mathrm{F}/(\hbar c)^3$	Fermi coupling constant	1.1663787(6)×10^{-5} GeV^{-2}
g_p	proton *g*-factor	5.5856946893(16)
g_μ	muon *g*-factor	−2.00233184123(82)
h	Planck constant	6.62607015×10^{-34} J⋅Hz^{-1}

Symbol	**Quantity**	**Value**[a][b]
$h/2m_{\mathrm{e}}$	quantum of circulation	$3.6369475467(11)\times10^{-4}$ m^{2}· s^{-1}
$\hbar = h/2\pi$	reduced Planck constant	$1.054571817...\times10^{-34}$ J· s
$K_{\mathrm{J}} = 2e/h$	Josephson constant	$483597.8484...\times10^{9}$ Hz· V^{-1}
k, k_{B}	Boltzmann constant	1.380649×10^{-23} J· K^{-1}
m_{e}	electron mass	$9.1093837139(28)\times10^{-31}$ kg
m_{n}	neutron mass	$1.67492750056(85)\times10^{-27}$ kg
m_{p}	proton mass	$1.67262192595(52)\times10^{-27}$ kg
$m_{\mathrm{p}}/m_{\mathrm{e}}$	proton-to-electron mass ratio	1836.152673426(32)
$m_{\mathrm{u}} = m(^{12}\mathrm{C})/12$	atomic mass constant	$1.66053906892(52)\times10^{-27}$ kg
$M_{\mathrm{u}} = M(^{12}\mathrm{C})/12$	molar mass constant	$1.00000000105(31)\times10^{-3}$ kg· mol^{-1}
$m_{\mathrm{W}}/m_{\mathrm{Z}}$	W-to-Z mass ratio	0.88145(13)
m_{μ}	muon mass	$1.883531627(42)\times10^{-28}$ kg
m_{τ}	tau mass	$3.16754(21)\times10^{-27}$ kg
$M(^{12}\mathrm{C}) = N_{\mathrm{A}}m(^{12}\mathrm{C})$	molar mass of carbon-12	$12.0000000126(37)\times10^{-3}$ kg· mol^{-1}
N_{A}	Avogadro constant	6.02214076×10^{23} mol^{-1}
$N_{\mathrm{A}}h$	molar Planck constant	$3.990312712893431\times10^{-10}$ J· s· mol^{-1}
$R_{\infty} = \alpha^2 m_{\mathrm{e}}c/2h$	Rydberg constant	10973731.568157(12) m^{-1}
$r_{\mathrm{e}} = \alpha\hbar/m_{\mathrm{e}}c$	classical electron radius	$2.8179403205(13)\times10^{-15}$ m
$R_{\mathrm{K}} = h/e^2$	von Klitzing constant	25812.80745... Ω
$R = N_{\mathrm{A}}k_{\mathrm{B}}$	molar gas constant	8.31446261815324 J· mol^{-1}· K^{-1}
$\mathrm{Ry} = R_{\infty}hc = E_{\mathrm{h}}/2$	Rydberg unit of energy	$2.1798723611030(24)\times10^{-18}$ J
$\sin^2\theta_{\mathrm{W}} = 1-(m_{\mathrm{W}}/m_{\mathrm{Z}})^2$	sine-square weak mixing angle	0.22305(23)[g] 0.23121(4)[h] 0.23153(4)[i]

Symbol	**Quantity**	**Value**[a][b]
$V_\mathrm{m}(\mathrm{Si})$	molar volume of silicon	$1.205883199(60)\times10^{-5}\ \mathrm{m^3\cdot\ mol^{-1}}$
$Z_0 = 4\pi\alpha\hbar/e^2$	characteristic impedance of vacuum	$376.730313412(59)\ \Omega$
α^{-1}	inverse fine-structure constant	137.035999177(21)
$\alpha = e^2/4\pi\varepsilon_0\hbar c$	fine-structure constant	0.0072973525643(11)
$\Delta\nu_\mathrm{Cs}$	hyperfine transition frequency of ^{133}Cs	9192631770 Hz
$\varepsilon_0 = e^2/4\pi\alpha\hbar c$	vacuum electric permittivity	$8.8541878188(14)\times10^{-12}\ \mathrm{F\cdot\ m^{-1}}$
Λ	cosmological constant	$1.089(29)\times10^{-52}\ \mathrm{m^{-2}}$[c] $1.088(30)\times10^{-52}\ \mathrm{m^{-2}}$[d]
$\mu_0 = 4\pi\alpha\hbar/e^2c$	vacuum magnetic permeability	$1.25663706127(20)\times10^{-6}\ \mathrm{N\cdot\ A^{-2}}$
$\mu_\mathrm{B} = e\hbar/2m_\mathrm{e}$	Bohr magneton	$9.2740100657(29)\times10^{-24}\ \mathrm{J\cdot\ T^{-1}}$
$\mu_\mathrm{N} = e\hbar/2m_\mathrm{p}$	nuclear magneton	$5.0507837393(16)\times10^{-27}\ \mathrm{J\cdot\ T^{-1}}$
$\sigma_\mathrm{e} = (8\pi/3)r_\mathrm{e}^2$	Thompson cross section	$6.6524587051(62)\times10^{-29}\ \mathrm{m^2}$
$\sigma = \pi^2k_\mathrm{B}^4/60\hbar^3c^2$	Stefan–Boltzmann constant	$5.670374419...\times10^{-8}\ \mathrm{W\cdot\ m^{-2}\cdot\ K^{-4}}$
$\Phi_0 = h/2e$	magnetic flux quantum	$2.067833848...\times10^{-15}$ Wb